5-2008

Processing, Structure, and Properties of Amorphous Aluminum Alloys

Timothy Wayne Wilson
University of Tennessee - Knoxville

To the Graduate Council:

I am submitting herewith a dissertation written by Timothy Wayne Wilson entitled "Processing, Structure, and Properties of Amorphous Aluminum Alloys." I have examined the final electronic copy of this dissertation for form and content and recommend that it be accepted in partial fulfillment of the requirements for the degree of Doctor of Philosophy, with a major in Materials Science and Engineering.

Hahn Choo, Major Professor

We have read this dissertation and recommend its acceptance:

Peter Liaw, Takeshi Egami, David Joy

Accepted for the Council:
Dixie L. Thompson

Vice Provost and Dean of the Graduate School

(Original signatures are on file with official student records.)

To the Graduate Council:

I am submitting herewith a dissertation written by Timothy Wayne Wilson Jr. entitled *"Processing, Structure, and Properties of Amorphous Aluminum Alloys."* I have examined the final electronic copy of this dissertation for form and content and recommend that it be accepted in partial fulfillment of the requirements for the degree of Doctor of Philosophy, with a major in Materials Science and Engineering.

_____
Hahn Choo, Major Professor

We have read this thesis
and recommend its acceptance:

Peter Liaw
_____

Takeshi Egami
_____

David Joy
_____

Accepted for the Council:

Carolyn R. Hodges
_____
Vice Provost and Dean of the
Graduate School

(Original signatures are on file with official student records)

PROCESSING, STRUCTURE, AND PROPERTIES OF AMORPHOUS ALUMINUM ALLOYS

A Dissertation
Presented for the
Doctor of Philosophy
Degree
The University of Tennessee, Knoxville

Timothy Wayne Wilson Jr.
May 2008

Dedication

To my wife, Ashley Wilson, and all of my family, thank you for providing me inspiration and support.

Acknowledgements

I appreciate the help that many people have given me during the course of my Ph.D. study. My advisor, Dr. Hahn Choo has given me scientific guidance, inspiration, and motivation, and he has provided me the opportunity to further develop my academic and professional capability. I would like to thank my co-advisor Dr. Peter Liaw for his kind encouragement and advice. I would also like to thank my other committee members, Dr. Takeshi Egami and Dr. David Joy for their helpful advice and suggestions.

During this process many people have offered their kind advice, time, and knowledge. I am thankful to all of our team members: Mrs. Elena Garlea, Dr. Wanchuck Woo, Mr. Jinwoo Jeon, Dr. Kaixiang Tao, Dr. James Wall, Mr. Michael Benson, Mr. E-Wen Huang, Dr. Gongyao Wang, Mr. Robert McDaniel, Ms. Zhenzhen Yu, Mr. Andrew Chaung, and Mr. Soo-yeol Lee for all of their help. In addition, I am thankful to Dr. Cang Fan, Dr. Wenhui Jiang, Dr. Wojtek Dmowski, and Dr. Honqi Li. Mrs. Carol Winn, Mr. Douglas Fielden, and Mr. Frank Holiway have also made contributions for which I am grateful.

My special thanks go to those at Los Alamos National Laboratory for giving me the opportunity to work and learn from them. I am thankful to Dr. Donald Brown, Dr. Bjorn Clausen, and Mr. Thomas Sisneros for all of their help and guidance.

This work is supported by the NSF International Materials Institutes (IMI) Program under Contract DMR-0231320. This work benefited from use of the MUCAT beamline a APS and beamline X14A of NSLS at BNL. The use of the APS was supported by the U.S. DOE, Basic Energy Sciences, Office of Science, under Contract

No.W-31-109-Eng-38 and MUCAT by Contract No.W-7405-Eng-82 through the Ames Laboratory. Beamline X14A is sponsored by the Assistant Secretary for Energy Efficiency and Renewable Energy, Office of Transportation Technologies, as part of the High Temperature Materials Laboratory User Program, ORNL, managed by UT-Battelle, LLC, for the U.S. Dept. of Energy under contract DE-AC05-00OR22725. This work also benefited from the use of the Los Alamos Neutron Science Center at the Los Alamos National Laboratory. This facility is funded by the US Department of Energy under Contract W-7405-ENG-36.

Abstract

Although research has been conducted on amorphous aluminum-based alloys, most of the research has focused on melt-spun ribbons. There has been significantly less research on mechanically alloyed amorphous powder even though mechanically alloyed powder seems to have more potential for the production of bulk amorphous aluminum-based alloys. In addition, there has not been adequate research conducted on the local atomic structure of amorphous aluminum alloys, and a greater understanding of the relationship between processing, structure, and properties is necessary.

In the following thesis, multiple investigations have been performed to understand the structure, processing, and properties of aluminum-based amorphous alloys. These studies sought to develop a methodology for the production of amorphous aluminum alloys by mechanical alloying, understand how composition affects the glass-forming ability, understand the crystallization and its effects on structure and properties, and consolidate the mechanically alloyed powder and examine the resultant structure and properties.

High-energy ball milling was used to synthesize aluminum-based alloys containing amorphous and nanocrystalline phases to investigate the compositional effects of transition metals (TM) on the amorphization and crystallization processes of the ball-milled $Al_{85}Y_7Fe_5TM_3$ alloys (TM = Ni, Co, Cu, and Fe) were investigated.

The local atomic structure of mechanically alloyed $Al_{85}Y_7Fe_8$ and $Al_{83}Y_7Fe_8Ti_2$ were examined by high-energy synchrotron x-ray diffraction. Diffraction results showed that $Al_{85}Y_7Fe_8$structure to be nanocrystalline, while $Al_{83}Y_7Fe_8Ti_2$is amorphous. The pair

distribution function analyses revealed that local structure of $Al_{85}Y_7Fe_8$was dominated by Al, Fe, and Al_3Y short range ordered regions. On the other hand, the local structure of $Al_{83}Y_7Fe_8Ti_2$was comprised of Al, Al_6Fe, and Al_3Y short-range order regions, in which the order extended for about 8 angstroms.

Efforts to consolidate the mechanically alloyed amorphous powder were made by quasi-isostatic forging at different temperatures. Samples were also processed containing different levels of coarse grain crystalline aluminum to evaluate the production of bi-modal composites.

In addition to the research performed on amorphous aluminum alloys, research on the mechanical behavior of the local atomic structure of a bulk metallic glass was performed. The internal strain was measured for a $Zr_{57}Nb_5Cu_{15.4}Ni_{12.6}Al_{10}$ BMG *in-situ* by neutron diffraction.

Table of Contents

List of Tables

List of Figures

Chapter I: Introduction

1.1 Amorphous Aluminum-based Alloys

Amorphous aluminum alloys are of great interest due to their unique combination of high strengths (about 1,000 MPa [1] which can be up to 2-3 times greater than their conventional crystalline counterparts [2]) and low densities (about 3.5-3.7 g/cm^3 [3]). The strengths of these aluminum alloys can be further increased, to over 1,400 MPa, by partial crystallization [4, 5], as illustrated in Figure 1-1. Amorphous aluminum alloys are often produced in ternary compositions containing Al-RE-TM (RE = Rare Earth, TM = Transition Metal) due to their good glass formability and have been found to have good bending ductility of about 180º in wire samples [6-8]. For example, Al-Y-Fe systems have good glass-formability, due to the negative heats of mixing and the large (> 12%) atomic size differences [9-13] of the constituent elements. The addition of a second transition metal to these alloys to form quaternary systems, Al-RE-TM1-TM2, can further enhance the glass formability [14]. Aluminum alloys form marginal or weak metallic glasses. Because of this, aluminum based metallic glasses have only been produced in very small sizes. Ongoing research on aluminum-based amorphous alloys may eventually lead to the formation of bulk (diameter > 1mm) amorphous alloys.

Although aluminum-based bulk-metallic glasses have not been produced, aluminum-based amorphous alloys have been fabricated, by rapid solidification in ribbon form, by mechanical alloying in the powder form, gas atomization, and repeated cold rolling and folding. For the formation of Al-based glassy alloys the same empirical rules for glass formation in bulk glass-forming alloys tend to apply. Glass formation is favored

for multi-component systems. A large negative heat of mixing for the different elements and an atomic size mismatch of greater than 12% are necessary for glass formation. One difference between aluminum based glasses and bulk glass formers is that aluminum based glasses often form in systems that do not have a deep eutectic, which is common for other bulk glass forming alloys. In fact, aluminum-rare earth binary systems have the best glass formers at compositions of hypereutectic compositions [5]. Aluminum alloy's low glass-forming ability may be attributed to a low liquid fragility [15]. Low glass-forming ability is due to the molten liquid having a low viscosity that rapidly increases as it is cooled toward the liquidus temperature [16]. This corresponds to rapid structural rearrangements during freezing as opposed to the sluggish atomic redistribution that occurs in materials with high glass-forming ability.

There are several methods of producing amorphous aluminum alloys, almost as many techniques as for producing bulk amorphous alloys [1, 17-19]. The most promising techniques for producing amorphous samples for engineering applications appear to be by either rapid solidification or by deformation. Currently, the rapid solidification method has only been successful at producing ribbon samples with a thickness of less than a millimeter. Deformation-induced amorphization has been successful at producing amorphous powders, but there has been no successful attempt to fully consolidate these powders and still maintain the amorphous structure.

In order for these amorphous powders to be made into bulk samples, it is necessary to develop new compositions that will require a much lower critical cooling rate and high thermal stability; and/or it will be necessary to develop new processing methods capable of scaling up the size of marginal glass formers. In order to achieve this

it will be necessary to better understand the amorphization and crystallization mechanisms. Additionally, understanding the local atomic structure could lead to a way to understand and manipulate the atomic structure that would make the aluminum alloys stronger glass formers.

1.2 Synthesis and Characterization

Research has also been conducted on the formation of amorphous materials through solid-state reactions, such as mechanical alloying of powders. This technique can be coupled with powder consolidation to form amorphous alloys with larger dimensions than are capable of being produced through rapid solidification. Mechanical alloying is a solid-state reaction in which a great amount of energy being applied to the elemental powders to introduce defects and cause the steady refinement of the grains within the alloys until an amorphous structure is produced [20]. The glassy structure forms through an interdiffusion process, which occurs at low temperatures in the layered composite structure of the powder, which forms in the early stages of milling [21, 22]. An example of this layered composite structure is shown for a Ag-Cu system in Figure 1-2. Extended milling reduces the thickness of the layers until the layers have completely interdiffused.

Once amorphous powders have been produced, they can be consolidated into scaled-up samples with properties similar to those of the amorphous powder [4]. The properties of the bulk sample that is produced by consolidation of the mechanically alloyed powder will then be dependant on the consolidation parameters, such as time, temperature, and pressure. For example, consolidation at high temperatures can cause

partial or complete crystallization. Because the consolidation requires exposing the amorphous powder to elevated temperatures, increasing the crystallization temperature is of great engineering importance.

In addition to the technical benefits of increasing T_x, the investigation of crystallization behavior of amorphous alloys is important for the fundamental understanding of the glass-forming ability of these alloys. It has been observed that aluminum alloys often devitrify through a nanocrystallization process [23]. During this crystallization process, a high density ($> 10^{22}$ m^{-3}) of face-centered cubic (fcc) Al nanocrystals may form [11]. The formation of such nanocrystals may be linked to "quenched-in" nuclei, which have a short-range fcc-like structure consisting of Al atoms. Therefore, during the crystallization process, only short-range rearrangement of the elements is sufficient to form the nuclei into nanocrystals [24]. However, by forcing the crystallization to proceed through long-range diffusion rather than short-range rearrangements, the thermal stability can be improved along with the glass forming ability.

The glass-forming ability of metallic glasses was increased with the addition of certain elements in small amounts, or microalloying [25-28]. It has also been suggested that microalloying can increase the thermal stability of metallic glasses by suppressing the precipitation of crystalline phases during heating of the amorphous phase [26, 27, 29]. In particular, microalloying with Ti has been shown to effectively improve both the glass-forming ability and the thermal stability of these alloys presumably by changing the local order to hinder the precipitation of the fcc-Al phase [30], but the mechanism for this change is not fully understood. It is commonly found that Al-Fe-Y glasses often appear

amorphous when characterized by laboratory x-ray, more specifically, lacking the typical diffraction peaks observed in crystalline materials. However, further examination by isothermal differential scanning calorimetry (DSC) reveals that some aluminum-based glasses are comprised of a very fine nanocrystalline structure, and the crystallization event corresponds to a grain coarsening reaction, as opposed to a nucleation and growth reaction, which would occur in amorphous materials [31]. The addition of 2% Ti to Al-Y-Fe alloys dramatically improves the glass forming ability and changes the nature of the local structure of the alloy into an amorphous one [30]. The isothermal DSC curve for this alloy shows a peak that is characteristic of a nucleation and growth reaction occurring during crystallization.

Recent studies on the crystallization behavior using DSC and XRD revealed that the addition of 2% Ti to amorphous Al-Y-Fe systems also changed the crystallization from a primary crystallization of fcc-Al crystals to tetragonal Al_7Fe_5Y crystals presumably by forcing long-range diffusion of atoms to drive the crystallization process [32] The local order plays an important role in the mechanical and thermal properties of these alloys and structural studies are necessary to better understand this behavior. Short and medium-range order in amorphous materials is much less understood than long-range order in crystalline materials.

1.3 Powder Consolidation

In order for mechanically-alloyed powders to be used in engineering applications, it is necessary to consolidate the powder into bulk form. There have been many efforts to consolidate amorphous aluminum powder using various techniques, but there has been

little success in retaining the amorphous phase in a sample with full theoretical density. For example, efforts made in 1994 to consolidate MA $Al_{80}Ni_8Fe_4Gd_8$ by cold-pressing and subsequent hot-isostatic pressing produced only 93% dense samples, but these samples did have Vickers hardness values in the range of 625 – 650 [17]. This is much higher than those measured for conventional structural aluminum alloys which typically range from 100-190 HV. It has been found that by controlling the crystallization during powder consolidation, it is possible to produce very strong aluminum alloys. In 2001 $Al_{85}Ni_5Y_8Co_2$ was consolidated to 99% density, and the resulting compression tests showed high strengths of 1420 MPa [4], Figure 1-3. These high strength alloys (except for the powder consolidated at a relatively low temperature of 483°C) had a fully crystalline microstructure consisting of fcc-Al, Al_3Y, and $Al_{70}Ni_{11}Y_{15}Co_4$, Figure 1-4. Others have also successfully produced high strength aluminum alloys through consolidating MA amorphous powder, but to date, there have been no successful reports of fully dense, fully amorphous aluminum alloys.

1.4 Total Scattering

The determination of crystal structures is very important in the fields of chemistry, physics, and material science, because the structure of materials determine their properties. Traditionally this has been done by measuring and analyzing the locations and intensities of peaks resulting from Bragg diffraction. This method gives information regarding only the long range average atomic structure. If the material has deviations from the long range average structure, they will result in diffuse scattering which contains information regarding the local atomic structure. By combining diffuse scattering with

Bragg scattering, one can obtain information regarding the local structural ordering of materials. This is especially useful when studying liquids, glasses, disordered structures, and materials with defects.

The pair distribution function (PDF) is an analysis method that utilizes total scattering (i.e., Bragg scattering plus diffuse scattering) to accurately determine the local atomic structure [33]. The PDF can be used for materials that lack long-range order, or where the short-range structure is not reflected in the long-range order of the crystal. The PDF is a one-dimensional function showing the atom-atom distances of all of the atoms throughout the material. The PDF is represented in real space, rather than the reciprocal-space powder diffraction data [33]. This approach has been widely used for studying the structures of glasses and liquids since the 1930s [34]. This real-space method is one of the small number of experimental techniques that can be used to probe structure on the nanometer length scale, when the local structure is not consistent with the long-range globally-averaged structure [35]. PDF studies have provided details about the local ordering [36], free volume [37, 38], and mechanical behavior [37, 39, 40] of BMGs.

1.5. Motivation of the Research

Amorphous aluminum alloys are of technical interest due to their high specific strengths, however; they have not found engineering applications due to their low glass-forming ability. Recent efforts have shown that glass-forming ability can be increased by adding small additions of specific elements. These elements improve the thermal stability of the amorphous phase, but the mechanism of this improvement still remains unknown. While microalloying may not be able to decrease the critical cooling rate of

aluminum alloys enough to form bulk amorphous alloys through rapid solidification, it appears a promising approach to improve the amorphization through powder processing. By increasing the crystallization temperature of the amorphous alloy, the temperature range, or thermal window, for consolidation of these materials can be increased along as well. This dissertation research seeks to build a greater understanding of the solid state amorphization of aluminum alloys, gain insight regarding the nature of the local atomic structure in the amorphous phase, understand the crystallization process, and use this information towards developing new high-strength aluminum alloys. Figure 1-5 shows the objectives, tasks, and anticipated results of the present dissertation, see Appendix for Tables and Figures. In this research, a correlation between the synthesis, local atomic structure, and physical and mechanical properties will be established. A greater understanding of the chemical short-range ordering in the local atomic structure of amorphous aluminum alloys will be achieved. This research also provides an analysis of a novel processing methodology for the production of amorphous aluminum alloys.

Chapter II: Literature Review

Part I. Bulk Metallic Glasses

Metallic glasses are a new class of materials that have very different properties when compared to conventional metals. They have an amorphous microstructure, which causes them to have some exceptional properties. Metallic glasses have been produced in many different compositions and in compositions with many different base elements. They are of interest for both scientific and fundamental reasons, as well as having great engineering potential. Some metallic glasses are already being used in specific applications, and other applications appear to be coming in the future.

2.1 History

Amorphous metallic materials, or metallic glasses, are a relatively new class of materials that first emerged in 1959 when Duwez showed that $Au_{75}Si_{25}$ could be rapidly solidified from the liquid form without crystallization [41]. His experiments illustrated that by spreading thin films on a conductive substrate; cooling rates of 10^5 to 10^6 K/s could be achieved, thus circumventing the crystallization process. Since then a great number of amorphous materials have been synthesized, and the topic of bulk amorphous alloys has been of great scientific interest. During the 1970s and 1980s their primary interest was due to their soft magnetic properties, which could be used in applications such as transformer cores and other magnetic devices [42]. Further interest came in the 1980s after it was found that ingots could be cast with diameters up to 1 cm, cooling at

rates below 100 K/s [43]. All this interest stems from their unique mechanical, physical, and chemical properties, which distinguish them from their crystalline counterparts.

2.2 Properties

Metallic glasses contain atoms that are randomly arranged throughout the solid. This random nature makes them free from the typical defects that are seen in crystalline alloys such as, dislocations and grain boundaries. This increases the amount of energy required to cause the metallic glasses to fail to values much closer to their theoretical strength. This absence of crystal slip systems causes the metallic glasses to have many desirable mechanical properties, including high strength and hardness and good wear properties. Table 2-1 shows a comparison of the properties of conventional (crystalline) metals to bulk structural amorphous alloys. Properties such as tensile fracture strength, hardness, and Young's modulus have been shown to further increase following a heat treatment that caused the precipitation of nanocrystalline particles from the amorphous matrix. This increase in mechanical properties was found to continue as an increasing volume fraction of nanocrystals was precipitated from the amorphous matrix, up to about 25% nanoparticles [44]. Another important mechanical property of bulk metallic glasses is a very high elastic limit. The elastic strain that a metallic glass can support in tension or bending is almost double that of its crystalline counterpart [45]. Additionally, the lack of defects and the chemical homogeneneity cause bulk metallic glasses to have a high corrosion resistance [45].

2.3 Applications

Due to their unique properties, bulk amorphous alloys have become of great interest in a number of engineering applications. Their high strengths and good toughness have made bulk amorphous alloys a promising candidate for structural applications. These applications could include the areas of aircraft frames, automobiles, and medical implants. Metallic glasses have been shown to have good corrosion resistance. The added corrosion resistance of metallic glasses for structural applications makes these alloys even more desirable. With their elastic energy storage density almost double that of crystalline alloys, bulk metallic glasses are ideal material for springs [46]. This property has also been exploited in the sporting good industry, as golf clubs are also being produced with metallic glass heads [3]. The combination of high wear resistance and corrosion resistance has lead to the application of amorphous alloys in spray coatings [47]. One of the most significant applications of metallic glasses has been in applications requiring soft magnetic properties. The chemical homogeneity of these alloys leads to the absence of magneto-crystalline anisotropy, which gives rise to low coercivity and low hysteretic loss. For these reasons metallic glasses, typically with compositions containing a ferromagnetic base element, have seen applications in the cores of distribution transformers, tape recorder heads, and other small magnetic devices [3, 42].

2.4 Glass Formation

2.4.1 Glass-Forming Ability (GFA)

The ease at which an alloy can be processed into a glassy state is known as its glass-forming ability (GFA). Understanding what determines the GFA of different alloys

is critical in the development of new metallic glasses as well as understanding why existing metallic glasses are possible. Common methods of quantifying an alloy's GFA involve measuring its characteristic temperatures by means of differential scanning calorimetry and/or differential thermal analysis. The most widely used parameters are the reduced glass transition T_{rg} temperature, which is the glass-transition temperature divided by the liquidous temperature, $T_{rg} = T_g/T_l$, [48] which is determined by the stability of the liquid phase, and the supercooled liquid region ΔT_x which is related to the resistance to crystallization for the glassy phase and is the difference between the onset of crystallization temperature and the glass-transition temperature, $\Delta T_x = T_g - T_x$ [49]. These glass-forming criterions are shown in Figure 2-1. Another, more recent, approach to examining the GFA of metallic glasses has been formulated which takes into account that the two key components to GFA are liquid phase stability and resistance to crystallization [50, 51]. This measure, γ, is determined by dividing the onset of crystallization temperature, T_x, by the sum of the glass transition temperature and the liquidous temperature, T_g+T_l. γ relates GFA by relating both the kinetic and thermodynamic effects of the glass transition. From a kinetic point of view, the higher the T_g, the slower the atomic mobility and resulting in a high GFA. From a thermodynamic point of view, the lower the T_g, the higher the liquid phase stability and resulting in a higher GFA. Figure 2-2 shows the linear relationship between and γ the critical cooling rate [52]. Because γ takes into account both the effects of liquid phase stability and the resistance to crystallization, where T_{rg} and ΔT_x do not, it appears that γ is the best measure of GFA.

2.4.2 Metallic Glass Forming Criteria

Producing a model for GFA has been challenging for the scientific community. Earliest rules for glass formation were strictly empirical. Inoue developed three empirical rules for glass formation. These rules say that for metallic glasses to be formed the system should be comprised of multiple components, they should have atomic sizes that are at least 12% different, and that the heat of mixing between the components should be negative and relatively large. The reasons for these rules appear relatively simple. The system should have multiple components because adding elements adds strain at the local atomic level. It is necessary for the difference in atomic sizes because different size elements create strain within the lattice, and when the strain reaches a critical value the structure breaks down and becomes amorphous. The reason for the need for negative heat of mixing is that when the heat of mixing is negative between atoms of different elements, the atoms want to be surrounded by the unlike atoms. This causes increase in random packing density, which leads to difficulty in atomic rearrangements. This also decreases atomic diffusivity and viscosity. These rules have been shown to be accurate for a wide range alloys systems, particularly in the La-, Zr-, Mg-, Pd-, and Fe-systems [53-57]. The most recent modeling attempts will be discussed later.

2.5 Compositions

For multi-component bulk metallic glass systems, the role of atomic size and chemical interactions appear to be the most important for glass-formation. While there are many different compositions of metallic glasses, there exist some similarities in the known glass formers. Poon suggests that these known glass-forming alloys can be

grouped into two broad classes based on the atomic sizes of the constituent elements [8]. The first class of bulk metallic glasses contains alloys with the mid-sized element as the majority element often containing 60-70 atomic percent. The smaller elements and the larger elements are the minority components, with the small element comprising 20 to 30 atomic percent and the large element accounting for 10 atomic percent. This class of bulk metallic glasses is termed 'majority atom-small atom-large atom' or MSL class. The other class is labeled the 'large atom-small atom' or the 'small atom-large atom' class (LS/SL class). It includes alloys with primarily large sized atoms comprising about 40 to 75 percent and small atoms making up 25 to 60 percent of the alloy.

Due to the large negative heats of mixing between the large and small atoms in the MSL category, these atoms tend to be strongly attracted towards each other. This attraction is often greater than the medium-sized atom pairs with either the large or small atom. Because of this attraction, there will be pairs of large and small atoms distributed throughout the amorphous matrix. This has been referred to as a reinforced "backbone" [8]. This backbone has been attributed to stabilizing the undercooled melt, which would in turn inhibit crystallization. Figure 2-3 shows a schematic drawing of this networked or backbone structure. A similar situation is occurring in LS/SL systems with the large and small atoms being attracted towards each other creating difficulties in crystallization.

2.6 Processing

Several processes can be used to form amorphous metals. These can be generalized into two categories, rapid solidification from a liquid phase and deformation of an existing crystalline microstructure. Each processing method has its own distinctive

advantages and disadvantages. The properties of the metallic glasses produced by different processing methods are often slightly different as well. The sizes of the final product available are also different depending on which processing method is chosen. Most importantly, different processing methods can be tailored to a given application. Some of the different processing methods are shown in Table 2-2, and these include rapid cooling of the liquid, under-cooling of clean liquids, physical vapor deposition, chemical methods, irradiation, mechanical methods, and reactions [44]. This review will focus on the most common methods as seen in literature.

2.6.1 Rapid Solidification

Rapidly solidified metallic glasses are formed when the liquid is cooled at a rate sufficiently high to prevent crystallization. In order to solidify an amorphous phase from the liquid phase it is critical to suppress the nucleation and growth process of a crystalline phase in the super-cooled liquid region. This is the region between the melting temperature (T_m) and the glass transition temperature (T_g) [58]. Alloys with high glass-forming ability typically have narrower regions between T_m and T_g, or small reduced glass-transition temperatures, T_{rg} ($T_{rg} = T_g/T_m$) [48]. Additionally, there exists a critical cooling rate (R_c) at which these alloys must be cooled or else they will solidify into crystalline phases rather than a completely amorphous one. The critical cooling rate is crucial in determining the size of the bulk metallic glass that can be made upon rapid solidification. The relationship between R_c and t_g ($t_g = T_g/T_m$), seen in Figure 2-1, along with how sample thickness, is directly proportional to the critical cooling rate. R_c has also been related to the GFA parameter γ [52] by the equation:

$$R_c = 2x10^{21}\exp(-114.8\,\gamma) \quad (1)$$

There are many ways of producing cooling rates high enough to solidify a glassy alloy, and depending on the magnitude of the cooling rate necessary, several different techniques are available to produce different sizes of glassy products. With lower critical cooling rates, larger samples can be fabricated. Figure 2-1 also shows many of the bulk metallic glass-forming compositions that have been discovered to date and their critical cooling rate. While this figure illustrates many glass forming compositions, it is not a complete list of glass forming compositions. The advantage of this technique is that large (several millimeter diameter) samples can easily be produced with good reproducibility. A disadvantage of this technique is that the compositions are limited to those near eutectics.

2.6.2 Melt-Spinning

One common method of producing glassy alloys that require a very high critical cooling rate is melt-spinning of thin ribbons. In this method, a master alloy sample is created by melting the elemental components together and solidified to give a homogeneous mixture. The thin ribbons are produced by ejecting the molten master alloy liquid onto a spinning wheel, usually copper, because of its high thermal conductivity, which cools the sample at rates of about 10^5 to 10^6 K/s. This produces samples that are less than a millimeter thick (typically < 50 μm) and a few millimeters wide, as presented in Figure 2-4. Melt-spinning produces alloys that were cooled at very

high cooling rates, and the ribbons were cooled under very clean conditions. Because of this nucleation is suppressed and crystallization can be avoided [44]. The cooling rate that can be achieved during melt-spinning is directly related to the speed at which the wheel rotates. This in turn can be very important in the resulting microstructure and properties of the material [59]. For a material whose critical cooling rate is in the range of about 10^5 to 10^6 K/s, the wheel speed will determine whether that material is crystalline, crystalline plus amorphous, or purely amorphous. This can be seen for the $Y_{60}Fe_{30}Al_{10}$, as shown in Figure 2-5. Melt-spinning is a valuable technique for producing marginal glass forming alloys because of its high cooling rates.

2.6.3 Metallic Mold Casting

Metallic glasses were first made into bulk metallic glasses by Chen in 1974 when he used suction casting to fabricate millimeter diameter rods [60]. Suction casting systems, as shown in Figure 2-6, typically have two chambers, upper and lower. The upper chamber is at a higher pressure and is where the ingot is remelted, and the lower chamber is at a lower pressure and is where the ingot is cast. When the ingot is melted, a valve opens and the molten liquid is sucked into the water-cooled copper mold due to the large difference in pressure between the two chambers. Bulk metallic glasses can also be made by drop casting, injection casting, and several other casting methods, which utilize the same idea of melting the master alloy ingot in an upper chamber, dropping, injecting, or sucking it into the water-cooled copper mold, and then rapidly cooling the sample before it can crystallize. Casting is now the most common method of producing bulk metallic glasses. Casting methods have been used to produce BMG's with diameters of

several centimeters in La-, Mg-, and Zr-alloy systems with low critical cooling rates [61-63].

2.6.4 Deformation

Deformation techniques generally start from crystalline materials and deform them to a point in which no crystalline structure remains. Mechanical alloying is a powder metallurgy technique capable of producing solid-state amorphization reaction. According to Suryanarayana, this involves sufficient energy being applied to the material to introduce defects and cause the steady refinement of the grains within the alloys. In these processes, deformation causes an accumulation of strain energy within the lattice. Upon further deformation, the local atomic strain levels increase, due to the high dislocation density, and eventually the crystal changes into subgrains with low angle grain boundaries in order to decrease lattice strain. More deformation causes new shear bands to form in the unstrained region, and the grain size steadily decreases, as small angle grain boundaries become large angle grain boundaries through grain boundary rotation. Eventually nanometer sized grains are formed, and these nanograins and their increased grain boundary area can drive the crystalline to amorphous transformation [20]. Some of the factors that control the amorphization reaction include the milling intensity, the milling atmosphere, and the ball-to-powder ratio [64]. Advantages of this technique are that the process can be scaled up from powder samples to large consolidated samples and compositions are not limited to compositions near the eutectic [64].

2.7 Structure

2.7.1 General Structure

Conventional alloys have a crystalline structure, with their atoms arranged in an orderly, repeated manner. These crystalline areas are grouped together in identically aligned regions, called grains, and between the grains are thin regions, which do not contain this crystalline structure, called grain boundaries. These grain boundaries often serve as a point of weakness in the material. The feature of metallic glasses that makes them so fascinating is their amorphous nature. This means that metallic glasses are free from the long-range order that crystalline materials possess.

Amorphous structures are characterized by a broad halo present in an x-ray diffraction (XRD) pattern. This means that there is an absence of long-range order in their structure. Even though the glasses contain no long-range order, it is possible that their arrangement is not completely random. For example, silica glasses have a well-defined short-range order in which every silicon atom is bonded to four oxygen atoms, but this ordering does not extend in a periodic array throughout the crystal. This lack of long-range order means that these glasses are amorphous. Metallic glasses can have similar short range ordering, but are typically less stable. This order comes from the strong chemical interactions between the individual atoms, and is responsible for some alloys being bulk glass forming alloys and some (that do not have a well defined short range order) to be only marginal glass formers. Understanding the amorphous structure is important to scaling up bulk glasses and making marginal glass formers into bulk glass formers, as well as understanding their unique properties.

The distinctive mechanical properties of bulk metallic glasses are due to their amorphous structure. Some metallic glasses' properties can be further improved by annealing to a temperature in which partial crystallization will occur. This will produce a composite of nanocrystalline, defect-free particles reinforcing an amorphous matrix [5]. Figure 2-7 shows a schematic of how nanocrystalline particles serve to reinforce the amorphous matrix against shear deformation. The crystallization process is heavily dependant on composition, annealing procedure, and oxygen content. The understanding of the local atomic structure is vital in the understanding of both the mechanical properties and thermal stability as well as gaining a predictive way of discovering new alloys with high glass-forming ability. The local atomic structure of these alloys can be analyzed by techniques such as anomalous x-ray diffraction (AXS) and neutron scattering [65]. From the information that is available from these techniques, it is possible to gain insight on the reasons for high glass-formability in some compositions.

The most common ways of determining the crystal structure of a material are X-ray diffraction and transmission electron microscopy. Crystalline materials will diffract beams of x-rays or electrons (or neutrons) according to Bragg's Law, but since amorphous materials do not have periodic structures they only reveal broad background in diffraction. This is seen in XRD as a broad hump and in TEM diffraction as a broad diffraction ring or halo. Figure 2-8 shows an example of the diffraction patterns a Zr-based BMG in the as-cast, amorphous state, and in various stages of the crystallization process due to isothermal annealing. Figure 2-9 shows the TEM micrographs of an Al-based glassy powder in the amorphous state and in various stages of the crystallization process as it is consolidated at various temperatures. The observance of these

amorphous-like features by diffraction does not guarantee that the structure is amorphous [31], but diffraction is still commonly reported in the literature. Common diffraction techniques can show that a material has no long-range order, but other techniques are necessary to reveal information about short or medium range ordering in these materials.

2.7.2 Local Atomic Structure

Anomalous x-ray scattering takes into account the fact that the scattering factor of an atom is only dependant on the energy of the x-ray near the absorption edge of that particular atom. The energy dependence, which is known as anomalous dispersion, is due to the resonance of the x-ray with the excitation of the electrons around the nucleus of the atom. By choosing the correct energy, one can resolve the scattering of one particular element from each additional element [65]. By doing this it is possible to obtain a radial distribution function (RDF) around a particular element. Figure 2-10 shows the scattering intensity profiles of $Mg_{50}Ni_{30}La_{20}$ [66]. The figure shows a typical profile of a completely random arraignment of atoms with the exception of the prepeak seen at Q = 14nm^{-1}. This prepeak is interpreted as presence of chemical short range ordering. This short range ordering is common in many metallic glasses, as well as oxide glasses. Figure 2-11 is the environmental RDF of Ni and the ordinary RDF of $Mg_{50}Ni_{30}La_{20}$ [55]. By comparing the peak positions of the environmental RDF of Ni to the ordinary RDF of $Mg_{50}Ni_{30}La_{20}$ and to the distances of crystalline pairs of Mg_2Ni, Mg_2La, and Ni_2La, it is found that the first peak region is due to Ni-Ni, Ni-Mg, and Ni-La pairs and not from Mg-Mg, La-La, and Mg-La pairs. The average coordination number and atomic separation distances from the first peak were reported to be 9.13 at 0.284nm,

which agrees with the coordination number of 9.12 calculated from crystalline pairs of Ni-Ni, Ni-Mg, and Mg_2Ni. These structural features, namely chemical short-range ordering, could be part of the reason why these alloys have a wide super-cooled liquid region, as well as their high glass-forming ability.

Another method for determining structural information on the local atomic level is by conducting a total scattering experiment. The increased availability of spallation neutron sources is particularly advantageous for performing pair-distribution function (PDF) analyses, due to their ability to provide high Q information. These sources are capable of producing high resolution, wide angle, and total scattering, which are necessary for PDF measurements. PDF measurements are real space description of atomic pair correlations, which provides information about the local structure of the atoms, without the requirement of long-range order. For this reason it is used to analyze amorphous systems. Figure 2-4 shows the structure function of $Fe_{68}Zr_4Nb_4B_{24}$ alloy along with $(Fe_{70}Mn_{30})_{68}Zr_4Nb_4B_{24}$ (in which Mn has been substituted for Fe). Noticeable in this figure, is a prepeak a 1.5 $Å^{-1}$, which indicates that the Mn substitution enhances the chemical short range ordering [67]. Chemical substitutions can also have noticeable affects on chemical interactions between the constituent elements. This is illustrated in Figure 2-5, which is the PDF for the Fe-Zr system with substitutions of Mn for Fe and Nb for Zr. This shows how substitution for one element can cause the interaction between two different elements to change. In this case, as Nb is substituted for Zr, the intensity of the Fe-B peak increases, while the intensity of the Fe-Fe peak decreases. From this it is clear that Nb does not just substitute for Zr, but chemically interacts in someway to

change the local structure [67]. This information could be then correlated to information on physical properties to find alloys with optimal characteristics.

From these measurements it is clear that these amorphous metals are not completely random in nature. Strong atomic interactions between the different elements in the alloy cause short and medium range ordering that allow the glasses to have a distinct local atomic structure without having long range order. A structural model has been proposed that can account for short range ordering that allows the alloys to maintain their amorphous (lacking long-range order) character. This structural model is based on the dense packing of atomic clusters [68]. In this model there exist local coordination clusters in which the cluster consists of a solute atom at the center surrounded by solvent atoms arranged in an array with no orientation between clusters, Figure 2-14. The solvent atoms will then occupy random positions throughout the material. The relative atomic sizes of the solute atoms compared to the solvent atoms, determines coordination number for these clusters. Neighboring clusters will share faces, edges, or vertices depending on the orientation of the cluster. These different orientations will create interstices between the clusters, which can be filled by smaller second (and third) solute atoms. Solute atoms that have radius ratios with the solvent atoms that allow the most efficient packing are preferred in metallic glasses with good glass forming abilities.

2.8 Thermal stability

2.8.1 Glass Transition

Due to the fact that bulk metallic glasses are formed through non-equilibrium processes, the final form of the alloy that can be obtained is a metastable one. When

these glasses are heated beyond a certain point they undergo a structural relaxation at the glass-transition temperature, T_g. This structural relaxation occurs through the rearrangement of the atoms to a structure closer to that of the liquid. For this reason, these alloys are called super-cooled liquids when they are at temperatures above T_g and below the onset of crystallization temperature, T_x. Further heating above T_x will cause the super-cooled liquid to crystallize. The structural relaxation of BMG's is quite similar to those observed in conventional glasses [69]. Figure 2-15a is shows a typical differential scanning calorimetry (DSC) curve for bulk metallic glasses. From this curve we can notice that the glass transition occurs with the release of endothermic energy corresponding to atomic relaxation [70]. Experiments performed using ultrasonic measurements on annealed $Zr_{41}Ti_{14}Cu_{12.5}Ni_{10}Be_{22.5}$ BMG samples have shown results consistent with a phase transition occurring at the glass-transition temperature. The results of these experiments are shown in Figure 2-15b. Also shown is that density and Vicker's hardness change suddenly at the glass-transition temperature, and because this is not just gradual change with temperature, the abrupt changes indicate a phase change [70]. The changes in density, measured by Archimedes principle, are reportedly due to annihilation of free volume during the structural relaxation of the glass. The occurrence of this free volume is due to various quenched-in defects. A similar decrease in free volume has been reported by positron annihilation spectroscopy [71]. The relative change in acoustic velocity, as measured by the pulsed-echo overlap method, was also seen to occur abruptly at the glass-transition temperature. These changes are due to the nature of the changes in the chemical bonds, which influence microstructure of the super-cooled liquid region. This microstructural change causes a variation in the acoustic

properties. For these reasons it is suggested that a phase transition is occurring at the glass-transition temperature [70].

A different group performing a different experiment seems to have verified the existence of a phase change at the glass transition temperature by studying specific heat at temperature. Figure 2-16 show the temperature dependence of the apparent specific heat for $Zr_{60}Al_{10}Co_3Ni_9Cu_{18}$. The samples were cast with diameters of 5mm and 7mm. Also included was a melt-spun ribbon with thickness of 20μm. The results show slight increases in C_p, up to about 500K. At this point the specific heat begins to decrease due to the structural relaxation before the glass transition. Then, at about 580K, there is a rapid increase in specific heat corresponding to the glass transition, at which point the alloy is at an equilibrium super-cooled state. There is a gradual decrease in Cp for the super-cooled liquid state followed by a rapid decrease due to crystallization [72]. These rapid changes in specific heat along with the ultrasonic measurements seem to show that bulk metallic glasses undergo a phase transition when heated to the glass transition temperature. From the specific heat data, it also appears that there is phase transition occurring upon crystallization as well.

High temperature synchrotron diffraction can also be used to see how the structure changes with temperature. If a phase change is going to happen when a bulk metallic glass is heated to the glass-transition temperature, and it becomes a super-cooled liquid it would be expected to see a structural change occurring with this process. This is seen in Figure 2-17, which shows the temperature dependence of the position q_1 and the height $S(q_1)$ of the maximum structure factor [73]. The sudden change in slope in this

figure is due to the alloy transforming from a glass to a super-cooled liquid at the glass transition temperature.

2.8.2 Structural Relaxation

As mentioned the high cooling rates prevent crystallization in metallic glasses, and the amorphous structure is not at its lowest free energy level. Upon heating of the glass to temperatures below the glass transition temperature, T_g, the atoms are able to rearrange themselves from a higher free energy state to a lower one. This phenomenon is known as structural relaxation. The existence of quenched-in defects during the solidification process has been identified as the primary cause of this higher energy metastable amorphous state. It is commonly described by the free volume model, in which, excess volume is trapped during the quenching process, as the viscosity of the melt is sufficiently high to prevent the atoms from migrating to their lowest free energy state. By relaxing these alloys, their properties can be altered. These properties include elasticity, magnetism, diffusivity, electrochemical properties and others [74]. In order to structurally relax a glass, the alloy must be held at a temperature below T_x but high enough to allow the atomic mobility to be great enough for the atoms to rearrange the amorphous structure.

2.8.3 Crystallization

Another critical feature of amorphous alloys is the crystallization process. Crystallization can be observed in the DSC curve, Figure 2-15(a) of metallic glasses as a sharp exothermic peak occurring after the glass-transition, corresponding to the formation

of a long-range ordered structure. This stage is caused by the precipitation of crystallites that are either one of the pure elements or a compound composed of some of the constituent elements. The exact order of crystallization is dependant on the composition. It occurs when a sufficient amount of energy has been received by the alloy for the atoms of the metastable amorphous phase to redistribute themselves from their random arraignment into a periodic crystalline arrangement. This takes place on a very small scale at first, and the result is the precipitation of crystalline particles, that can be in the size range of a few nanometers, to a few tens of nanometers. It has been found that this is due to one of two processes. One involves phase separation in the super-cooled liquid, and that such a fine-scale phase separation before crystallization causes the crystallites to have sizes on the nanometer scale. This effect has been studied by small angle neutron scattering (SANS), and is seen in the appearance of an interference peak. The other occurs through a primary crystallization, provided that there exists a high density of sites for heterogeneous nucleation, mainly "quenched-in" nuclei [75]. In this case the composition plays an important role in the growth of the nanocrystalline structure. As the growth process is limited by the slow diffusivity of the large elements in the primary crystalline phase, the crystallites formed remain on the nanometer scale.

2.8.4 Nanocrystallization

It has been frequently assumed that the devitrification of these amorphous alloys is undesirable, but recent studies have shown (as previously mentioned) that controlled crystallization can actually improve some of the properties. Because the crystallites that form in the amorphous matrix are often just a few tens of nanometers large and are defect

free, they can, in fact, improve strength, ductility, and toughness as the volume fraction of nanoparticles increases, up to an optimal value [44]. These nanoscale particles are smaller than the shear deformation band thickness and act as an effective barrier against deformation, as illustrated in Figure 2-7 [5]. A partially devitrified microstructure can also be useful in improving other properties, such as soft magnetic properties. As previously mentioned, it is possible to produce a microstructure with a nanoscale dispersion of defect free crystals. These crystals have been shown effective in pinning domain boundaries, and can limit hysteretic losses at high frequency [76].

Nanocrystallization via partial crystallization of the amorphous matrix has been shown possible in many classes of glassy alloys. These include Al, Fe, Ln, Mg, Ni, Pd, and Zr-based metallic glasses. [54, 77-84]. The nanocrystallization process results in elemental nanocrystals or solid solutions for Al, Mg, Ni, some Fe - based alloys, and intermetallic compounds for Ln, Pd, Zr, and some Fe-based alloys. Quenched-in nuclei have been identified as important factors in the nanocrystallization process [85]. Because atomic configurations of the glassy structure are quenched-in during the solidification process, the nature of the quenched-in nuclei is dependant on the atomic interactions in the liquid structure [86].

It has been identified that in order to form a nanostructured material from an amorphous matrix it is necessary for the following criterion to be met [87]: (1) a multi stage crystallization mode leading to a primary crystalline phase, (2) a homogeneous nucleation of the primary phase must be thermodynamically easy, (3) the subsequent growth reaction of the crystal should be slow, and (4) the remaining amorphous phase must be thermodynamically stable. This is well illustrated in the case of

$Zr_{60}Cu_{20}Al_{10}Pd_{10}$ and $Zr_{65}Cu_{27.5}Al_{7.5}$ [85, 88]. In this case, $Zr_{60}Cu_{20}Al_{10}Pd_{10}$ forms nanocrystals, while $Zr_{65}Cu_{27.5}Al_{7.5}$ does not. The Pd has a much larger negative heat of mixing with Zr than that of the other atomic pairs in the alloy. As a result short-ranged ordered (Zr, Pd) domains were formed. The Pd causes the crystallization mode to change from a single stage to two-stage crystallization, as shown in Figure 2-18, in addition to the generation of homogeneous Zr-Pd clusters. The growth of these clusters is difficult because of the enrichment of Al in the remaining amorphous phase. The difficult of growth results in a high activation energy for the precipitation of the Zr_2(Cu,Pd) phase. Also the Al-enriched amorphous phase has increased thermal stability, and this plays an important role in the maintenance of the nanoscale size of the crystallites.

2.9 Local Structure of Metallic Glasses

As total scattering measurements have become more accurate and accessible with creation of more pulsed neutron sources and synchrotron sources, high-speed computers have also benefited scientists and engineers wishing to perform structural measurements [65]. Today there exist many applications of structural measurements involving Bragg and diffuse scattering. These subjects include amorphous materials, disordered structure, and materials with defects.

Present work that is being conducted on Zr-based bulk metallic glasses has shown that neutron scattering can provide insight into the local atomic structure of these materials even though they do not have any long-range periodic structure that would be observed during typical Bragg diffraction. PDF analysis on as-cast, structurally relaxed,

and partially crystallized samples has provide insight into the crystallization process and may lead to better understanding of their mechanical properties [89].

Following heat treatments to produce structurally relaxed and partially crystallized metallic glass samples, neutron scattering experiments were carried out at the General Purpose Powder Diffractometer (GPPD) at the Intense Pulsed Neutron Source (IPNS) at the Argonne National Laboratory, USA to examine the local structure of these materials [90]. Atomic pair distribution functions (PDF) were obtained by a Fourier transformation of the normalized structure factors. The standard data reduction was performed to obtain the structure factors, however, several additional steps were undertaken to minimize systematic and statistical errors. Samples were mounted without a container, and long measurement times were carried out in groups of five detector banks. Before merging, detector banks scale was adjusted by minimizing root-mean squared, RMS, noise at low r in the PDF(r). Q_{max} was selected by a constraint that the difference in the first PDF peak corresponding to the first atomic shell was minimized.

Figure 2-19 and 2-20 present the experimentally obtained structure factor, $S(Q)$, and the total pair distribution function, for the as-cast, structurally relaxed, and partially crystallized $Zr_{55}Cu_{35}Al_{10}$ [90]. The experimental data shows that the as-cast and structurally relaxed samples studied are still amorphous materials. No diffraction peaks, characteristic of crystalline inclusions formed during the cooling or annealing process, are observed in the S(Q) – Q patterns for as-cast and structurally relaxed samples. The partially crystallized sample shows the only small crystalline peaks, which superimposed onto the amorphous peak at low Q, indicating partial crystallization.

The PDF of as-cast samples show only a single first shell peak, and there are three peaks at the second cell. These peaks indicate that there is not only short-range order, but also medium-range order existing in as-cast samples. As shown in Fig. 2-20(b), small but visible changes can be observed in the first atomic shell as a result of structural relaxation. It is seen that effect of the structural relaxation is to sharpen the fist pair of the PDF peaks without shifting them. Peaks increased in intensity for the first pairs, but lowered for the second pairs. This is essentially the same result that was observed in traditional metallic glasses [89, 91]. It can be interpreted in terms of local atomic stresses [92], in which the effect of low temperature structural relaxation is to eliminate short and long inter-atomic distances, which are under compression and tension forces. No meaningful changes were observed in the PDF beyond the first peak. Therefore, it was concluded that relaxation was mostly due to small changes in the first atomic shell resulting from the elimination of extreme inter-atomic distances.

After partially crystallized, peaks increased in intensity in first shell, at 3.10 angstroms and in the second shell at 4.85, 5.25 and 5.87 angstroms. Additionally, the peak at 4.85 angstroms increased in intensity more than the others. As shown in Fig. 2-19 this amorphous alloy crystallizes to quasicrystals. The changes in the peaks in the PDF after partial crystallization are from the nucleation and grain growth of quasicrystals. The similar peak shapes in the PDF of as-cast and partially crystallized samples imply that quenched-in nuclei in medium-range order, with quasicrystalline structure, exist in the as-cast samples of this alloy. Amorphous structures can be considered as frozen liquid structures. The quenched-in, quasicrystalline MRO, shows the link in the relationship between quasicrystal cluster packing and liquid structures.

2.10 Conclusions

Bulk metallic glasses have shown to have many unique mechanical and physical properties. At the heart of these distinctive properties is a microstructure that science is just beginning to understand and manipulate. As this understanding of metallic glasses continues to improve, so will bulk metallic glasses role in engineering applications. With all of the effort that has gone into studying bulk metallic glasses, a great improvement has come about in the general understanding of this unique class of materials. With further understanding of their atomic structure and how it behaves under different conditions, the bright future of bulk metallic glasses will move closer and closer to fruition. But in order to get to that future, there is still much to be learned about this interesting class of materials.

Part II. Amorphous Aluminum Alloys

Amorphous aluminum alloys are of great interest due to their unique combination of high strengths (about 1,000 MPa [1] which can be up to 4-5 times greater than their conventional crystalline counterparts [2]) and low densities (about 3.5-3.7 g/cm^3 [4]). The strengths of these aluminum alloys can be further increased, to over 1,400 MPa, by partial crystallization [3, 5]. Aluminum alloys form marginal or weak metallic glasses. Because of this, aluminum based metallic glasses have only been produced in very small sample. Ongoing research into aluminum based amorphous alloys may eventually lead to the formation of aluminum bulk amorphous alloys.

2.11 History

The development of bulk amorphous aluminum alloys has seen more difficulties than have been experienced in many other systems. Early attempts at producing amorphous Al-based systems were performed by rapidly quenching of binary systems of Al-metalloid and Al-transition metal systems. These attempts were successful at producing a structure consisting of concurrent amorphous and crystalline phases. These systems required very high cooling rates for the formation of a single-phase amorphous alloy, and there were not any quenching techniques available to reach these high cooling rates. In 1981 the first single phase amorphous Al-based alloy was produced in the Al-Fe-B and Al-Co-B systems [93]. Subsequently melt spun amorphous Al-Fe-Si, Al-Fe-Ge, and Al-Mn-Si alloys were developed. The problem with these alloys was that they were all extremely brittle [94, 95]. In 1987, Inoue's group discovered alloys containing ~80% Al that possessed good bending ductility. These alloys were in Al-Ni-Si and Al-Ni-Ge systems [96]. Following the innovation of these alloy systems, compositions have been effectively synthesized in ternary systems consisting of Al – early transition metal- late transition metal or Al-ETM-LTM systems (early transition metal = group IV-VI and late transition metal = group VII and VIII) [97, 98]. Additionally, ternary systems including Al-rare earth elements- transition metal have been successfully fabricated [99]. While there has been some success in producing Al-based glasses, the production of Al-based bulk metallic glasses has not been achieved.

2.12 Glass Formation

There has been much research that has been conducted on aluminum based metallic glasses and has focused on alloys containing 80-92% aluminum, 3-20% rare earth metals, and 1-15% transition metal additions [1, 5, 6]. These alloy compositions are significantly different from the majority of bulk glass forming alloys. As mentioned previously, most bulk forming alloy systems contain 20-30 % of a small atom. There has been recent work conducted on Al-based systems with reduced aluminum contents [100, 101]. In the case of most aluminum systems, the small atom is generally a late transition metal atom, which accounts for 1-15% of the alloy. Even though a well-defined L-S pair correlation has been shown to exist in the Al-TM-Ln alloy [8], aluminum based glasses have a weaker backbone structure than for bulk glass forming alloys. The maximum thickness reported for aluminum-based glasses is in the range of a hundred micrometers, when produced by melt spinning of ribbons. The maximum thickness of bulk glass forming alloys is in the range of several tens of millimeters, and can be produced by casting of ingots.

2.13 Amorphization Mechanisms

The amorphization process is generally described by the suppression of two kinetic mechanisms, seen in Figure 2-21, nucleation and growth. For a nucleation-controlled mechanism, the alloy is quenched from the melt sufficiently fast for the suppression of the nucleation reaction. If this nucleation reaction is suppressed, the atoms are not able to arrange themselves into clusters larger than a critical cluster size that would serve as an origination site for crystallization. When the alloy is heated a

clear glass transition will be present, as the growth process (and subsequent crystallization) will be delayed until after the nucleation reaction is underway. For a growth controlled mechanism of amorphization, a small number of clusters will form during cooling from the melt, but the increasing viscosity of the super-cooled liquid near T_g, keeps these clusters from growing. These pre-existing crystallites will rapidly grow when the alloy is heated back to Tg, and no super-cooled liquid region will be present because crystallization will occur at T_g [102].

2.14 Systems

As previously mentioned, it has been observed that for a glass to form in a given alloy composition there are three empirical rules for glass formation [87]: 1) have a multi-component system, 2) the atoms should have different atomic sizes > 12%, and 3) the atoms should have a large negative heat of mixing. Aluminum based amorphous alloy have been found to follow these rules as well. As seen in the literature, there are in general, three classes of ternary aluminum alloys: aluminum-late transition metal-early transition metal, aluminum-transition metal- metalloid, and aluminum-transition metal-rare earth metal. For the Al-late transition metal-early transition metal systems (Al-ETM-LTM), the early transition metal (ETM) atoms are Ti, Zr, Hf, V, Nb, Ta, Cr, Mo, and W and the late transition metals (LTM) are Cu, Fe, Ni, and Co.

Although aluminum based metallic glasses have not been produced, aluminum based amorphous alloys have been fabricated, by rapid solidification in ribbon form, by mechanical alloying in the powder form, and other methods. For the formation of Al-based glassy alloys the same empirical rules for glass formation in bulk glass forming

alloys tend to apply. Glass formation is favored for multi-component systems. A large negative heat of mixing for the different elements and an atomic size mismatch of greater than 12% are necessary for glass formation. One difference between aluminum based glasses and bulk glass formers is that aluminum based glasses often form in systems that do not have a deep eutectic, which is common for bulk glass forming alloys. In fact, aluminum-rare earth binary systems have the best glass formers at compositions of hypereutectic compositions [5].

2.15 Processing

There are several methods of producing amorphous aluminum alloys, almost as many techniques as for producing bulk amorphous alloys. [1, 17-19]. The most promising techniques for producing amorphous samples for engineering applications appear to be by either rapid solidification or by deformation. Currently the rapid solidification method has only been successful at producing ribbon samples with a thickness of less than a millimeter. Deformation induced amorphization has been successful a producing amorphous powders, but there has been no successful attempt to fully consolidate these powders and still maintain the amorphous structure. In order for these amorphous samples to be made into bulk samples it is necessary to develop new compositions that will require a much lower critical cooling rate and high thermal stability, or it will be necessary to develop new processing methods capable of scaling up the size of marginal glass formers. In order to do this it will be necessary to better understand the amorphization and crystallization mechanisms. Additionally

understanding the local atomic structure could lead to a way to manipulate the atomic structure that would make the aluminum alloys strong glass formers.

2.15.1 Rapid Solidification

One of the most common methods used to produce amorphous aluminum alloy samples is by rapidly solidifying the alloy by melt-spinning ribbons. As previously mentioned, the melt-spinning process is capable of achieving very high cooling rates, about 10^5 to 10^6 K/s, but the sample size is limited to less than 50 μm. Melt-spinning is one of the few rapid solidification processes that is capable of producing completely amorphous specimens. Because of this, melt-spun ribbon samples are frequently used in the investigation of the properties for these alloys.

2.15.2 Metallic Mold Casting

Metallic mold casting has been employed as a method of producing larger aluminum based samples via the rapid solidification process [5]. This process is capable of producing 0.2 x 5 mm sheets of amorphous $Al_{84}Ni_{10}Ce_6$. These thick sheet samples were prepared by injection casting of the melt into copper molds with the desired sheet dimensions. Attempts to cast larger samples resulted in crystalline phases being present in the material. Figure 2-22 shows the XRD patterns of sheets produced with different thicknesses, and it can be seen that the 0.2 mm thickness sample appears to be amorphous on both the surface and on the inside of the sample, as seen from XRD. Figure 2-23 shows the DSC data of the same sheets. Again in the 0.2 mm sample, the DSC curve appears to confirm that the sample is amorphous based on the fact that DSC shows a

supercooled liquid region that is the same as the melt-spun ribbon and with the same crystallization behavior.

2.15.3 Deformation

Research has also been conducted on the formation of amorphous materials through solid-state reactions, such as mechanical alloying of powders. This technique could be used to form amorphous alloys with larger dimensions than are capable of being produced through rapid solidification by consolidation of the amorphous powders. Mechanical alloying is a solid state reaction in which a great amount energy being applied to the elemental powders to introduce defects and cause the steady refinement of the grains within the alloys until an amorphous structure is produced [20]. The glassy structure forms through an interdiffusion process, which occurs at low temperatures in the layered composite structure of the powder, which forms in the early stages of milling. Extended milling reduces the thickness of the layers until the layers have completely interdiffused. Figure 2-24 shows an XRD pattern of mechanically alloyed $Al_{85}Y_8Ni_5Co_2$ powders after being milled for increasing amounts of time [103]. Once amorphous powders have been produced, they can be consolidated into scaled up samples with properties similar to those of the amorphous powder [4]. The properties of the bulk sample that is produced by consolidation of the mechanically alloyed powder will then be dependant on the consolidation parameters, such as time, temperature, and pressure. These parameters will affect the microstructure. For example, consolidation at high temperatures can cause partial or complete crystallization. This effect is shown in Figure 2-25.

2.16 Structure

Since aluminum based bulk metallic glasses have not yet been produced, and because aluminum based metallic glasses have different composition between the base element and the solute elements, it is important to know and understand the local structure of these glasses in order to produce bulk specimens and understand how the local environment affects the macroscopic properties. Pulsed neutron and x-ray scattering have been used to study Al-RE-TM systems. Analysis of $Al_{90}Fe_xCe_{10-x}$ revealed strong interactions near the first coordination shell of Fe [104, 105]. This revealed that the Fe-Al bond lengths were shortened by 8%, and had a 45% reduction in coordination number as expected from the dense-random packing (DRP) model. The Ce-Al bonds were also shortened, by 5% and showed a 13% reduction in coordination number. These strong interactions were explained as an increase in covalency between the ions and a reduction of their metallic character. Similar studies were performed on $Al_{87}Ni_7Nd_6$ that showed an 8% reduction in bond length for the Ni-Al bond [106]. In terms of the electronic structure, this could be due to electrons with the *sp* character in Al are transferred to the *d* states of Ni atoms. From these studies, it can be observed that the interaction between Al and the solute TM is an important factor in glass formation and plays a large role in the local environment.

2.17 Weak (marginal) glass former vs. BMGs

While there are three general rules for metallic glass formation, not all materials exhibiting these three rules can be easily formed into metallic glasses. The empirical rules do have a theoretical basis [107, 108], but there capabilities of predicting new

glasses are limited. Bulk glass-forming alloys typically have critical cooling rates of less than 100 K/s, while alloys that are not bulk glass-forming alloys, or ordinary amorphous alloys, have much higher critical cooling rates. One feature of bulk glass-forming alloys is the ratio of there atomic sizes. BMG's typically have the largest element as the base element, with the smallest element accounting for the next largest percent, and the middle-sized element accounting for the smallest minority. Ordinary amorphous alloys typically have a medium sized element as the base element, with larger and smaller elements accounting for the minority. For an alloy to become a bulk glass-former it is necessary for it to have slow atomic diffusion and reduced complexity (entropy) differences between the undercooled liquid and crystalline state. Given these favorable factors, a relatively low liquidus temperature is also desirable in reducing the amount of undercooling needed before crystallization occurs [8].

Because the normal mode for glass-formation is cooling a liquid, the glass-forming ability has been described by the cooling behavior of the liquid. The cooling behavior of the liquid can be described as "strong" or "fragile" when relating it to the glass-forming ability [16, 109, 110]. Stronger liquids will have good glass-forming ability, and in metallic glasses, they will form bulk metallic glasses. The opposite is true for more fragile liquids. This fragility can be determined by measuring the viscosity of the liquid as it cools. Strong liquids are several orders of magnitude more viscous at high temperatures relative to T_g, and as they cool, their viscosity gradually increases. Their high liquid viscosity helps to prevent the atoms from ordering themselves during cooling. The more sharply the viscosity increases as the temperature approaches the glass-transition temperature, the more fragile the liquid. Figure 2-26 shows a plot of the

viscosity of many different liquids as temperature is decreased to T_g. The larger the deviation from Arrhenious behavior, the more fragile the liquid becomes. The inset shows that the specific heat capacity increases more for fragile liquids, than for strong liquids as well. From this graph it can also be seen that the glass-transition temperature has been defined as the temperature at which the logarithm of viscosity is equal to 13 poise. This viscosity corresponds to a failure of the material to withstand shear stress for more than a few minutes [110]. Because of this, it can be seen that the shear modulus also plays an important role in the glass-forming ability. More specifically, the ratio of the shear modulus to the bulk modulus, or Poisson's ratio, is an important factor in glass-forming ability. Materials having a large Poisson's ratio will have a small shear modulus to bulk modulus ratio. These materials will in turn have a large fragility and a lower glass-forming ability.

2.18 Thermal Stability

2.18.1 Crystallization

The crystallization process of amorphous aluminum alloys has been studied by many different means of characterization. These include, but are not limited to, DSC, XRD, transmission electron microscopy (TEM), and neutron diffraction. For each of these experiments, the information is gathered in a different way, and with them, it is possible to truly understand how the crystallization process occurs and how the local structure is affected. Figure 2-27, shows a typical DSC curve for an aluminum alloy (in this case is $Al_{88}Y_7Fe_5$) that was rapidly quenched by melt-spinning of ribbons [102]. From this DSC we can see that the alloy remains stable until its primary crystallization

temperature, in this case the crystallization is of fcc aluminum nanocrystals at 273^{o}C. After this crystallization, the alloy remains stable until the temperature reaches the next crystallization event. This occurs at around 380^{o}C for this alloy and it corresponds to the crystallization of the remaining amorphous phase into intermetallic phases. Following this crystallization event, continued heating will results in various metastable phases evolving from the different phases present until the alloy finally melts. Figure 2-28 shows how important the composition of the alloys is in terms of its crystallization [24]. As the composition is gradually changed from $Al_{93-x}Ni_xGd_7$ the primary crystallization temperature shifts to higher temperatures until it disappears and is replaced by a glass transition temperature at the composition of $Al_{85}Ni_8Gd_7$.

By consolidating amorphous powders at temperature and pressure, and then examining the microstructure via TEM, it is possible to study the morphology occurring during crystallization. This gives insight into the microstructure of bulk materials that started as amorphous powders. TEM analysis during consolidation of $Al_{85}Ni_5Y_8Co_2$ is shown in Figure 2-9. At temperature well below the glass transition temperature the microstructure remains amorphous, which is manifested in a lack of features in the TEM image. As the temperature of consolidation is increased to temperatures near the glass transition temperature, fcc-Al precipitates begin to form in the amorphous matrix [4]. Consolidation at higher temperature leads to additional fcc-Al precipitates and the formation of Al_3Y precipitates. These precipitates are continuing to grow from 10-30nm at 523K to 100 -150 nm at 577K. An additional phase appears as temperature is further increased. These phases contribute to increasing strength of the consolidated samples and act as a nanoscale composite with very high strength.

Neutron diffraction is another way of studying the crystallization, but with neutron diffraction it is possible to examine the local atomic ordering of the alloy as it is heated from room temperature through the crystallization. Figure 2-29 shows neutron diffraction studies on $Al_{87}Ni_7Nd_6$ metallic glass, which illustrates that, the prepeak (indicative of short-range ordering) remains even after crystallization of some of the amorphous matrix begins, and it actually gets narrower at higher temperatures. This means that the chemical clusters expand with heating, and that the clustering would likely remain in the liquid as well [106, 111]. Figure 2-30 shows the PDF of the same composition at different temperatures from 100°C to 500°C. From this PDF analysis it is possible to see that the local environment significantly changes with temperature, due to the crystallization process [106, 111]. This is seen by the drop in the peak at around 2.6 nanometers corresponding to three different Al pairs which make up the peak: Al-Al, Al-Ni, and Al-Nd. The drop in the peak signifies a change in the amounts of these pairs present. From neutron diffraction it is possible to see how the crystallization process affects chemical short-range ordering and the local structure in the alloy.

2.18.2 Nanocrystallization

Another interesting feature of the crystallization behavior of amorphous aluminum alloys is that some compositions have a tendency to crystallize into nanometer sized clusters or grains. When the nanocrystallization is controlled, either by quenching at a cooling rate below the critical cooling rate [112], by mechanically alloying until the desired phases are present [113], by controlled annealing of an amorphous sample [114], or by consolidating glassy powders at temperatures just above T_x, one can further

increase the strength of these alloys [44], as seen in Figure 2-31. These aluminum alloys with extremely high strength are of high engineering importance due to the fact that aluminum has a low density (about $3g/cm^3$) giving it a very high strength to density ratio [44] as seen in Figure 2-31.

This nanocrystallization process has been described as a growth controlled process from pre-existing clusters or quenched-in defects. This would occur if the sample were cooled at a rate just below the critical cooling rate, and the rapidly rising viscosity during cooling prevented the clusters from developing further [102]. TEM has shown that nanocrystals can be growing at temperatures below the observed primary crystallization in DSC measurements [115] nanocrystals grow out of the initial clusters, but their growth is limited due to high particle density, 10^{21}-10^{22} m^{-3}, causing the impingement of diffusion fields from neighboring nanocrystals, which has been attributed to enhanced thermal stability [116].

2.19 Bulk Formation - What is being done?

Because of the limited success in scaling up amorphous aluminum alloys, there has been a refocusing of the research on identifying why aluminum based systems have not been successful in producing bulk samples. It has been determined that the critical cooling rate for vitrifying aluminum based glasses is much higher than those of bulk glass forming alloys. This can be attributed to the fragility of the liquid. Bulk glass forming alloys typically have significantly greater densities (when compared to their crystalline counterparts) than ordinary amorphous alloys. The difference in density between the amorphous and crystalline phases of bulk glass formers is often 0.3-0.54% whereas the

difference for ordinary amorphous alloys is close to 2% [117, 118]. This difference has been attributed to chemical short range ordering in bulk glass formers, and is likely due to explicit atomic arrangements and relations in the liquid phase. Systems without these interactions in the liquid phase are less likely to have high enough solid/liquid interfacial energy and low enough atomic diffusivity to adequately suppress the nucleation and growth of the crystalline phases [53].

Because of the difficulties in forming a bulk aluminum based glassy alloy, there has been increased attention into determine specific glass forming criterion. This is a shift away from using empirical rules for guiding the selection of components for glass forming candidates. The model proposed by Egami [119] specifies that a glass will form when the local atomic structure becomes unstable. Egami extends the geometrical criterion for melting due to local structural instability to the dense random packed structure and glass formation. This model says that when the strain produced by adding additional solute atoms, which are different in size compared to the solvent atoms, reaches a critical value, local instability will be achieved. This critical value occurs when solute atoms that are different in size from the solvent atoms are added. With the addition of each individual atom a strain is produced, and the volume is changed. When the volume is significantly changed enough to change the coordination number (for example, from 12 to 13 for an f.c.c. material), the structure becomes locally unstable. At this point, an amorphous structure can be attained. Factors that can improve the glass-forming ability include: increasing the atomic size differences of the different elements, increasing the number of components, increasing the interactions between large and small atoms, and increasing the repulsive interaction between small atoms [10].

This model has been extended by Senkov and Miracle [120] to distinguish between solute atoms occupying substitutional and interstitial sites. This is because as the solute atoms become increasingly small compared to the solvent atom the substitutional occupancy becomes unstable. Interstitial occupancy increases the minimum critical concentration for the local instability necessary to form an amorphous microstructure. When the radius ratio of solvent atom to solute atom is plotted against the minimum critical concentration required to achieve a critical strain, a concave-up plot is produced, as seen in Figure 2-32 [118]. When a similar plot of radius ratio versus solute concentration is mapped for real glasses, it is found that bulk metallic glasses produce a similar concave-up shape, as seen in Figure 2-33 for Zr-based metallic glasses. When ordinary metallic glasses are plotted, they produce a concave-down shaped graph, as seen in Figure 2-34 for Al-based glasses. This model could be very useful in predicting and fabricating new classes of metallic glasses, especially for classes of metallic glasses that cannot yet be produced as bulk metallic glasses.

2.20 Conclusions

Amorphous aluminum alloys have been successfully produced in many compositions, but there have been no successful efforts in the production of aluminum based bulk metallic glasses. This is due to the marginal glass-forming ability of aluminum-based alloys, and the high critical cooling rate that is necessary for their production by common means. Their structure has been studied to enhance the understanding of these alloys. Models have been proposed to attempt to explain the local structure and predict methods that could be used to increase their glass forming ability.

Through studies of the crystallization process, it has been found that by partially crystallizing the amorphous phase, a nanocrystalline phase plus amorphous matrix composite can be produced with enhanced engineering properties. For amorphous aluminum alloys to successfully be scaled up it will be necessary to find new compositions that have much greater glass-forming ability or to find new processing methods that can circumvent the crystallization process for alloys with existing or new compositions. If this is achieved, a wide variety of applications could be possible for these metastable amorphous and nanostructured alloys that could prove to be of great engineering importance.

Chapter III: Experimental Details

3.1 Overview of Experiments Conducted

The primary goal of this dissertation was to examine the processing, structure, and properties of amorphous aluminum alloys. Experiments were conducted to gather information about these materials, and careful attention was paid to select experiments that would provide both new and useful information regarding this class of materials. Each experiment resulted in unique information that was correlated to other experimental results both in this dissertation and in the literature to provide a comprehensive examination of amorphous and nanocrystalline aluminum alloys prepared through mechanical alloying. The synthesis by mechanical alloying, differential scanning calorimetry, x-ray diffraction (both synchrotron and conventional), and neutron diffraction were key experimental methods used in this research.

3.2 Alloy synthesis and Materials

The Al-Y-Fe system was chosen for the research performed in this dissertation. This system was chosen because similar melt-spun ribbons have studied by several other research groups [1, 11, 99] and the current results may be compared and contrasted to the literature. This ternary system was also chosen because of its relative ease of glass formation. In addition, Fe is a typical contaminant from the ball-milling process, and in order to minimize this contamination effect a composition containing Fe was chosen.

Elemental powders of Al, Y, Fe, Ni, Ti, Cu, and Co, with purities of 99.97% for Al and 99.9% for all others were mixed and ball milled using a SPEX 8000D mixer/mill

with hardened-steel vials and stainless-steel grinding balls with a ball to powder weight ratio of 10:1. Powders were milled continuously for 45 hours in an argon atmosphere. After 45 hours of ball-milling the powder was collected inside of an argon atmosphere glovebox. In order to control the Fe contamination, each alloy examined was filled in a clean vial with new grinding balls and milled for 45 hours. For each successive batch the vials were not completely cleaned for a given composition. This was done to coat the grinding media (vials and grinding balls) with the alloy and obtain more consistent results (composition) from batch to batch.

For the consolidation efforts in this study, the selected alloy composition is $Al_{79}Y_7Fe_8Ni_3Ti_2Nd_1$. Powder was milled continuously in the argon atmosphere. After the ball-milling, the powder was collected inside an argon atmosphere glovebox and transferred into a steel compression die lubricated with high-temperature boron nitride lubricant. In order to prepare the green sample, the die was transferred to a Material Test System 810 (MTS Systems Corporation, Eden Prairie, MN) hydraulic load frame and heated under vacuum to 400°C at a rate of 20°C / min. Once the temperature was reached, the stress was increased to and maintained at 190 MPa for 3 hours. Subsequently, Ceracon forging was performed by Advanced Materials & Manufacturing Technologies, LLC (Carmichael, CA). The green samples prepared at UT were forged at two different temperatures, 420°C and 445°C. Samples forged at 420°C had to be forged 3 times in order to densify the preform, while samples forged at 445°C only needed to be forged one time for apparent densification.

3.3 Calorimetry

Differential scanning calorimetry (DSC) was carried out at a heating rate of 20 ºC/min. in a flowing argon atmosphere using two differential scanning calorimeters. For the results described in Chapter 4.1 a NETZSCH Instruments, Inc DSC 404C was used. This DSC was calibrated by melting standards of Al, IN, Zn, Sn, and Pb. For all other results a Perkin-Elmer Diamond DSC was used. This DSC was calibrated by melting standards of In and Sn. Heat treatments were also performed in the DSC by heating the powders at a heating rate of 20 ºC/min. to the desired temperature, at which they were held for 10 minutes and cooled to room-temperature at a cooling rate of 60ºC/min.

3.4 Structural Characterization

3.4.1 Laboratory X-ray Diffraction

Room-temperature laboratory x-ray diffraction patterns were obtained with a Philips X'Pert X-ray Diffractometer using Cu Kα radiation, $\lambda = 1.542$Å.

For the results in Chapter 4.1, *in-situ* high-temperature x-ray diffraction (HTXRD) was conducted during isothermal annealing of the ball-milled powders using a Panalytical X'PERT PRO θ–θ diffractometer with an X'Celerator position sensitive detector (2θ range = 36-46°) and Cu Kα radiation. The evolution of the diffraction patterns during annealing were measured at 633 K, below the primary crystallization temperature, in a He atmosphere every 5 minutes using the position sensitive detector.

3.4.2 Synchrotron X-ray Diffraction

For the results in Chapter 4.2 and 4.3, synchrotron XRD (SXRD) was performed using the 6-ID-C beamline at the Advanced Photon Source (APS) at Argonne National Laboratory on a high-energy beam line with a monochromatic wavelength of 0.12462 Å. A picture of the 6-ID-C beamline is shown in Figure 3-1. Samples were measured in an aluminum sample holder with a 1-mm circular hole and sealed using Kapton® tape. Beam size was 1 mm, and sample-to-detector distance was approximately 0.245 m. Images were recorded using a Mar345 image plate detector (3450x3450 pixels). A cerium dioxide powder standard was used to calibrate the sample to detector distance and refine instrumental parameters.

For the results in Chapter 4.4, SXRD was performed using the X-14A beamline at the National Synchrotron Light Source (NSLS) of the Brookhaven National Laboratory (BNL) [121, 122], Figure 3-2. A six-circle Huber diffractometer with a Xe–CO_2 filled proportional counter was employed with a 1×4 mm incident beam cross section [122]. Powders were sealed in a glass capillary tube, and heated inside a tube furnace [123]. The synchrotron beam was monochromated using a Si (111) crystal. The data was collected at an energy of 16.99KeV, and the wavelength (λ = 0.72982 Å) was calibrated by measuring a NIST LaB_6 standard (NIST SRM 660a - Line Profile LaB_6). Samples were heated at a rate of 0.14 °C/second, and data was collected at a rate of 0.005°/step and constant monitor counts per step. Diffraction patterns were collected at room temperature, 100, 200, 300, 325, 350, 375, 400, 425, 450, 475, 500, 550, and 600°C. Each diffraction pattern measurement required the sample to be held at temperature for

about 15 - 20 minutes. Phases were identified using Jade (Materials Data Inc., Livermore, CA, USA) phase identification software.

3.4.3 Neutron Diffraction

Neutron diffraction experiments were conducted on a bulk metallic glass sample, $Zr_{57}Nb_5Cu_{15.4}Ni_{12.6}Al_{10}$, subjected to uniaxial compression testing using the SMARTS instrument at the Lujan Neutron Science Center, Los Alamos National Laboratory. The geometric setup of SMARTS allows for simultaneous measurements in longitudinal and transverse directions. The diffraction data were collected using the time-of-flight technique for 4 hours at each stress level, ranging from 20 MPa to 1500 MPa and an unloaded condition at 20 MPa. Data were collected out to a maximum Q of 20.4 $Å^{-1}$. Measurements were performed such that the BMG sample was initially loaded to a stress of 20 MPa in order to hold the sample in the horizontal load frame. The sample was held at this stress while the diffraction measurement was conducted. After sufficient data was collected, the stress was increased to 500 MPa and this procedure was repeated. Data was collected at stresses of 20 MPa, 500 MPa, 1000MPa, 1500MPa, and an unloaded condition of 20 MPa. The macroscopic stress-strain behavior was also measured with an affixed extensometer for applied stresses ranging from 0 to 1500 MPa.

3.5 Pair Distribution Function Analyses

Because the size of the features studied during a total scattering experiment is small, it is necessary to perform measurements that measure as much scattering data as

possible. Due to the reciprocal nature of diffraction measurements, a large value of Q is needed to study small features.

Due to the high Q-space resolution necessary to produce quality total scattering measurements and PDF analyses, the most common X-ray sources cannot be used [65]. This is because x-ray tubes with copper targets, the most common targets, produce K_α x-rays with a wavelength of 1.544Å. This corresponds to a to a maximum Q range of about 8 $Å^{-1}$. High resolution measurements require $Q_{max} > 35$ $Å^{-1}$. Because of the limitation in Q-space of traditional x-ray generators, most measurements are performed at synchrotron radiation sources. Synchrotron sources produce intense, high energy x-rays (>2.5 GeV) are polychromatic, or they can be made monochromatic using a single crystal monochromator. The high-intensity, short-wavelength particles are necessary for accurate PDF analysis.

For measurements to be performed there are several conditions that must be properly tuned to obtain accurate results. The sample must be placed into a sample container or some other special environment. Special environments are used it if is desired to study the sample's structure at temperature, pressure, or other non-normal conditions. Sample containers are usually made of vanadium for neutron scattering because vanadium scatters neutrons almost perfectly incoherently. A measurement of the sample container without a sample is also necessary to be able to differentiate the effects of the container and the sample. This measurement will enable the user to subtract the information gathered from the sample from that of the container and other instrument background effects. The instrument is also calibrated to determine how well its measurements represent a known standard. From these measurements and corrections,

the measurements of the sample can be used to accurately determine the structure of the sample.

The elastic scattering intensity, I(Q), is measured as a function of the magnitude of the scattering vector $Q=4\pi\sin\theta/\lambda$. θ is the scattering angle and λ is the wavelength of radiation used. The scattering data was normalized and corrected, by subtracting the instrumental background and the background from the Kapton® film sample holder used in this study, from the measured data. The results were integrated to Q space by using the program FIT2D [124]. The integrated data were corrected for absorption, multiple scattering, fluorescence, and Compton scattering. The structure factor, *S(Q)*, was obtained according to the equation:

$$S(Q) = \frac{I(Q)}{N < f(Q) >^2} \tag{2}$$

where N is the number of atoms, *f(Q)* is the atomic scattering factor for x-rays averaged over the composition of the material.

Real space information about the local atomic structure can be obtained through the Fourier transform of *S(Q)* to the pair distribution function (PDF), *G(r)*:

$$G(r) = \frac{2}{\pi}\int_0^\infty Q[S(Q) - 1]\sin(Qr)dQ \tag{3}$$

where r is the distance from an average atom. The PDF gives the probability of finding an atom at a given distance from an average atom located at the origin. This real-space measurement technique is useful for probing the structure on the nanometer length scale, when the local structure is not consistent with the long-range averaged structure [35]. Therefore, PDF is particularly useful for the determination of local atomic structures of amorphous materials [33].

Chapter IV: Results and Discussion

4.1 Effect of Composition on Amorphization and Crystallization

This section presents the compositional effects of transition metals on the amorphization and crystallization of the $Al_{85}Y_7Fe_5TM_3$ system (TM = Ni, Co, Cu, and Fe) prepared by mechanical alloying of elemental powders. The TM additions have similar atomic sizes, but have different chemical interactions with the Al, Y, and Fe. The influence of the chemical composition of the amorphous phase on its thermal stability will be examined by studying the effect of various transition metal additions and by varying the transition metal to aluminum ratio for the system $Al_{85-x}Y_7Fe_5Ni_{3+x}$ (x = 0, 2, 4). The influence of nanocrystalline phases on the crystallization of the amorphous phase will also be discussed.

4.1.1 Effect of Late Transition Metals (LTM) on Amorphization Process

X-ray diffraction (XRD) patterns of the ball-milled $Al_{85}Y_{10}Fe_5$ and $Al_{85}Y_7Fe_5TM_3$ (TM = Ni, Co, Cu, Fe) alloys show that, after 30 hours of milling, all alloys contained evidence of nanocrystalline peaks superimposed onto a broad amorphous background, Figure 4-1. Although continued milling could change the amounts of amorphous phases [16], this study focuses on the comparison between the effects of different TM additions on 30 hours of ball milling.

The diffraction pattern of $Al_{85}Y_{10}Fe_5$ shows a broad amorphous background with crystalline peaks of Al and Al_2Y superimposed onto it. This diffraction pattern shows that it contains a significant amount of crystalline phase. The crystalline peaks were of

different intensities for the four different transition metal additions (3 atomic % TM replacing Y), indicating that there were different types/amounts of crystalline phases present in each alloy. The alloy with 3% Ni addition shows the least intense crystalline diffraction peaks followed by Fe, Co, and Cu additions. The diffraction pattern of $Al_{85}Y_7Fe_5Ni_3$ indicates that crystalline phases present in the amorphous matrix are Al and there is likely crystalline Fe present as well, but Fe could not be confirmed for these alloys because the locations of Al and Fe peaks overlap and additional peaks are too weak, compared to the background, to resolve. The pattern for $Al_{85}Y_7Fe_5Co_3$ shows that Al and Y crystalline phases are present in the amorphous matrix. For $Al_{85}Y_7Fe_5Cu_3$, Al and Al_3Y are present in the amorphous matrix. For the $Al_{85}Y_7Fe_5Fe_3$ alloy, the diffraction pattern revealed that Al and Fe are present in the amorphous matrix. The chemical interactions of the different transition metals with Al and Y seem to be the primary reasons for the varying amounts of amorphous phase for each alloy, since the atomic sizes of Ni, Co, Cu, and Fe are all within 3 % of each other (0.12459, 0.12510, 0.12780, and 0.12412 nm, respectively [125]). These radii assume a structural model of dense packing of atomic clusters, where efficiently packed solute-centered atomic clusters are maintained as local structural elements [68].

The heat of mixing between Al and Ni is the most negative among TM additions (-22 kJ/mol for Ni-Al compared to -19 for Co-Al, -1 for Cu-Al, and -11 kJ/mol Fe-Al) [126]. A large negative heat of mixing has been cited as a criterion for producing amorphous alloys [13]. For this reason, $Al_{85}Y_7Fe_5Ni_3$ was further investigated by modifying the Al content. The effect of increasing the Ni content at the expense of Al is presented in Figure 4-2. The intensities of the crystalline peaks weaken as the Ni content

is increased from 3% to 5% and 7%, while the Al content is reduced correspondingly. At 7% Ni, the remaining crystalline peaks disappear into the amorphous background. However, the second shoulder (at higher angle near 45°) of the amorphous background suggests the presence of nanoclusters or nanocrystalline phases within the amorphous matrix [127, 128].

4.1.2 Effect of LTM on Crystallization Behavior

Figure 4-3 shows a typical DSC trace for the mechanically alloyed powder of $Al_{81}Y_7Fe_5Ni_7$. DSC scans showed multiple exothermic events, but the focus of this paper is on the first exothermic event. Table 4-1 summarizes the results of the DSC scans (at a heating rate of 20 K/min) for the different alloy compositions as well. The onset of crystallization temperature was extrapolated from the results of the DSC scans. The primary crystallization temperatures, T_x, show that 3% additions of Ni, Fe, and Co produce a similar T_x, within about 2 %, (612 K, 615 K, and 619 K). However, for the alloy with a 3% Cu addition, a T_x of 590 K was measured, which is about 22 to 29 degrees different from that with Ni, Fe, and Co. The DSC scans were used to determine the enthalpies of the crystallization (ΔH_x) of the different alloys, as shown in Table 4-1. The ΔH_x values for the 3% transition metal additions are close to those reported for the primary crystallization of fcc-Al from the amorphous matrix of mechanically alloyed powders of $Al_{85}Ni_{10}Y_{2.5}La_{2.5}$ (2.2 kJ/mol) [129] and $Al_{88}RE_8Ni_4$ (1.8kJ/mol) [130]. *In-situ* HTXRD was performed to further study the crystallization, and it was determined that the event observed in the DSC is related to the growth of the pre-existing nanocrystals. This will be discussed later in section 4.4.2.

Isothermal DSC scans were performed on $Al_{83}Y_7Fe_5Ni_5$ at temperatures of 623, 633, 643, and 653 K to further examine the crystallization kinetics. The powders were heated at 20 K/min to a temperature, 20 degrees below the annealing temperature, and then were heated at 5 K/min to the annealing temperature, at which time the isothermal hold began.

The isothermal annealing results were used to obtain the activation energy, E_a, for the primary crystallization process according to the Johnson-Mehl-Avrami (JMA) theory [131]. The volume fraction transformed, *x*, at a time, *t*, is given by:

$$x = 1 - \exp[-K(t-\tau)^n] \quad t > \tau \tag{4}$$

where τ is the incubation time at the isothermal temperature for nucleation to begin, and *K* is the rate constant, which depends on the nucleation rate and the crystallization rate. K may be expected to show an Arrhenius temperature dependence, $K = K_0\exp(-E_a/RT)$ The transformation rate (dx/dt) is proportional to the heat flow rate (dH/dt), which can be found from the DSC data. At $t = t_p$, where t_p is the time of the transformation peak maximum, dx/dt is a maximum, and $(dx^2/dt^2) = 0$. Then $(n-1)/n = [K(t_p - \tau)]^n$. From this we obtain:

$$\ln(t_p - \tau) - E_a / RT = \text{constant} \tag{5}$$

where is the time of the transformation peak maximum, R is the ideal gas constant, and T is the isothermal temperature. E_a is the effective activation energy for crystallization, which can be obtained by plotting $\ln(t_p - \tau)$ versus (1/T) [2, 103], as shown in Figure 4-4. E_a for the ball-milled $Al_{83}Y_7Fe_5Ni_5$ powder was found to be 310 kJ/mol. This value is larger than the activation energies of 164-285 kJ/mol previously reported for $Al_{85}Y_8Ni_5Co_2$, $Al_{93-x}Ni_xGd_7$, $Al_{90}Fe_{10}$, $Al_{85}Ni_{15-x}Y_x$, and $Al_{80}Y_{15}Ni_5$ [24, 103, 113, 132, 133], but lower than 425 kJ/mol for $Al_{85}Ni_5Fe_2Gd_8$ [2]. The larger values imply more stability against crystallization at temperature below T_x. Table 4-2 summarizes the activation energies for various amorphous aluminum alloys in the literature and the method by which it was determined, i.e., JMA or Kissinger analyses [131, 134]. The activation energy shows a wide range of values for the different amorphous aluminum alloys in the literature, which is likely due to the different components and compositions of the various alloys. The comparison also shows that the processing method, ball-milling or rapid solidification, may also have an effect on the amount of energy required for the crystallization process.

Finally, *in-situ* time-resolved high-temperature x-ray diffraction measurements were performed during isothermal annealing of the $Al_{83}Y_7Fe_5Ni_5$ alloy to further study the crystallization process. Figure 4-5 presents the evolution of the diffraction patterns during the isothermal annealing for 95 minutes at 633 K. It shows the formation and growth of an intermetallic phase along with the growth of the aluminum crystalline phase from the amorphous matrix. Figure 4-6a presents the changes in integrated peak intensities of Al_7Fe_5Y intermetallic phase during the anneal. The peak appears after about 25 minutes and continues to grow until about 75 minutes of annealing, after which

it seems to saturate. Figure 4-6b indicates that the aluminum phase begins to grow after about 45 minutes. The results show that crystallization observed in the DSC curve (with the activation energy of about 310 kJ/mol) is a combination of the crystallization of the amorphous aluminum matrix and the formation and growth of intermetallic phases. This convoluted crystallization step would explain the higher energies for the primary crystallization than some of the previously reported values [24, 103, 113, 131, 132]. X-ray diffraction was performed at room temperature with wider 2θ angle coverage, using the same method as the initial room-temperature XRD measurements, to verify the phases present after the *in-situ* isothermal annealing. The results, shown in Figure 4-7, confirmed the presence of fcc-Al and Al_7Fe_5Y

4.1.3 Discussion of the Effect of Composition

The results suggest that the chemical composition of the amorphous phase strongly influence thermal stability of the alloys studied. When the T_x temperatures for Al-Y-Fe-TM are compared to the eutectic temperatures of the aluminum rich binary compounds [135] of Al_9Co_2, Al_3Fe, Al_3Ni, and Al_2Cu, in Table 4-1, the alloys with the highest eutectic temperatures also had the highest T_x. This trend suggests that the effect of chemical interactions play a key role in the thermal stability of the Al-Y-Fe-TM alloys, with Co greater than Fe, followed by Ni and Cu. Also shown in Table 4-1 are the crystallization temperatures of $Al_{83}Y_7Fe_5Ni_5$ and $Al_{81}Y_7Fe_5Ni_7$. The decrease in the Al/Ni ratio show a large increase in T_x from 612 K, to 668 K, and then to 672 K as the Ni content increases from 3 to 5 and 7%, respectively. This indicates that the increase in Ni additions replacing the Al stabilizes the amorphous phase against crystallization.

The observation that most of the alloys produced in this work have slightly higher enthalpies of crystallization than previously reported for amorphous alloys, likely results from the presence of nanocrystalline phases. $Al_{83}Y_7Fe_5Ni_5$ and $Al_{81}Y_7Fe_5Ni_7$ show higher enthalpies of crystallization than the 3% TM additions, Table 4-1. The increased thermal stability is likely due to deviations in the chemical composition of the amorphous phase from the original composition, which results from the varying amounts of amorphous and nanocrystalline phases in the alloy. As the composition of the alloy shifts toward lower Al contents, the crystallization temperature increases. As the amount of Al is reduced, the enthalpy of crystallization increases, which suggests that the amount of amorphous phase in the sample, has also increased when the alloy contains smaller amounts of Al [90].

It has been shown that ball-milling-induced nanocrystallization can occur due to atomic displacement under the high stress in the deformation process, and these nanocrystals can make the amorphous phase more stable against thermally activated crystallization of the amorphous phase [136]. With the nanocrystalline phase, the free energy of the material increases and an increased amount of energy is needed to reach the stable state [137]. As the high density ($>10^{21}$ / m^3) of nanocrystalline particles grow at temperatures below T_x, they reduce the number of nucleation sites. As the nanocrystals grow into the amorphous matrix, they could shift the chemical composition of the amorphous phase, which could, in turn, stabilize the amorphous phase and hinder crystallization [116, 136-138]. The particles remain in the nanometer size range due to the overlapping of diffusion fields of the growing grains [116, 139]. Similarly it was observed in this study that amorphous plus nanocrystalline alloys of Al-Y-Fe-TM showed

high crystallization temperatures and larger activation energy than previously reported. The presence of nanocrystalline phases in Al-Y-Fe-TM alloys could shift the composition of the amorphous phase away from that of the overall composition, and the changes in the composition caused an increase in thermal stability of the amorphous phase.

4.2 Chemical Short-Range Ordering in $Al_{85}Y_7Fe_8$ and $Al_{83}Y_7Fe_8Ti_2$

The glass-forming ability of metallic glasses can be increased with the addition of certain elements in small amounts, or microalloying [25-28]. It has also been suggested that microalloying can increase the thermal stability of metallic glasses by suppressing the precipitation of crystalline phases during heating of the amorphous phase [26, 27, 140]. In particular, microalloying with Ti has been shown to effectively improve both the glass-forming ability and the thermal stability of these alloys presumably by changing the local order to hinder the precipitation of the fcc-Al phase [30], but the mechanism for this change is not fully understood. Recent reports have suggested a model for short-range order in amorphous alloys that is comprised mostly of tightly bonded clusters that are similar to crystalline materials, rather than a local structure that is comprised of a dense random packing of atoms [141, 142]. The basis of these models is the efficient packing of space by overlapping close-packed clusters that fill space in three dimensions [68]. In these clusters, the order is limited to a few atomic distances. The clusters are connected to each other but are randomly oriented so as to limit ordering. These models indicate that densely-packed clusters enhance the glass-forming ability of metallic materials. In particular, the addition of Ti to Al-Y-Fe alloys has been found to result in a well-defined

cluster structure forming around solute atoms, even with additions of Ti as small as 0.5%, due to strong interactions of Ti with Al [143].

It is commonly found that Al-Fe-Y glasses often appear amorphous when characterized by laboratory x-ray diffraction (XRD), more specifically, lacking the typical diffraction peaks observed in crystalline materials. However, further examination by isothermal differential scanning calorimetry (DSC) reveals that some aluminum-based glasses are comprised of a very fine nanocrystalline structure, and the crystallization event corresponds to a grain coarsening reaction, as opposed to a nucleation and growth reaction, which would occur in amorphous materials [23, 31, 128]. However, the addition of 2% Ti to Al-Y-Fe alloys dramatically improves the glass forming ability and changes the nature of the local structure of the alloy into an amorphous one, and the isothermal DSC curve for this alloy shows a peak that is characteristic of a nucleation and growth reaction occurring during crystallization [30].

Examination of the local atomic structure of Al-Y-Fe and Al-Y-Fe-Ti alloys can provide further information about the nature of the clustering developed in these alloys and the role of Ti on enhancing the glass-forming ability. The pair distribution function (PDF) is an analysis method that utilizes total scattering (i.e., Bragg scattering plus diffuse scattering) to accurately determine the local atomic structure [65]. The PDF can be used for materials that lack long-range order, or where the short-range structure is not reflected in the long-range order of the crystal. The PDF is a one-dimensional function showing the atom-atom distances of all of the atoms throughout the material. The PDF is represented in real space, rather than the reciprocal-space powder diffraction data [65]. This approach has been widely used for studying the structures of glasses and liquids

since the 1930s [34]. This real-space method is one of the small number of experimental techniques that can be used to probe structure on the nanometer length scale, when the local structure is not consistent with the long-range globally-averaged structure [35]. PDF studies have provided details about the local ordering [36], free volume [37, 38], and mechanical behavior [37, 39, 40] of BMGs.

This section presents the experimental investigation on the influence of the addition of a small amount of Ti on the changes in local atomic ordering in the amorphous state. The study focuses on examining the difference in the amorphous structures at the local atomic level when the structure is modeled with local arrangements of tightly bonded clusters (similar to the alloys' crystalline counterpart structures) are randomly distributed and oriented. The local atomic structures of $Al_{85}Y_7Fe_8$ and $Al_{83}Y_7Fe_8Ti_2$ will be presented and the influence of Ti on the amorphous phase will be discussed by using synchrotron x-ray diffraction results and pair distribution function analyses.

4.2.1 X-ray Diffraction Analysis

Figure 4-8 presents the x-ray diffraction data showing the effect of adding Ti to an Al-Y-Fe alloy. The diffraction patterns reveal that as 2% Ti is added, while removing Fe, there is little change in the microstructure. The diffraction pattern shows that $Al_{85}Y_7Fe_8$ and $Al_{85}Y_7Fe_6Ti_2$ contain nanocrystalline Al and Fe phases. When the Ti content is further increased to 4% (while reducing the Fe content), the XRD pattern shows the diffraction peaks disappear and the structure becomes amorphous. This indicates that Ti affects the glass-forming ability, but there is a minimum amount necessary to form the

amorphous phase. When 2% Ti is added, while reducing the Al content, the XRD pattern indicates that the microstructure is amorphous. This further indicates that the addition of Ti improves the glass-forming ability. This also shows that the amount of base element (Al) is also an important factor in the glass-forming ability, and the overall composition influences the effect of the microalloying addition. Figure 4-8(b) shows the structure factor for $Al_{85}Y_7Fe_8$ and $Al_{83}Y_7Fe_8Ti_2$. These two alloys were chosen for further examination because of the significant differences in structure, with the minimal change in composition. The structure factor of $Al_{85}Y_7Fe_8$ shows broad diffraction peaks that were indexed as Al and Fe. On the other hand, the $Al_{83}Y_7Fe_8Ti_2$ alloy shows only weak broad diffraction peaks superimposed onto an amorphous background. These weak peaks were indexed as Fe. The results show that replacing 2% Al with Ti has affected the ability to form an amorphous phase, which is consistent with the results previously reported [30, 124, 143, 144]. For example, the addition of Ti to Al-Fe-Y melt-spun ribbons caused the structure to change from a fine nanocrystalline material to an amorphous material [30, 144].

Furthermore, a close observation of the structure factor data, Fig. 4-8(c), reveals a small 'prepeak' in the $Al_{85}Y_7Fe_8$ and $Al_{83}Y_7Fe_8Ti_2$ data. The integrated area of the prepeak for $Al_{83}Y_7Fe_8Ti_2$ is about 70% larger than that of $Al_{85}Y_7Fe_8$. The prepeaks; centered at about 1.4 $Å^{-1}$ and 1.45$Å^{-1}$ for $Al_{85}Y_7Fe_8$ and $Al_{83}Y_7Fe_8Ti_2$, respectively; are characteristic of a cluster structure consisting of unlike atoms [145]. A similar prepeaks has been observed in many other Al-based amorphous alloys [104-106, 146]. From the position of this prepeak it is possible to estimate the average separation between clusters [36] according to the equation $L(Å) \sim 1.23(2\pi) / Q(Å^{-1})$. In this equation, L is the average

separation between clusters, and Q (scattering vector, $Q=4\pi \sin\theta / \lambda$) is the position of the prepeak. The prepeaks observed in Fig. 4-1(c) correspond to a correlation length, L, of ~ 5Å.

4.2.2 Pair Distribution Function (PDF) Analysis

The pair distribution function (PDF) analyses of the two alloys are shown in Figure 4-9. The PDF of $Al_{85}Y_7Fe_8$ shows multiple broad coordination shells, indicating ordered arrangements of atoms over long distances. This is consistent with the broad diffraction peaks observed in the reciprocal space data. The small oscillations seen in the PDF are due to termination and other errors. The PDF of $Al_{83}Y_7Fe_8Ti_2$ shows three broad coordination shells, revealing the nearest neighbor distances, beyond which the PDF shows very low intensity oscillations around zero indicating no significant order.

Based on previous studies on the amorphization and crystallization of aluminum-based alloys, specific precursor and crystallization product phases were used to approximate the local structure of the alloys. The crystalline phases which best filled the space of the first coordination shells of the PDFs were used to approximate the short-range order in these two alloys, displayed in Figure 4-10. Our approximation shows that the structures that most closely describing $Al_{85}Y_7Fe_8$ are Al (F m -3 m; a = 4.047), Fe (Im-3m; a= 2.876), and Al_3Y (R -3 m; a = 6.156, c = 21.084). On the other hand, the structure of $Al_{83}Y_7Fe_8Ti_2$ was best described with Al, Al_3Y, and Al_6Fe (C m c 2_1; a= 6.464, b = 7.440, c = 8.779). With the Ti addition, it was apparent that different crystal structures were necessary to properly fill these shells which indicated that the local atomic structure had changed. Because of the relatively small amount of Ti present in the

$Al_{83}Y_7Fe_8Ti_2$ alloy, Ti-containing phases or compounds were not observable. The primary difference between these two alloys is that the alloy with the 2% Ti addition has enhanced the interaction between Al and Fe to the point that Al_6Fe-like clusters are formed in the amorphous alloy. The formation of the Al_6Fe phase will be discussed in the following section.

Figure 4-11 shows the difference pair distribution function (DPDF) produced when the PDF of $Al_{83}Y_7Fe_8Ti_2$ is subtracted from that of $Al_{85}Y_7Fe_8$. This figure highlights the changes in the local structure when 2% Ti replaces Al. The results show peaks and valleys where the PDFs of the two alloys are different and oscillate around zero where they are the same. The model in Figure 4-11 was obtained by determining the PDFs for body-centered Fe and for orthorhombic Al_6Fe, as described above, and calculating $G(r)^{Fe}$-$G(r)^{Al_6Fe}$. From the good agreement shown in Figure 4-11, the approximations of $Al_{85}Y_7Fe_8$ with Al, Fe, and Al_3Y clusters and $Al_{83}Y_7Fe_8Ti_2$ with by Al, Al_6Fe, and Al_3Y clusters seem, qualitatively, quite reasonable. The differences in the model and the data (i.e., the peaks in the model are sharper than in the measured data) are mainly due to a lack of long-range order in the measured data, where the model was calculated for crystalline materials. The qualitative agreement shown in Figure 4-11 further indicates that the choice of clusters shown in Figure 4-10 is reasonable.

4.2.3 Discussion on CSRO and Local Atomic Structure

Al and Al_3Y are the most stable phases according to the Al-Y binary phase diagram for the composition. Y has the largest negative heat of mixing with Al in the current alloy (ΔH_{mix} = -38kJ/mol, Table 4-1 [126]). This indicates that Y will easily bond

with Al, as observed for both $Al_{85}Y_7Fe_8$ and $Al_{83}Y_7Fe_8Ti_2$ by the presence of the Al_3Y-type clusters. The primary difference between the PDFs of the two alloys was that $Al_{83}Y_7Fe_8Ti_2$ was better modeled with Al_6Fe while Fe produced a better fit for $Al_{85}Y_7Fe_8$. The difference in the PDFs by changing the local structure from Fe to Al_6Fe was also visible from the DPDF, Fig. 11. This comparison suggests that the primary difference between the two phases is that, in the presence of Ti, Al_6Fe clusters tend to form instead of Fe resulting in an enhanced glass-forming ability as shown from the scattering results, Fig. 9. During the mechanical alloying of $Al_{83}Y_7Fe_8Ti_2$ it is likely that Al_6Fe and Al_3Y clusters are formed in addition to Al, and the continued milling caused a steady refinement of the crystal size and destroyed the long-range order leaving only the short-range clusters. Al_6Fe is a metastable phase, but is commonly present during polymorphous crystallization reactions [113, 147, 148] in Al-Fe systems. Al_6Fe can form during a deformation induced transformation of Al-Fe alloys as the defect concentration becomes high near the Al and Fe phase boundaries [149], which would be continuously occurring during the mechanical alloying process. The presence of Al_6Fe–type clustering has previously been ascribed to enabling the glass formation in Al-Y-Fe rapidly-solidified ribbons.

In order to understand the effect of Ti on the atomic interactions of Al and Fe it is necessary to consider its influence on the free energy of the system. Ti has a negative heat of mixing with Al and Fe (ΔH_{mix} = -30 and -17 kJ/mol, respectively), which means that it is energetically favorable for Ti to bond with Al and Fe. Ti will preferentially bond with Al over all other elements present because it has the largest negative heat of mixing. Subsequently, Al-type clusters containing Ti may have a greater driving force to

form bonds with Fe because heat of mixing of Ti and Fe is 55% higher than that of pure Al and Fe (the heat of mixing for Al-Fe is -11kJ/mol). Therefore, Ti could promote Al-Fe short range chemical ordering and result in the increases in the presence of Al_6Fe-type clusters in the $Al_{83}Y_7Fe_8Ti_2$ alloy.

Furthermore, Ti has a positive heat of mixing with Y (+15 kJ/mol), which means that it will be less favorable for Ti to bond with Y. While large negative heats of mixing between the constituent elements of metallic glasses has typically been attributed to enhanced glass forming ability, positive heats of mixing between elements added in minor amounts can cause chemical heterogeneity in the alloy. Recent reports have indicated that a positive heat of mixing with alloying elements can promote phase separation in the amorphous alloy. This phase separation can lead to the formation of a type of dual phase amorphous material that can have increased glass forming ability [150], increased thermal stability [151], or increased plasticity during mechanical testing [152-154]. The positive heat of mixing of Ti and Y could lead to heterogeneous regions in which one region is rich in Y, and another is rich in Fe and Ti. The heat of mixing between Fe and Y is small (-1 kJ/mol), so there is little driving force for Fe-Y bonding as well.

Finally, the structure factor data for both $Al_{85}Y_7Fe_8$ and $Al_{83}Y_7Fe_8Ti_2$ showed a prepeak centered at 1.40 and 1.45$Å^{-1}$, respectively. The prepeak in the structure factor data can be attributed to short-range ordering of unlike atoms [36]. The intensity of the prepeak of $Al_{83}Y_7Fe_8Ti_2$ was about 70% greater than that of $Al_{85}Y_7Fe_8$ which indicates that there is more short-range chemical ordering in the $Al_{83}Y_7Fe_8Ti_2$ alloy [155]. The prepeak in this system is almost purely from the solute, while the main part of the

structure factor is from the amorphous matrix. If we consider an Fe – Y system in an amorphous Al matrix, and if Fe and Y have a repulsive nature in this system as mentioned earlier. Fe and Y atoms can form their own dense random packing structure with there average correlation distance much larger than the average atomic radii due to dilution [105]. Ehrenfest [156] illustrated that scattering of amorphous materials can be approximated by applying the Debye equation:

$$I(q) = \sum_m \sum_n f_m f_n \frac{\sin qr_{mn}}{qr_{mn}} \tag{6}$$

where *I(q)* is the scattering intensity and *f* is the scattering factor for atoms *m* and *n*, to the case of a diatomic gas. Coherent scattering between molecules can be neglected, and if the atoms are identical, Eq. (3) becomes:

$$I(q) = 2f^2(1 + \frac{\sin qL}{qL}) \tag{7}$$

where *L* is the distance between the two atoms. The first q_{max} will occur at $1.23(2\pi) / L$. This gives the distance between the solute elements in the amorphous matrix and appears as a prepeak when chemical short-range ordering is present [36]. Hsieh found by gradually changing the composition of Al-Fe-RE alloys, that, in binary Al-RE and Al-Fe alloys prepeak at 1.23$Å^{-1}$ corresponds to Al-RE chemical short range ordering, and a prepeak at 1.58 $Å^{-1}$ corresponds to Al-Fe short range ordering [104]. In ternary alloys,

the prepeak locations are in between these two extremes depending on the alloy [104]. The addition of 2% Ti to the $Al_{85}Y_7Fe_8$ alloy caused the prepeak to move from 1.4 $Å^{-1}$ to 1.45$Å^{-1}$. This shift in prepeak position indicates that the ordering has changed from mostly of Al-Y (i.e., Al_3Y) clusters to include more Al-Fe clusters (i.e. Al_6Fe) in the alloy. The increased intensity of the prepeak also implies that the chemical short-range order has increased with the addition of Ti to the ternary alloy and cluster formation has been enhanced.

4.3 Evolution of Local Atomic Structure During Annealing Below T_x

Recent studies on the crystallization behavior using DSC and XRD revealed that the addition of 2% Ti to amorphous Al-Y-Fe systems also changed the crystallization from a primary crystallization of fcc-Al crystals to tetragonal Al_7Fe_5Y crystals presumably by forcing long-range diffusion of atoms to drive the crystallization process [32]. The local order plays an important role in the mechanical and thermal properties of these alloys and structural studies are necessary to better understand this behavior. However, short and medium-range order in amorphous materials is much less well understood than long range order in crystalline materials.

This section presents experimental investigation of the influence of the addition of a small amount of Ti on the changes in local atomic ordering in the amorphous state and its influence on the amorphous structure 'during heating' using a PDF analysis. The study focuses on examining the differences in the amorphous structure at the local atomic level when $Al_{85}Y_7Fe_8$ and $Al_{83}Y_7Fe_8Ti_2$ are heated to structurally relax and to crystallize using differential scanning calorimetry (DSC) and synchrotron x-ray diffraction (SXRD).

4.3.1 Calorimetry Study during the Heat Treatments below T_x

Differential scanning calorimetry (DSC) was performed at a heating rate of 20°C/min. to examine the crystallization behavior of $Al_{85}Y_7Fe_8$ and $Al_{83}Y_7Fe_8Ti_2$. The onset-of-crystallization temperature, T_x, was obtained from the results of the DSC scans, Figure 4-12. The primary crystallization of $Al_{85}Y_7Fe_8$ occurs at 354ºC, while replacing Al with 2% Ti delays the crystallization to 446ºC.

Furthermore, isothermal anneals were performed on both alloys for 10 minutes at 100, 60, 40, and 20°C below their respective crystallization temperatures observed in Figure 4-12. Figure 4-13 shows the results of the isothermal anneals for $Al_{85}Y_7Fe_8$. These DSC traces show that, after an instrument transient period (a sharp drop in the beginning), a continuously increasing (endothermic heat flow) DSC signal for each of the annealing temperatures, 255, 295, 315, and 335°C. Figure 4-14 shows the DSC traces at 350, 390, 410°C of the isothermal anneals for $Al_{83}Y_7Fe_8Ti_2$. The results show the DSC signal is continuously increasing, while annealing at 430°C shows a bell-shaped signal corresponding to the crystallization of the amorphous phase after a short incubation period.

4.3.2 Structure Factor after Heat Treatments

Figure 4-15 shows the structure factor data, collected using SXRD as explained in section 4.2.1 for $Al_{85}Y_7Fe_8$ in the as-milled condition and after heat treatments at 315 and 335°C. The as-milled data shows that the $Al_{85}Y_7Fe_8$ alloy consists of a nanocrystalline microstructure consistent with Al and Fe crystalline phases. These nanocrystalline phases remain stable until the alloy is heat treated at 335°C for 10 minutes. Figure 4-15 b

shows that as the alloy is heated from room temperature to 295°C; it appears that the Al Bragg-peaks are sharpening, likely due to grain growth.

Figure 4-16 shows the structure factor data for $Al_{83}Y_7Fe_8Ti_2$ in the as-milled condition and after heat treatment at 410° and 430°C. The as-milled data shows that the $Al_{83}Y_7Fe_8Ti_2$ alloy has an amorphous microstructure, and it remains amorphous until it was heat-treated at 430°C for 10 minutes. The results show that replacing 2% Al with Ti has affected the ability to form an amorphous phase, which is consistent with the studies previously observed, in which, the addition of Ti to Al-Fe-Y melt-spun ribbons caused the structure to change from a fine nanocrystalline material to an amorphous material [30, 144].

Closer examination of the structure factor data in Figures 4-15 and 4-16, again reveals small 'prepeaks' in the $Al_{85}Y_7Fe_8$ and $Al_{83}Y_7Fe_8Ti_2$ data centered at about 1.4 $Å^{-1}$ and 1.45$Å^{-1}$, which are characteristic of a cluster structure consisting of unlike atoms [145] as shown in section 4.2.1. It was mentioned earlier that the integrated area of the prepeak for $Al_{83}Y_7Fe_8Ti_2$ is about 70% larger than that of $Al_{85}Y_7Fe_8$. The prepeaks for both alloys increase in integrated peak intensity when they are annealed at 100°C below T_x indicating that there is an increase in the chemical short range order in the alloys as they are heated. The intensity remains almost constant as it is annealed to higher temperatures, and then there is a sharp decrease in intensity when the alloys are annealed 20°C below T_x, as shown in Figure 4-17. The increased area under the prepeak indicates the order of the structure corresponding to the pre-peak has increased. This would mean that the local structure becomes more ordered during structural relaxation. When the

alloy begins to crystallize at 20°C below T_x, the chemical short range ordering decreases sharply, as seen in the decrease in area under the prepeak.

4.3.3 Local Atomic Structure after Heat Treatments

The pair distribution function (PDF) analysis results of the two as-milled alloys are shown again in Figure 4-18. Figure 4-19 shows the PDF of $Al_{85}Y_7Fe_8$ in the as-milled and annealed condition along with the DPDF's at various temperatures. After annealing $Al_{85}Y_7Fe_8$ at 255°C for 10 minutes, the first coordination shell of the PDF shows that there is an increase in intensity at a distance of 2.86Å and a decrease in intensity at 2.5Å, Figure 4-19a. The increase at 2.86 Å likely corresponds to an increase in the number Al-Al pairs, since the radius of Al is 1.43Å [157]. The decrease in intensity at 2.5Å likely corresponds to a decrease in Fe-Fe bonding, since the radius of Fe is 1.26Å [157]. Both Al and Fe were seen in the diffraction patterns. By examining the successive difference curves for the different heat treatments we can observe the evolution of the local structure during heating before crystallization and gain insights into the nature of structural relaxation. The difference pair distribution function (DPDF) for the sample annealed at 255°C and the as-milled sample, DPDF (255°C - room temperature) is shown in Figure 4-19b. The DPDF highlights the changes in the local atomic structure during annealing below T_x. The negative peak at 2.5Å is due to the decrease in Fe-Fe bonding, and the positive peak at 2.86 Å is due to an increase in Al-Al bonding. Figure 4-19c shows the changes as the annealing temperature is raised from 255°C to 315°C. The peaks and troughs in the data are at the same locations, but with lower intensities. The DPDF (315°C – 255°C) shows (not shown here) that small

changes continue to occur. The DPDF for the anneal at 335°C minus 315°C is shown in Figure 4-19d, note the change in scale. When the temperature is increased to 335°C and annealed for 10 minutes, a phase transition occurs and the alloy crystallizes into fcc-Al and a bct-Al_7Fe_5Y-type phase, as will be shown in section 4.4.

The PDFs of $Al_{83}Y_7Fe_8Ti_2$ for the as-milled condition and the alloy annealed at 350°C, Figure 4-20a, show that the first shell has sharpened by decreasing the density of short and long-range atomic interactions and increased the density of bonds in the 2.65 to 3.2 Å range. The difference curve DPDF (350°C – room temperature), Figure 4-20b, shows the sharpening observed in the G(r) data as the negative values of the difference curve at the edges of the first coordination shell and the positive values in the middle of the coordination shell. This increase in atomic pair density around 2.8-3.1 angstroms indicates that there is an increase in the interactions of Al-Al and Al-Y atomic pairs. There is a decrease at ~2.45 angstroms indicating that the Fe-Fe-like bonding has decreased while there is a significant increase in the range of 2.6-2.7 angstroms that indicate that Fe-Al clusters are forming. The difference curve of 410°C -390°C, Figure 4-20c, does not show that any significant changes have occurred with this intermediate temperature change. The difference curve for 430°C – 410°C, Figure 4-20d, shows large differences that are related to partial crystallization of the amorphous phase as observed in the DSC data. Just like the diffraction data shows that the sample annealed at 430°C has crystallized, the difference curve of 430°C – room temperature can be fit with a model of a tetragonal Al_7Fe_5Y-type phase, which is the intermetallic phase formed during the first crystallization event.

4.3.4 Structure and Stability of Heat Treated $Al_{85}Y_7Fe_8$ and $Al_{83}Y_7Fe_8Ti_2$

The isothermal anneal performed at 430°C showed $Al_{83}Y_7Fe_8Ti_2$ crystallized with a bell-shaped curves which are a signal typical for a nucleation and growth reaction where the heat released is due to the difference in enthalpy between the amorphous and crystalline phases [31]. Diffraction results show that this temperature is the first annealing temperature where crystalline phases appear. This indicates that the as-milled powder consists of an amorphous phase rather than a fine nanocrystalline phase. The isothermal DSC scan at 335°C performed on $Al_{85}Y_7Fe_8$ shows only a monotonically increasing signal. Diffraction results showed that after annealing at this temperature, new crystalline peaks appear indicating a phase change from the as-milled alloy. This monotonically increasing signal is characteristic of a grain corsening reaction taking place during the annealing. These isothermal DSC results are consistent with previous results showing the addition of Ti to Al-Y-Fe alloys results in a change in the crystallization mechanism from a coarsening reaction to a nucleation and growth reaction for Al-Y-Fe-Ti alloys [30].

The effect of adding 2% Ti to $Al_{85}Y_7Fe_8$ on the formation of an amorphous phase and the thermal stability of the resulting alloy is clear. $Al_{83}Y_7Fe_8Ti_2$ forms an amorphous phase after 45 hours of ball-milling, while $Al_{85}Y_7Fe_8$ forms a nanocrystalline microstructure, and the crystallization event observed during continuous heating differential scanning calorimetry was delayed by 92°C. The improvement in thermal stability may be due to this stronger chemical short range ordering [143]. The 70% increase in area of the prepeak of $Al_{83}Y_7Fe_8Ti_2$ indicates that this CSRO increases as temperature increases. The CSRO would make a diffusion controlled crystallization

proceeding through a nucleation and growth process more difficult at lower temperatures, and higher temperatures would be necessary for crystallization.

Analysis of the changes in the pair distribution function as a function of annealing temperature gives additional information about how the local atomic order changes at higher temperatures. Figure 4-20a shows that when the $Al_{83}Y_7Fe_8Ti_2$ alloys is annealed at 350°C, about 100°C below the crystallization temperature, the first coordination shell of the PDF sharpens (i.e. becomes narrower and taller). Sharpening of the first coordination shell after annealing is a characteristic of structural relaxation of a metallic glass [89]. This corresponds to the elimination of short and long inter-atomic distances, while the number of atom pairs with bonds of average distance is increased [38]. This is fundamentally different from annealing out free volume because free volume would only correspond to the long inter-atomic distances (the right shoulder of the first coordination shell in the PDF). Rather, the observed changes may be due to relaxation of tensile and compressive atomic level stresses [92]. During structural relaxation the local atomic configuration changes to lower the free energy of the amorphous phase. These changes result in short-range atomic reordering and have been attributed to viscous flow in the amorphous phase of interlocking flow units or clusters, rather than through a long-range diffusion process [158, 159]. Structural relaxation does not result in the formation of a new phase, but the changes in chemical ordering during relaxation may lead to phase separation. The DPDF shows annealing at 350° causes an increase in atom pairs in the range of 2.6 to 3.2 Å. This coincides with the range where an increase in chemical clustering would occur. An increase in Al-Fe bonds would be at 2.67 Å, Al-Al pairs would be at 2.86, and Al-Y bonds would be at 3.2 Å. These results imply that the

promotion of clusters due to the addition of Ti increases as temperature is increased and this CSRO leads to a delay in crystallization by retarding diffusion in the alloy. In particular, there is a distinct increase in the 'Al-Fe' bonds, which were not observed in the ternary Al-Y-Fe alloy.

While annealing at temperatures below T_x caused $Al_{83}Y_7Fe_8Ti_2$ to changes the amorphous phase to a more relaxed state closer to equilibrium, a fundamentally different process occurs in the ternary alloy without the 2% Ti addition. The diffraction patterns in Figure 4-15b reveal that the Bragg peaks of the nanocrystalline fcc-Al phase sharpen during the heat treatment of $Al_{85}Y_7Fe_8$. This sharpening of the Al diffraction peaks signify that grain coarsening is occurring at temperatures below the T_x observed in the DSC. The decrease in intensity of the bcc-Fe peaks indicates that the Fe atoms in the alloy are diffusing into the alloy. This is also seen in the real-space analysis of the PDF in Figure 4-19b. The Fe-Fe pairs at 2.5Å are decreasing in intensity as the alloy is annealed, and the Al-Al pairs increase in intensity. The DPDF of $Al_{85}Y_7Fe_8$ differs from that of $Al_{83}Y_7Fe_8Ti_2$ in that the there is no sharpening of the first coordination shell with negative values at both extreme bond lengths and positive values for the average bond lengths. The DPDF of $Al_{85}Y_7Fe_8$ along with the diffraction data do not indicate a structural relaxation process occurring at intermediate temperatures in the amorphous $Al_{83}Y_7Fe_8Ti_2$, but rather exhibit a continual grain coarsening process.

4.4 Crystallization Behavior of Amorphous Al

The study on the crystallization behavior of amorphous alloys is of fundamental importance for the understanding of the glass-forming ability of these alloys [52, 160-

163]. It has been observed that aluminum alloys often devitrify through a nanocrystallization process [23]. During this crystallization process, a high density (> 10^{22} m^{-3}) of face-centered cubic (fcc) Al nanocrystals may form, but their growth reaction may be limited due to overlapping of diffusion fields of the growing grains [11]. The formation of such nanocrystals may be linked to "quenched-in" nuclei, which have a short-range fcc-like structure consisting of Al atoms. Therefore, during the crystallization process, only short-range rearrangements seem to be necessary to form the nuclei into nanocrystals [24].

This section focuses on examining the crystallization behavior of microalloyed aluminum-based amorphous alloys with a high thermal stability. The crystallization process was examined using differential scanning calorimetry (DSC) and *in-situ* high-temperature synchrotron x-ray diffraction to determine the microstructural evolution during heating of the amorphous alloys. The results show different crystallization processes operating for $Al_{85}Y_7Fe_8$ and the microalloyed $Al_{83}Y_7Fe_8Ti_2$ and $Al_{79}Y_7Fe_8Ni_3Ti_2Nd_1$.

4.4.1 Crystallization Behavior Determined by Calorimetry

Differential scanning calorimetry (DSC) was performed to examine the crystallization behavior of the ball-milled powders. The onset-of-crystallization temperature, T_x, was obtained from the results of the DSC scans, Figure 4-21. The primary crystallization of $Al_{85}Y_7Fe_8$ occurs at 342ºC, while the addition of 2% Ti delays the crystallization to 446ºC. $Al_{79}Y_7Fe_8Ni_3Ti_2Nd_1$ is even more thermally stable, with the primary crystallization occurring at 457ºC. The melting temperatures of $Al_{85}Y_7Fe_8$,

$Al_{83}Y_7Fe_8Ti_2$, and $Al_{79}Y_7Fe_8Ni_3Ti_2Nd_1$ were measured to be 642, 644, and 642°C, respectively.

4.4.2 *In-situ* High-Temperature X-ray Diffraction

In order to examine the phase evolution during the crystallization process, *in-situ* synchrotron x-ray diffraction (SXRD) was performed during heating of the as-milled powders. Synchrotron x-ray diffraction, Figure 4-22, showed the presence of an Fe phase (marked with an arrow below the peaks in Figs. 22 (a), (b), and (c)) in all of the as-milled alloys, likely due to the ball-milling process, which was not detectable using laboratory x-ray diffraction. SXRD patterns were collected at 100°C intervals up to 300°C and at 25°C intervals until the temperature reached 500°C. SXRD results show that the amorphous phase of the $Al_{85}Y_7Fe_8$ powder remains stable as the powder is heated to 300ºC, Fig. 22a. $Al_{85}Y_7Fe_8$ began to crystallize after the powder was heated to 325ºC under the current heating conditions. Fcc-Al and body-centered tetragonal (bct)-type intermetallic phase (Al_7Fe_5Y) with the I/4mmm space group appear at this temperature. The heating rates during the *in-situ* diffraction experiment were different than those used in the DSC mainly due to the holding time for the diffraction measurements. However, the heating schemes (e.g. measurement temperatures, heating rates, hold times, etc) were kept consistent for each sample measured by SXRD. As a result, the absolute temperatures where the crystallization occur during SXRD are different from those measured using the DSC. However, the qualitative trends remain consistent and agree well with the DSC results, which will be shown in the following section.

4.4.3 Evolution of Crystalline Products

When Al is replaced by 2% Ti, the DSC results showed that the crystallization is delayed by 58ºC, and the same trend was observed in the *in-situ* SXRD result, Figure 4-22b. The amorphous phase remains stable until the powder is heated to 375ºC, where small amounts of bct phase (Al_7Fe_5Y) begin to precipitate, which was not observed in the DSC data. The increase in the T_x observed during SXRD is about 50°C greater than $Al_{85}Y_7Fe_8$. More interestingly, the crystallization process is qualitatively different from the ternary $Al_{85}Y_7Fe_8$ alloy in that no significant amount of fcc-Al precipitates. The microstructure remains as a mixture of amorphous phase and bct phase (Al_7Fe_5Y) until the temperature is increased to 450ºC, where the $Al_{83}Y_7Fe_8Ti_2$ amorphous phase fully crystallizes, mostly into the bct phase (Al_7Fe_5Y) with little or no fcc-Al phase. Figure 4-22c shows that the addition of 3% Ni and 1% Nd (both replacing Al) to $Al_{83}Y_7Fe_8Ti_2$ increases the onset of crystallization temperature even further, which is consistent with the DSC data. The first crystallization event observed for $Al_{79}Y_7Fe_8Ni_3Ti_2Nd_1$ is after the powder is heated to 425ºC. At this temperature, the bct phase (Al_7Fe_5Y) begins to precipitate from the amorphous matrix. Further heating to 450ºC induced complete crystallization of the amorphous matrix, and the presence of a small amount of Al_3Ni was also observed.

In this study, *in-situ* SXRD results showed that the crystallization behavior of the microalloyed $Al_{83}Y_7Fe_8Ti_2$ and $Al_{79}Y_7Fe_8Ni_3Ti_2Nd_1$ is qualitatively different from the ternary $Al_{85}Y_7Fe_8$ and other previously reported amorphous Al alloys [11, 24, 139, 164] in that they crystallize at much higher temperatures, and the primary crystallization products are intermetallic phases (Al_7Fe_5Y and Al_3Ni) rather than fcc-Al. For amorphous

alloys with very high (> 80%) Al content, the local order typically consists of nanoclusters, which are mostly aluminum [67, 105, 165]. Because the Al is already clustered in a configuration close to the stable fcc phase, the energy required to form the fcc-Al phase is relatively low. The crystallization of amorphous aluminum alloys into fcc-Al does not require long-range diffusion because short-range atomic redistribution is sufficient for the precipitation of Al nanocrystals [24]. When the Al content is reduced by 2~6% and microalloying elements of Ti, Ni, and Nd, are present, the local ordering is changed and long-range diffusion may become necessary for the crystallization. Ti has shown to decrease the aluminum diffusion rate by increasing the local ordering with the other elements in the alloy. This change in the local order has been shown to inhibit the nucleation of the fcc-Al phase [30]. Ti and Nd both can scavenge for oxygen atoms, which have been shown to be detrimental to glass formation [166], and form nano-sized oxide particles or clusters. However, these oxide clusters do not trigger the formation of large crystalline phases around them because they change the interfacial structures and chemical composition around them [27]. It is relatively more difficult for Al atoms to simply re-order, and the sluggish diffusion of larger atoms, such as Y, Nd, and Ti, require more energy for the amorphous phase to crystallize. In order for crystallization to proceed through long-range diffusion, rather than short-range rearrangements, the alloy must be heated to higher temperatures, and is therefore more thermally stable. Ni additions caused the appearance of the Al_3Ni in the crystallization products. Competition between the Al_7Fe_5Y and Al_3Ni crystalline phases may also serve to further shift the onset of crystallization to higher temperatures.

4.5 Consolidation of Aluminum Powder

In an attempt to consolidate the mechanically alloyed amorphous aluminum alloy powder, quais-isostatic forging, also known as the Ceracon process was used. Ceracon process was conceived in the late 1960s for metal powder consolidation. Ceracon stands for CERAmic CONsolidation.

The process uses a pseudo-isostatic, hot forging, where green compacts with densities about 70 – 80 % of the theoretical density are used as the preform. The preform is heated to the consolidating temperature, and so is the pressure transmitting medium (PTM). The preform is embedded in the PTM and they are put into an empty die in a hydraulic press, where sufficient pressure is applied to densify the preform. The process is especially useful for consolidation of materials that cannot sustain exposure to elevated temperature for prolonged amounts of time, such as alloys that will change chemically or microstucturally after prolonged heating [167]. Ceracon processing is also useful because of shearing forces present in the consolidation process that break-up oxide layers that can adversely affect interparticle bonding. Due to the metastable nature of the amorphous aluminum phase, the Ceracon process seems to be the most appropriate approach to consolidate the powder. Table 4-4 summarizes the samples used in this consolidation study.

4.5.1 Optical Observations

Figure 4-23 shows photographs of the samples after they have been forged. From this figure it can be seen that the samples have been deformed and that some samples are heavily shear banded. All 3 of the samples forged at 420°C show shear banding. The

100% mechanically alloyed (MA) powder sample has been fractured into 6 pieces. The composite of 85% MA and 15% coarse grain (CG) aluminum sample shows shear bands completely traversing the sample, but the sample remains in one piece. The composite of 70%MA and 30%CG sample has shear bands around the edges, but the shear bands were stopped in the middle of the sample.

The samples forged at 445°C show less shear banding than those forged at 420°C. The 100% MA sample forged at 445°C shows a few shear band that have traversed the sample while most have stopped in the middle. The 70% MA and 30% CG composite forged at 445°C shows very few shear bands and appears mostly undeformed.

4.5.2 X-ray Diffraction of Consolidated Samples

Figure 4-24 shows the x-ray diffraction patterns for each of the forged samples. Figure 4-24a show the 100%MA sample forged at 420°C. Figures 4-24b and 4-24c show the fcc Al phase due to the CG additions and the bct Al_7Fe_5Y phase. The 100% MA and 70% MA plus 30% CG samples forged at 445°C are shown in Figures 4-24d and 4-24e. These figures show the same crystalline plus amorphous phases as the samples forged at 420°C. These results show that the original amorphous phase in all of the samples partially crystallized with some amorphous phase remaining after forging.

4.5.3 Mechanical Behavior of Consolidated Samples

In order to examine the mechanical behavior of the consolidated samples, monotonic compression tests were performed. Tests were performed at an initial strain rate of 10^{-4}/sec. The results of the compression tests are shown in Figure 4-25 and 4-26.

The 100% MA sample forged at 420°C was very brittle, and fractured shortly after loading began. The 85% MA and 15% CG sample forged at 420°C yielded and fractured at 265 MPa. The 70% MA and 30% CG sample forged at 420°C yielded at about 300 MPa. This sample did not fail completely at this stress. The sample started fracturing at about 300 MPa, but the ductile CG Al phase held the sample together. This sample did not completely fail during the test, but did show multiple yield points. Figure 4-26 shows the compression tests of the samples forged at 445°C. The 100% MA sample forged at 445°C failed at about 350 MPa. The 70% MA and 30% CG sample forged at 445°C behaves similar to the sample of the same composition forged at 420°C. The sample yields at 285 MPa where the brittle phase fractured, but the sample did not completely fail because the ductile Al phase held the sample together and allowed continued loading. The strengths of these consolidated sample were all 2-3 times lower than expected. A possible explanation for these low strengths is that significant bonding did not occur during the consolidation. Porosity in these samples and poor bonding likely resulted in the brittle behavior and low strengths in the 100%MA samples. Bonding was improved in the composite samples, but poor consolidation in the MA phase likely still contributed to the low strengths.

4.6 *In-situ* Neutron Scattering of a Zr-based Bulk Metallic Glass during Mechanical Loading

Metallic glasses are an important new class of engineering materials with attractive properties such as high strength, high hardness, a large elastic strain limit (~2%), and good fracture toughness [3, 58, 168, 169]. Because of their amorphous structure and

inherent lack of grains, metallic glasses do not deform due to dislocation motion like most crystalline materials. They deform via localized shear bands which quickly propagate through the materials, quickly leading to catastrophic failure [170]. Because metallic glasses form these localized shear bands, typically leading to failure before appreciable plastic deformation can occur, understanding of the internal strains during elastic deformation is an important aspect of understanding the deformation in these material. Modeling of the deformation of BMGs began about 35 years ago [171-173], but these models have not been verified by experiments because experimental techniques for measuring the internal stress-strain behavior of glasses were not available. Today high-intensity synchrotron x-ray and pulsed neutron diffraction facilities make *in-situ* loading diffraction experiments possible. An understanding of the deformation behavior at all length scales, nanoscale, microscopic, and macroscopic, is still required for these materials, and considerable effort is being put forth to understand the deformation and fracture of metallic glasses [174-177]. Since most of the deformation is elastic, and because of the high elastic deformation limit of BMGs they should be a good candidate for strain measurements via diffraction. The primary challenge to studying the deformation of metallic glasses by diffraction is that metallic glasses are not crystalline. They do not produce sharp crystalline peaks, whose changes can be easily and accurately measured. The diffraction pattern of metallic glasses consists of a broad hump, which has typically been considered useless for accurate strain measurements.

X-ray and neutron diffraction have been used to measure elastic strains in crystalline engineering materials for a long time. This is done by measuring changes in the d-spacing of atomic planes, and the microscopic diffraction data can be accurately

correlated to macroscopic properties. Recently, efforts have been made to use high-energy x-rays as a tool to measure elastic strains in amorphous materials [39, 40]. Because high-energy x-rays and neutrons can be used to examine the local atomic structure of materials, these techniques have been employed to examine structural changes of glasses that have been subjected to large stresses. This section presents efforts to examine the deformation of $Zr_{57}Nb_5Cu_{15.4}Ni_{12.6}Al_{10}$ by using neutron diffraction.

4.6.1 Measurement of Strain from PDF Analysis

Analysis of glasses using the PDF assumes that the BMGs are isotropic and amorphous materials are usually assumed to be isotropic. In this case the assumption is made that the small amount of anisotropy caused the uniaxial deformation can be neglected even though a thorough analysis would involve using spherical harmonics to describe the small amount of anisotropy [178, 179] The pair distribution functions, *G(r)*, shown in Figure 4-27a, for the axial direction have been obtained through the Fourier transformation of the structure factor, *S(q)*, data. The first coordination shell of *G(r)* shows that the peak shifts to smaller r with increasing compressive load, indicating that the atom-atom pair distances are being shortened or compressed, Figure 4-27b. When the stress was lowered from 1,500 MPa to the unloaded condition of 20 MPa, all of the strain was recovered to a level below the initial loading condition of 20 MPa. In order to calculate the shift in position of *G(r)*, the location where $G(r) = 0$ was used as the reference point for internal strain measurements [40].

4.6.2 Local Atomic Response to Applied Stress

The strains determined from *G(r)* from the axial bank of the SMARTS instrument are plotted as a function of distance r out to ~16 Å for the different stress levels, Figure 4-28. Distances greater than 16 Å approach zero indicating that there is no order past 16 Å. There appears to be no significant trend for increasing strain as the distance in the PDF increases. This is significantly different than was reported by Paulsen [39], in which it was reported that strain increased by a factor of 2.7 beyond the first coordination shell. The data shows that at a distance of about 9-10 Å and 15-16 Å there are spikes in the strain data which are seen for each level of applied stress. Similar spikes in strain were reported on a similar metallic glass (Vit105 – $Zr_{57}Ti_5Cu_{20}Ni_8Al_{10}$) at distances of 8-9 Å and 13-15 Å.

The average strain was determined by taking an average of all strains for each stress over the complete range of *r* measured. This linear fit yields an elastic modulus value E = 121 GPa, Figure 4-29. The elastic modulus of $Zr_{57}Nb_5Cu_{15.4}Ni_{12.6}Al_{10}$ reported in the literature is 87.3GPa [180], a 39% difference. By calculating the slope from the transverse direction data the Poisson's ratio, *v*, was calculated to be 0.52. The literature value for $v = 0.365$, a difference of ~42%.

Statistical methods were also used to measure the local deformation of the BMG. The center of mass of each peak in the PDF was calculated according to the equation:

$$COM = \frac{\oint rG(r)dr}{\oint G(r)dr} \tag{8}$$

This measures how each of the coordination shells move for each of the applied stress levels. This gives an average to how the bulk of the atoms in each coordination shell are moving with stress. It is less sensitive to termination ripples the PDF data that could affect the stress strain behavior calculated using the intercept method because it is a weighted average and is less responsive to the data farther from the center of mass of each coordination shell. The center of mass data was plotted to give strain as a function of distance *r*, Figure 4-28b. The data shows that as stress is applied, the strain increases in a very similar manner observed in the intercept method. When the stress is lowered back to 20 MPa, the strain decreases to a level near the initial condition of 20 MPa, as expected for a fully recoverable deformation process. The average strain from all of the coordination shells results in an obtained modulus value of about 112 GPa, which within the error bars calculated for the intercept method, as seen in Figure 4-29. The difference between the literature data and the center-of-mass determination of Young's modulus and Poisson's ratio is 29% and 32%, respectively.

4.6.3 Proposed Deformation Mechanisms

It was noted previously that the first coordination shell of BMGs is stiffer than the bulk average of the material taken at large value of *r*. This appears to be the case for the $Zr_{57}Nb_5Cu_{15.4}Ni_{12.6}Al_{10}$ alloy as well. The elastic modulus of the first $G(r) = 0$ intercept (corresponding to the first coordination shell) was measured to be 145GPa, while the second intercept and the bulk (everything outside of the 1st shell) give values of 97 GPa and 107 GPa, respectively. The values of the elastic moduli in the glass in the first shell likely are due to overlapping Zr - (Cu, Ni) and (Cu, Ni) – (Cu, Ni) bonds and Zr – Zr

bonds, as these values are similar to these crystalline materials. The left side of the first coordination shell had a stiffness of 145 GPa, while the right side had a stiffness of 97GPa. The elastic modulus of crystalline Zr is 96 GPa, Cu is 115 GPa, and Ni is 204 GPa [181]. Based on atomic size calculations, the left side of the first coordination shell is dominantly Zr-Zr bonds, while the right side is dominated by Zr-(Ni, Cu) and (Ni, Cu) – (Ni, Cu) bonds. The presence of Al and Nb, in the diffraction data, is difficult to observe in the diffraction data due to the low scattering cross section of Al and the low concentration of Nb in the alloy. This could be important when comparing the diffraction data to the macroscopic data because at 10% and 5%, the concentration of these elements is likely higher than can be neglected on the macroscopic scale.

The difference between the measured local elastic modulus of ~112 GPa and the literature value of ~87 GPa is about 29%. This difference is about the same as the difference between glasses and their corresponding crystalline counterparts [182, 183]. This difference in modulus is likely due to internal displacements or rearrangements which can occur in glasses but cannot in crystals [171, 172]. In crystals, atoms are located at centers of symmetry, and the atomic displacements are completely described by the macroscopic displacement field. Glasses can have additional displacement options due to the regions of lower density caused by their amorphous nature, and some atoms will be strained more than others. The free volume present in metallic glasses allows atoms to move in a uniform direction with the applied stress and in a non-uniform direction with applied stress, and thus anelastic deformation can occur in glasses in addition to elastic deformation. These inhomogeneous displacements cause the decreases in the shear modulus and Young's modulus in glasses [184]. The diffraction results

would show the component of the strain in which the atoms moved in the same direction. The additional motion component of the strain in which the atoms are displaced in different directions would not appear in the analysis of the diffraction data. This effect can be removed to some degree by structurally relaxing the glass. The slight densification associated with structural relaxation has been shown to substantially raise the Young's modulus closer to that of the devitrified state [185].

If atoms in metallic glasses have short range order, and solute atoms tend to cluster around solvent atoms [68, 142, 186], this effect would be seen by the movement of clusters as opposed to individual atoms. The shear displacement of clusters would not be observed in the local structure because average local environment would be the same. In this way the atoms could move in a uniform manner under the applied stress that would be measured by diffraction, and at the same time the clusters themselves could rotate and arrange themselves in a way to minimize internal energy [141]. Rotation would be allowed by the additional volume frozen into the glass, and a collective rotation of clusters could serve to initiate shear bands, which appear at higher stresses near the yield stress. The space between clusters, acting as free volume, would provide room for the rotation of clusters upon applied loading, helping to govern the deformation characteristics of the glass [187].

In order to investigate this phenomenon, the changes in the peak width were examined by studying the variance of each coordination shell in the PDF. The variance of the data from the center of mass is plotted in Figure 4-30. While the center of mass measurements show how the weighted center of the peaks move as a stress is applied, the variance of the data, which is a measure of how the data is distributed about the center of

mass, illustrates how the extremes of the data change with regard to the center of mass. Figure 4-6 indicates that in the fourth shell, r ~ 10 Å, the extremes move significantly more than the center of mass for each applied load. After this spike in the data, the variance appears to move in the negative direction to a spike at around 15 Å. These spikes are due to the coordination shell broadening and contracting at different distances as the stress is applied. This means that the environment at distances of about 10 Å from an average atom is being deformed more than atoms at smaller average distances. These spikes are present at all levels of stress, and the unloaded sample shows that this deformation in the broadening and contracting of the coordination shells is recoverable.

While the average strain is less than the macroscopic response, there are instances where the local strain exceeds the macroscopic behavior. While looking at the data obtained from the intercept method, this happens at distances of 9-10 Å and 15-16Å. A similar spike in the data was observed at ~10 Å when the variance from the center of mass was plotted as a function of distance, and this spike disappears upon unloading. Interestingly these spikes in strain correspond nicely to the diameter expected for shear transformation zones (STZ), ~10 Å, or roughly 3 or 4 atoms in diameter [173, 188, 189]. 3 or 4 atoms in diameter could then correspond to the size of one local cluster of atoms arranged with short range ordering schemes. The STZ is a deformation mechanism caused by the collective motion of atoms (possibly the atoms within a cluster rotating together) subjected to shearing forces. Multiple STZ's acting together can be thought of as a shear band nucleus. The STZ is a way for local shear events to comprise local plasticity. These local plastic strains could explain why the average strain measured is less than the macroscopic response of the material as plastic deformation would not be

detected via diffraction measurements. The rotation of clusters could explain the anelastic deformation behavior observed in this experiment along with the spikes in the strain data occurring at distances of about 10 Å.

Chapter V: Conclusions

Previous research results in the literature illustrated that amorphous aluminum alloys have great potential for structural applications due to their exceptional mechanical properties [1, 4, 190]. In addition to the technical utility of these alloys, there is also a fundamental interest in examining the glass-forming ability and unique crystallization behavior of these alloys. The current dissertation research has served to further the knowledge base on these alloys in multiple ways by addressing key scientific objectives. This dissertation presented a methodology developed for the production of amorphous aluminum powder through mechanical alloying. A better understanding of the relationship between the local atomic structure and the glass-forming ability has been established. The crystallization process has been evaluated at a local atomic level, and a potential consolidation method has been explored.

Because aluminum alloys are only marginal glass formers and have a very high critical cooling rate [5], a mechanical alloying technique was developed to produce amorphous aluminum alloy powders. The role that composition plays in the glass formability and crystallization in the system of $Al_{85}Y_7Fe_5TM_3$ (TM = Ni, Co, Cu, and Fe) was investigated. When one TM component is substituted with another TM component of similar atomic size, the intensity of the crystalline peaks in the XRD patterns changed as the enthalpy of mixing, ΔH_{mix}, for Al and TM changed. The general trend was observed that the alloys with the highest eutectic temperature of the binary alloy (Al–TM) also had the highest onset of crystallization temperature. Additions of Ti were also examined to determine the effect of Ti on the glass-forming ability of these alloys. The

alloy $Al_{83}Y_7Fe_8Ti_2$ appeared amorphous through diffraction experiments, and had the best glass-forming ability of all of the compositions examined.

In order to understand the relationship between the local atomic structure and the improved glass-forming alloy, $Al_{83}Y_7Fe_8Ti_2$, and a reference alloy, $Al_{85}Y_7Fe_8$, were examined by high-energy synchrotron x-ray diffraction. Diffraction results showed that $Al_{85}Y_7Fe_8$ structure to be nanocrystalline, while $Al_{83}Y_7Fe_8Ti_2$ is amorphous. The pair distribution function analyses revealed that local structure of $Al_{85}Y_7Fe_8$ was dominated by Al, Fe, and Al_3Y short range ordered regions. On the other hand, the local structure of $Al_{83}Y_7Fe_8Ti_2$ was comprised of Al, Al_6Fe, and Al_3Y short-range order regions, in which the order extended for about 8 angstroms. The addition of Ti seems to promote the Al-Fe interaction in a way that Al_6Fe clusters to form and enhance chemical ordering for the improved glass-forming ability.

Differential scanning calorimetry (DSC) results showed that the addition of Ti also improved the thermal stability by delaying crystallization by 92°C. Isothermal DSC showed that a monotonically decreasing signal for $Al_{85}Y_7Fe_8$ indicative of a grain coarsening process, but isothermal DSC of $Al_{83}Y_7Fe_8Ti_2$ showed a bell-shaped signal characteristic of a nucleation and growth during the crystallization event. Annealing of these alloys revealed structural relaxation occurring, due to the Ti addition, by increasing the chemical short range order (CSRO) in the amorphous phase. This short-range order in the amorphous phase is different from that of the stable crystalline phase, and this enhanced CSRO in the amorphous phase makes diffusion more difficult and delays crystallization to higher temperatures. The crystallization of $Al_{83}Y_7Fe_8Ti_2$ corresponds to the devitrification of the amorphous phase mainly into a bct-type intermetallic phase

(Al_7Fe_5Y) unlike $Al_{85}Y_7Fe_8$ and other aluminum-rich amorphous alloys reported previously, where the primary crystallization results in the precipitation of an fcc-Al phase.

Mechanically alloyed amorphous aluminum-based alloys were consolidated using the Ceracon forging process at two temperatures, 420°C and 445°C. The forged samples showed various levels of deformation after consolidation. X-ray diffraction showed that the amorphous phase of all of the samples had started to crystallize. The compression tests showed that the strengths of these consolidated alloys was low, likely due to poor bonding and porosity after the consolidation.

In addition to amorphous aluminum alloys, the mechanical behavior of a Zr-based bulk metallic glass was also examined in this work. The internal strain was measured for a $Zr_{57}Nb_5Cu_{15.4}Ni_{12.6}Al_{10}$ BMG *in-situ* by neutron diffraction. Measurements of the stress-strain behavior were examined by multiple data analysis methods in real space with good precision. The results show that local strains can be measured with good agreement with macroscopic data, and the differences in the local environment measured by diffraction are likely due to anelastic relaxations which occur in glasses but not in crystals. These results seem to validate the idea that metallic glasses contain short range order, and metallic glasses deformation occurs at length scales greater than this short range order.

Chapter VI: Future Research and Interests

This is fascinating time for the study of amorphous metallic alloys. Research is moving forward at an exciting pace around the world. Current topics of research on bulk metallic glasses being conducted on their thermodynamics and kinetics, glass formation of composites, atomistic modeling, increasing plastic deformation, and porous and foam materials.

As indicated in this research, the local atomic structure of amorphous metallic alloys plays a very important role in properties and glass-forming abilities of these materials. Small changes in chemical composition can have significant influences on the local atomic structure. Synchrotron x-ray and pulsed neutron sources can be used to couple experimental data to mathematical models of the atomic structure. Understanding this structure can guide the development of improved glass forming alloys, which is crucial for the development of improved metallic glasses.

One of the strongest driving forces behind the research into aluminum-based metallic glasses is their potential application as structural materials due to their unique high strength, low density, and high elastic limit. However, their poor glass forming ability provides the greatest hurdle for their use as engineering materials. The advance of bulk scale materials is essential for progression of this field. Current rapid solidification techniques only produce alloys with thicknesses on the tens of micrometer length-scale. Recent research has illustrated that amorphous aluminum can be produced through deformation techniques, such as powder metallurgy. With the development of good glass-forming alloys with high thermal stability, the use of these techniques may

enable the production of bulk alloys. The development of improved composite materials also appears to be a promising research approach for amorphous aluminum alloys.

References

1. He, Y., Poon, S., and Shiftlet, G., Science, 1988. 241: p. 1640.

2. He, Y., Dougherty, G., Shiftlet, G., and Poon, S., Acta Metall. Mater., 1993. 41(337).

3. Johnson, W., JOM, 2002. 54: p. 40-43.

4. Kawamura, Y., Mano, H., and Inoue, A., Scripta Materialia, 2001. 44(1599-1604).

5. Inoue, A., Progress in Materials Science, 1998. 43: p. 365-520.

6. Perepezko, J. and Herbert, R., JOM, 2002. 54: p. 34.

7. Inoue, A., Materials Transactions, JIM, 1994. 35: p. 485.

8. Poon, S., Shiflet, G., Guo, F., and Ponnambalam, V., Journal of Non-Crystalline Solids, 2003. 317: p. 1-9.

9. Takeuchi, A. and Inoue, A., Journal of Metastable and Noncrystalline Materials, 2000. 8: p. 37.

10. Egami, T., Journal of Non-Crystalline Solids, 2003. 317: p. 30.

11. Foley, J. and Perepezko, J., Journal of Non-Crystalline Solids, 1996. 205-207: p. 559.

12. Li, Q., Johnson, E., Johansen, A., and Sarholt-Kirstensen, L., Journal of Materials Research, 1992. 7: p. 2756.

13. Chen, H., Rep. Prog. Phys., 1980. 43: p. 353.

14. Dougherty, G., Shiflet, G., and Poon, S., Acta Metall. Mater., 1994. 42: p. 2275.

15. Bian, X.F., Sun, B.A., Hu, L.N., and Jia, Y.B., Physics Letters, 2005. 335: p. 61-67.

16. Angell, C., Science, 1995. 267: p. 1924-1935.

17. Dougherty, G., Shiflet, G., and Poon, J., Acta Metal. Mater., 1994. 42: p. 2275-2283.

18. Benameur, T., Inoue, A., and Masumoto, T., Mater. Trans. JIM, 1994. 35: p. 451-457.

19. Eckert, J., Mat. Sci. & Engr. A, 1997. 226-228: p. 364-373.

20. Suryanarayana, C., Progress in Materials Science, 2001. 46: p. 1-184.

21. Schwarz, R., Petrich, R., and Saw, C., Journal of Non-Crystalline Solids, 1985. 76.

22. Eckert, J., Schwartz, L., and Urban, K., Journal of Non-Crystalline Solids, 1991. 130.

23. Nakazato, K., Kawamura, Y., Tsai, A.P., and Inoue, A., Appl. Phys. Lett, 1993. 63: p. 2644.

24. Guo, F., Poon, S., and Shiflet, G., Scripta Materialia, 2000. 43: p. 1089-1095.

25. Choi-Yim, H., Busch, R., and Johnson, W.L., Journal of Applied Physics, 1998. 83: p. 7993.

26. Liu, C.T., Chisholm, M.F., and Miller, M.K., Intermetallics, 2002. 10: p. 1105.

27. Lu, Z.P. and Liu, C.T., Journal of Materials Science, 2004. 39: p. 3965 – 3974.

28. Wilson, T.W., Choo, H., Porter, W.D., Speakman, S.A., and Liaw, P.K., Journal Non-Crystalline Solids, 2006. 352: p. 4024-4029.

29. Zhang, Y., Pan, M.X., Zhao, D.Q., Wang, R.J., and Wang, W.H., Mater. Trans. JIM, 2000. 41: p. 1410.

30. Xing, L.Q., Mukhopadhyay, A., Buhro, W.E., and Kelton, K.F., Philosophical Magazine Letters, 2004. 84(5): p. 293–302.

31. Chen, L. and Spaepen, F., Nature, 1988. 336: p. 366.

32. Wilson, T.W., J.Bai, and Choo, H., Materials Letters, 2008. MLBLUE-D-07-04092.

33. Egami, T. and Billinge, S.J.L., Underneath the Bragg Peaks: Structural Analysis of Complex Materials. 2003, New York: Pergamon Press.

34. Debye, P. and Menke, H., Phys Z, 1930. 31: p. 797.

35. Proffen, T., Billinge, S.J.L., Egami, T., and Louca, D., Z. Kristallogr, 2003. 218: p. 132.

36. Waseda, Y., Structure of Non-Crystalline Materials. 1980, New York: McGraw-Hill. 60.

37. Fan, C., Liaw, P.K., Wilson, T.W., Choo, H., Gao, Y.F., Liu, C.T., Proffen, T., and Richardson, J.W., Applied Physics Letters, 2006. 89: p. 231920.

38. Dmowski, W., Fan, C., Morrison, M., Liaw, P.K., and Egami, T., Materials Science and Engineering A, 2007. 471: p. 125-129.

39. Poulsen, H.F., Wert, J.A., Neuefeind, J., Honkimaki, V., and Daymond, M., Nature materials, 2005. 4: p. 33-36.

40. Hufnagel, T.C., Ott, R.T., and Almer, J., Physical Review B, 2006. 76: p. 064204.

41. Klement, K., Willens, R.H., and Duwez, P., Nature, 1960. 187.

42. Smith, C.H. Rapidly Solidified Alloys: Processes, Structure, Properties, and Applications, ed. R. Liberman. 1993, New York: Butterworths.

43. Drehman, A., Greer, A., and Turnbull, D., Applied Physics Letters, 1982. 41: p. 716-717.

44. Greer, A., Science, 1995. 267: p. 1947-1953.

45. Basu, J. and Ranganthan, S., Sadhana, 2003. 28: p. 783-798.

46. Ashby, M., Materials Selection in Mechanical Design. 1992, Oxford: Pergamon.

47. Sudarsan, U., Chattopadhyay, K., and Kishore. in Proceedings of the Fifth International Confrence on Rapidly Quenched Metals. 1985: North-Holland, Amsterdam, Neth.

48. Turnbull, D., Contemp. Physics, 1963. 10: p. 473.

49. Inoue, A., Bulk Amorphous Alloys Preparation and Fundamental Characteristics. 1998: Trans Tech Publications.

50. Lu, Z.P. and Liu, C.T., Intermetallics, 2004. 12: p. 1043-1053.

51. Lu, Z.P. and Liu, C.T., Acta Materialia, 2002. 50: p. 3501–3512.

52. Lu, Z.P. and Liu, C.T., Physical Review Letters, 2003. 91: p. 115505.

53. Inoue, A., Acta Metall., 2000. 48: p. 279-306.

54. Peker, A. and Johnson, W.L., Appl. Phys. Lett., 1993. 63: p. 2342-2344.

55. Mastsubara, E., Tamura, T., Waseda, Y., Inoue, A., Kohinata, M., and Masumoto, T., Mater. Trans. JIM, 1990. 31: p. 228-231.

56. Inoue, A., Shinohara, Y., and Gook, J.S., Mater. Trans. JIM, 1995. 36: p. 1427-1433.

57. Imafuku, M., Sato, S., Koshiba, H., Matsubara, E., and Inoue, A., Scripta Materialia, 2001. 44: p. 2369-2372.

58. Inoue, A., Bulk Amorphous Alloys: preparation and functional characteristics. 1989, Uetikon-Zurich: Trans Tech Publications.

59. Li, Y., Ding, J., and Wang, X., Phys. Stat. Sol. A. Appl. Res., 1999. 172: p. 461-468.

60. Chen, H., Acta Metall., 1974. 22: p. 897-900.

61. Inoue, A., Nakamura, T., Nishiyama, N., and Masumoto, T., Mater. Trans. JIM, 1992. 33(937-945).

62. Inoue, A., Mater. Trans. JIM, 1995. 36: p. 866.

63. Inoue, A., Zhang, T., Nishiyama, N., Ohba, K., and Masumoto, T., Mater. Trans. JIM, 1993. 34(1234-1237).

64. Eckert, J., Schultz, L., Hellstern, E., and Urban, K., Journal of Applied Physics, 1988. 64: p. 3224-3228.

65. Egami, T. and Billinge, S., Underneath the Bragg Peak - Structural Analysis of Complex Materials. 2003, New York: Pergamon.

66. Chen, H., Journal Non-Crystalline Solids, 1981. 46: p. 289.

67. Ahn, K., Louca, D., Poon, S.J., and Shiflet, G., J. Phys: Condensed Matter, 2003. 15: p. s2357-s2364.

68. Miracle, D., Nature materials, 2004. 3: p. 697-702.

69. Greer, A., Rapidly Solidified Alloys: Processes, Structure, Properties, and Applications, H.H. Liebermann, Editor. 1993, Mercel Dekker: New York. p. 269-301.

70. Wei, W., Li, L., Pan, M., and Wang, R., Physical Review B, 2002. 63: p. 52204.

71. Flores, K.M., Suh, D., Dauskardt, R.H., Asoka-Kumar, P., Sterne, P.A., and Howell, R.H., Journal of Materials Research, 2002. 17: p. 1153-1161.

72. Inoue, A., Zhang, T., and Masumoto, T., Mater. Trans. JIM, 1995. 36: p. 391.

73. Mattern, N., Hermann, H., Roth, S., Sakowski, J., Macht, M., Jovari, P., and Jiang, J., Applied Physics Letters, 2003. 82: p. 2589-2591.

74. Li, G., Wang, L.M., Zhan, Z.J., Sun, L.L., Zhang, J., and Wang, W.K., Journal of Physics - Condensed Matter, 2002. 14: p. 11077-11080.

75. Perarskaya, E., Loffler, J.F., and Johnson, W.L., Acta Materialia, 2003. 51: p. 4045-4057.

76. Datta, A., Cristofaro, N.J., and Davis, A. in Fourth International Confrence on Rapidly Quenched Metals. 1982. Sendai.

77. Kim, Y., Inoue, A., and Masumoto, T., Mater. Trans. JIM, 1991. 32: p. 599-603.

78. Inoue, A., Tomioka, H., and Masumoto, T., J. Materials Science, 1983. 18: p. 153-160.

79. Inoue, A., Zhang, T., and Masumoto, T., Mater. Trans. JIM, 1989. 30: p. 965-972.

80. Inoue, A., Yamaguchi, Y., Zhang, T., and Masumoto, T., Mater. Trans. JIM, 1990. 31: p. 104-109.

81. Kim, S., Inoue, A., and Masumoto, T., Mater. Trans. JIM, 1991. 32: p. 875-878.

82. Inoue, A., Shibata, T., and Masumoto, T., Mater. Trans. JIM, 1992. 33: p. 491-496.

83. Inoue, A., Nishiyama, N., and Masumoto, T., Mater. Trans. JIM, 1996. 37: p. 181-184.

84. Inoue, A., Shibata, T., and Zhang, T., Mater. Trans. JIM, 1995. 36: p. 1420-1426.

85. Fan, C., Louzguine, D., Li, C., and Inoue, A., Appl. Phys. Lett., 1999. 75: p. 340-342.

86. Fan, C., Imafuku, M., Kurokawa, H., and Inoue, A., Scripta Materialia, 2001. 44: p. 1993-1997.

87. Inoue, A., Bulk Amorphous Alloys - Practical Characteristics and Applications. 1999.

88. Fan, C., Imafuku, M., Kurokawa, H., and Inoue, A., Appl. Phys. Lett., 2001. 79: p. 1792-1794.

89. Egami, T., Journal of Materials Science, 1978. 13: p. 2597-2599.

90. Fan, C., Wilson, T., Dmowski, W., Choo, H., Richardson, J., Maxey, E., and Liaw, P., Intermetallics, 2006. 14: p. 888.

91. Waseda, Y. and Egami, T., J. Mater. Sci., 1978. 14: p. 1249.

92. Srolovitz, D., Egami, T., and Vitek, V., Physical Review B, 1981. 24: p. 6936.

93. Inoue, A., Kitamura, A., and Masumoto, T., J. Materials Science, 1981. 16: p. 1895.

94. Suzuki, R., Komatsu, Y., Kobayashi, K., and Shingu, P., J. Materials Science, 1983. 18: p. 1195-1201.

95. Inoue, A., Bizen, Y., Kimura, H., Yamamoto, M., Tsai, A., and Masumoto, T., J. of Mat. Sci. Lett., 1987. 6: p. 811-814.

96. Inoue, A., Yamamoto, M., Kitamura, A., and Masumoto, T., J. of Mat. Sci. Lett., 1987. 6: p. 194-196.

97. Tsai, A., Inoue, A., and Masumoto, T., Met. Trans., 1988. 19A: p. 1369-1371.

98. Tsai, A., Inoue, A., and Masumoto, T., J. Mater. Sci. Lett, 1988. 7: p. 805-807.

99. Inoue, A., Ohtera, K., Tsai, A., and Masumoto, T., Jpn. J. Appl. Phys., 1988. 27: p. L1579-L1582.

100. Nandi, P., Chattopadhyay, P., Pabi, S., and Manna, I., Mat. Sci. & Engr. A, 2003. 359: p. 11.

101. Guo, F., Enouf., S., Poon, J., and Shiflet, G., Phil. Mag. Lett., 2001. 81: p. 203-211.

102. Perepezko, J., Herbert, R., Wu, R., and Wilde, G., Journal Non-Crystalline Solids, 2003. 317: p. 52-61.

103. Borner, I. and Eckert, J., Scripta Materialia, 2001. 45: p. 237.

104. Hsieh, H., Toby, B., Egami, T., He, Y., Poon, J., and Shiflet, G., J. Materials Research, 1990. 5: p. 2807-2812.

105. Hsieh, H., Egami, T., He, Y., Poon, J., and Shiflet, G., Journal Non-Crystalline Solids, 1991. 135: p. 248-254.

106. Ahn, K., Louca, D., Poon, S.J., and Shiflet, G.J., Physical Review B, 2004. 70: p. 224103.

107. Spaepen, F. and Turnbull, D., Rapidly Quenched Metals 2, ed. M. Grant and B. Giessen. Vol. 2. 1976, Cambridge, MA.

108. Egami, T., Mat. Sci. & Engr. A, 1997. 226-228: p. 261-267.

109. Angell, C., Journal Non-Crystalline Solids, 1985. 73: p. 1-17.

110. Novikov, V. and Sokolov, A., Nature, 2004. 431: p. 961-963.

111. Louca, D., Ahn, K., Soper, A.K., Poon, S.J., and Shiflet, G.J., Materials Research Society Symposium Proceedings, 2004. 806: p. MM 9.2.1.

112. Kim, Y., Inoue, A., and Masumoto, T., Mater. Trans. JIM, 1990. 31: p. 747-749.

113. Zhou, F., Luck, R., Lu, K., Lavernia, E., and Ruhle, M., Philosophical Magazine Letters, 2002. 82: p. 1003.

114. Chen, H., He, Y., Shiflet, G., and Poon, S., Scripta Metall. Mater., 1991. 25: p. 1421-1424.

115. Foley, J., Allen, D., and Perepezko, J., Scripta Materialia, 1996. 35: p. 655-660.

116. Allen, D., Foley, J., and Perepezko, J., Acta Materialia, 1998. 46: p. 431-440.

117. Masumoto, T., Materials Science of Amorphous Alloys. 1983, Tokyo: Uhma.

118. Senkov, O.N. and Miracle, D.B., Materials Research Bulletin, 2001. 36: p. 2183–2198.

119. Egami, T. and Waseda, Y., Journal Non-Crystalline Solids, 1984. 64: p. 113-134.

120. Senkov, O. and Miracle, D., Journal Non-Crystalline Solids, 2003. 317: p. 34-39.

121. Inoue, A., Ohtera, K., Tsai, A., and Masumoto, T., Jpn. J. Appl. Phys., 1988. 27: p. L280-L282.

122. Chung, K.S., Bai, J., Sparks, C.J., and Ice, G.E. in 11th Synch. Rad. Conf. 2000: AIP Press.

123. Habernschuss, A., Ice, G.E., Sparks, C.J., and Neiser, R.A., The ORNL beamline at the National Synchrotron Light Source. Nucl. Instrum. Methods Phys. Res. A, 1988. 266: p. 215.

124. Margulies, L., Kramer, M.J., McCallum, R.W., Kycia, S., Haeffner, D.R., Lang, J.C., and Goldman, A.I., New high temperature furnace for structure refinement by powder diffraction in controlled atmospheres using synchrotron radiation. Review of Scientific Instruments, 1999. 70(9): p. 3554-3561.

125. Hammersley, A.P., Svensson, S.O., Hanfland, M., Fitch, A.N., and Häusetmann, D., High Press. Res., 1996. 14: p. 235.

126. International Tables for X-ray Crystallography. 1968, Birmingham, England.

127. Boer, F.d., Boom, R., Matterns, W., Miedema, A., and Niessen, A., Cohesion in Metals: Transition Metal Alloys. 1988, North Holland, Amsterdam.

128. Louzguine, D. and Inoue, A., Journal of Light Metals, 2001. 1: p. 105.

129. Louzguine, D. and Inoue, A., Journal of Alloys and Compounds, 2005. 399: p. 78-85.

130. Senkov, O., Scott, J., and Miracle, D., Journal of Alloys and Compounds, 2002. 337: p. 83.

131. Gangopadhyay, A. and Kelton, K., Philosophical Magazine Letters, 2000. 80: p. 1193.

132. Christian, J., The Theory of Transformation in Metals and Alloys: Equilibrium and General Kinetic Theory. 2nd ed. 1975, Oxford: Pergamon.

133. Ma, X., Yang, Y., Dong, Y., and He, Y., Acta Metallurgica Sinica, 1992. 5: p. 323.

134. Chang, I., Svec, P., Gogebakan, M., and Cantor, B., Material Science Forum, 1996. 225-7: p. 335.

135. Kissinger, H., Analytical Chemistry, 1957. 29: p. 1702-1706.

136. ASM Handbook: Alloy Phase Diagrams, ed. H. Baker. 1992, Materials Park, OH.

137. He, Y., Shiflet, G., and Poon, S., Acta Metall. Mater., 1995. 43: p. 83.

138. Gleiter, H., Acta Materialia, 2001. 48: p. 1.

139. Sun, W. and Quan, M., Materials Letters, 1996. 27: p. 101.

140. Kelton, K., Croat, T., Gangopadhyay, A., Xing, L., Greer, A., Weyland, M., Li, X., and Rajan, K., Journal of Non-Crystalline Solids, 2003. 317: p. 71.

141. Zhang, Y., Pan, M.X., Wang, R.J., and Wang, W.H., Mater. Trans. JIM, 2000. 41: p. 1410.

142. Fan, C., Liaw, P.K., Wilson, T.W., Dmowski, W., Choo, H., and Liu, C.T., Appl. Phys. Lett., 2006. 89: p. 111905.

143. Sheng, H.W., Luo, W.K., Alamgir, F.M., Bai, J.M., and Ma, E., Nature, 2006. 439: p. 419-425.

144. Sadoc, A., Hackmann, O., Nassif, V., Proux, O., Hazemann, J.L., Xing, L.Q., and Kelton, K.F., Journal Non-Crystalline Solids, 2007. 353: p. 2758-2766.

145. Debye, P. and Menke, H., Phys. Z, 1930. 31: p. 797.

146. Kelton, K.F., Journal of Alloys and Compounds, 2007. 434-435: p. 115-118.

147. Hoyer, W. and Jodicke, R., Journal Non-Crystalline Solids, 1995. 192 & 193: p. 102-105.

148. Saksl, K., Jovari, P., Franz, H., and Jiang, J.Z., Journal of Applied Physics, 2007. 97: p. 113507.

149. Cardellini, F., Contini, V., Mazzone, G., and Montone, A., Synthesis of nanocrystalline iron aluminides by mechanical alloying. Materials Science Forum, 1995. 195: p. 19-24.

150. Sasaki, T.T., Mukai, T., and Hono, K., Scripta Materialia, 2007. 57: p. 189-192.

151. Shabashov, V.A., Brodova, I.G., Mukoseev, A.G., Sagaradze, V.V., and Litvinov, A.V., Deformation-induced phase transformatin in the Al-Fe system under intensive plastic deformation. J. Phys.: Condens. Matter, 2007. 19: p. 386222.

152. Xu, D., Duan, G., and Johnson, W.L., Physical Review Letters, 2004. 92: p. 245504.

153. Louzguine-Luzgin, D.V., Xie, G., Zhang, W., and Inoue, A., Materials Science and Engineering A, 2007. 465: p. 146-152.

154. Oh, J.C., Ohkubo, T., Kim, Y.C., Fleury, E., and Hono, K., Scripta Materialia, 2005. 53: p. 165.

155. Park, E.S. and Kim, D.H., Acta Materialia, 2006. 54: p. 2597-2604.

156. Park, E.S., Chang, H.J., Kim, D.H., Ohkubo, T., and Hono, K., Scripta Materialia, 2006. 54: p. 1569.

157. Zhang, L., Wu, Y., Bian, X., Li, H., Wang, W., Li, J., and Lun, N., J. Phys: Condensed Matter, 1999. 11: p. 7959-7969.

158. Ehrenfest, P., Proc. Amsterdam Acad., 1915. 17: p. 1184.

159. Pauling, L., Journal of the American Chemical Societyy, 1947. 63: p. 542 - 553.

160. Krishan, K., Journal of Non-Crystalline Solids, 1982. 53: p. 83-104.

161. Tiwari, G.P., Ramanujan, R.V., Gonal, M.R., Prasad, R., Raj, P., Badguzar, B.P., and Goswami, G.L., Materials Science and Engineering A, 2001. 304-306: p. 499-504.

162. Turnbull, D., Contemp. Physics, 1969. 10: p. 473.

163. Thornburg, D.D., Materials Research Bulletin, 1974. 9: p. 1481.

164. Clavaguera, N., Clavaguera-mora, M.T., and Casasvazquez, J., Journal of Non-Crystalline Solids, 1976. 22: p. 23.

165. Schoers, N.J., Loffler, J.F., Pekarskaya, E., Busch, R., and Johnson, W.L., Materials Science Forum, 2001. 360: p. 79-84.

166. Jacovkis, D., Xiao, Y., Rodriguez-Viejo, J., Clavaguera-Mora, M.T., and Clavaguera, N., Acta Materialia, 2004. 52: p. 2819-2826.

167. Lin, Z., Youshi, W., Xiufang, B., Hui, L., Weimin, W., Jingguo, L., and Ning, L., Journal of Physics: Condensed Matter, 1999. 11: p. 7959.

168. Lin, X.H., Johnson, W.L., and Rhim, W.K., Mater. Trans. JIM, 1997. 38: p. 473-477.

169. Chan, H.W., Materials and Design, 1988. 9: p. 355-358.

170. Johnson, W.L., Intermetallic compounds. Vol. 1. 1994, New York: Wiley.

171. Gilbert, C.J., Ritchie, R.O., and Johnson, W.L., Applied Physics Letters, 1997. 71: p. 476.

172. Yang, B., Liaw, P.K., Wang, G., Morrison, M., Liu, C.T., Buchanan, R.A., and Yokoyama, Y., Intermetallics, 2004. 12: p. 1265.

173. Weaire, D., Ashby, M.F., Logan, J., and Weins, M.J., Acta Metall., 1971. 19: p. 779.

174. Knuyt, G., Deschepper, L., and Stals, L.M., Journal of Physics F Metal Phys., 1986. 16: p. 1989.

175. Argon, A.S. and Shi, L.T., Acta Metall., 1983. 31: p. 499.

176. Bruck, H.A., Christman, T., Rosakis, A.J., and Johnson, W.L., Scripta Metall. Mater., 1994. 30: p. 429.

177. Conner, R.A., Rosakis, A.J., Johnson, W.L., and Owen, D.M., Scripta Materialia, 1997. 37: p. 1373.

178. Liu, C.T., Heatherly, L., Easton, D.S., Carmichael, C.A., Schneibel, J.H., Chen, C.H., Wright, J.L., Yoo, M.H., Horton, J.A., and Inoue, A., Metall. Mater. Trans., 1998. A 29: p. 1811.

179. Hufnagel, T.C., Fan, C., Ott, R.C., Li, J., and Brennan, S., Intermetallics, 2002. 10: p. 1163.

180. Milberg, M.E., J. Appl. Phys., 1962. 33: p. 1766.

181. Suzuki, Y., Haimovich, J., and Egami, T., Physical Review B, 1987. 35: p. 2162.

182. Lewandowski, J., Wang, W., and Greer, A.L., Philosophical Magazine Letters, 2005. 85: p. 77.

183. Simmons, G. and Wang, H., Single Crystal Elastic Constants and Calculated Aggregate Properties: A Handbook. 1971, Cambridge, MA: MIT Press.

184. Ashby, M.F., Nelson, A.N., and Centamor, R.M., Scripta Metallurgica, 1970. 4: p. 715.

185. Barmatz, M. and Chen, H.S., Physical Review B, 1974. 9: p. 4073.

186. Srolovitz, D., Vitek, V., and Egami, T., Acta Metall., 1983. 32: p. 335.

187. Chen, H.S., J. Appl. Phys., 1978. 49: p. 3289.

188. Miracle, D., Sanders, W., and Senkov, O., Phil Mag. A, 2003. 83: p. 2409.

189. Fan, C., Liaw, P.K., Haas, V., Wall, J.J., Choo, H., Inoue, A., and Liu, C.T., Physical Review B, 2006. 74: p. 014205.

190. Argon, A.S., Acta Metall., 1979. 27: p. 47.

191. Schuh, C.A., Lund, A.C., and Nieh, T.G., Acta Materialia, 2004. 52: p. 5879.

192. Inoue, A., Ohtera, K., and Masumoto, T., Jpn. J. Appl. Phys., 1988. 27: p. L736.

193. Boer, F.R.d., Boom, R., Matters, W.C.M., Miedema, A.R., and Niessen, A.k., Cohesion in Metals: Transition metal alloys. 1988, New York: North Holland.

194. Gu, X., Xing, L., and Hufnagel, T., Journal Non-Crystalline Solids, 2002. 311: p. 77-82.

Appendix

Table 2-1. Comparison of bulk amorphous alloys to conventional alloys [3].

	Conventional Metals (Ferrous , Al-based, and Ti-based alloys)	**Bulk Amorphous Alloys (typical properties)**
Strength (MPa)	Al-based – 200–300 Ti-based – 300–1,000 Ferrous-based – 300–2000	Al-based – 800–1,500 Zr-based – 1600–2,000 Ferrous-based – 2,000–3500
Stiffness (Youngs Modulus) (GPa)	Al-based – 60–80 Ti-based – 100–120 Ferrous-based – 150–200	Al-based – 60–80 Zr-based – 80–105 Ferrous-based – 140–160
Density ($gram/cm^3$)	Al-based – 3–4 Ti-based – 4—5 Ferrous-based – 7–8	Al-based – ~3–4 Zr-based – ~6 Ferrous -based – 7–8
Toughness ($MPa\text{-}m^{1/2}$)	High values ~ 20–120 $MPa\text{-}m^{1/2}$	High values ~ 20–60 $MPa\text{-}m^{1/2}$ Can be increased using 2nd-phase additions [see, for example, Reference 15]
Plastic Strain to Failure (%)	Typical large in all loading geometries (2–50%)	Large in confined geometry Limited (≤ 1%) in unconfined geometry (e.g., tension) but, can be extended to 5% or more using 2nd-phase additions [see Reference 15]
Cost of raw ingot material ($ per Kg)	Al-based – $2–5 Ti-based – $15–30 Ferrous-based – $0.60–$10	Al-based – $2–5 Zr-based – $25–40 Ferrous-based – $1–10
Process/Manufacturing Technology	Conventional casting, forging, etc. Heat treatment, extrusion, etc. Substantial machining required to achieve net shapes High costs	Metal mold die casting Thermoplastic-forming (undercooled liquid state) Very near net shapes No heat treatment—final properties in cast state Little or no machining required Lower costs

Table 2-2. Various methods of producing metallic glasses grouped into different classes [44].

Method	Technique
Rapid Liquid Cooling	Melt-spinning
	Planar flow casting
	Wire formation in water
	Scanned laser or electron beam
	Pulsed laser beam
Undercooking of clean liquids	Emulsion
	Fluxing
	Solidification in free fall
Physical vapor deposition	Evaporation
	Sputtering
Chemical methods	Electroless deposition
	Electrodeposition
	Precipitation
	Hydrogenation
Irradiation	By light or heavy ions
	By electrons
	By neutrons
	Ion implantation
	Ion mixing
Mechanical Methods	Grinding
	Mechanical alloying
Reactions	Solid-state reaction of elements
	Decomposition of crystalline solid solution

Table 4-1. Summary of DSC results (20 K per minute heating rate). Primary crystallization temperature, T_x, and enthalpies of crystallization, ΔH_x, (kJ/mol) of amorphous/partially amorphous aluminum alloys after 30 hours of milling. Also shown is the eutectic temperature (T_e) for the transition metal and aluminum obtained from the binary phase diagrams [30].

Composition	T_x (K)	T_e (K)	ΔH_x (kJ/mol)
$Al_{85}Y_7Fe_5Ni_3$	612	913 (Al-Ni)	2.2
$Al_{85}Y_7Fe_5Fe_3$	615	928 (Al-Fe)	3.0
$Al_{85}Y_7Fe_5Co_3$	619	930 (Al-Co)	2.5
$Al_{85}Y_7Fe_5Cu_3$	590	821 (Al-Cu)	1.6
$Al_{83}Y_7Fe_5Ni_5$	668	913 (Al-Ni)	3.5
$Al_{81}Y_7Fe_5Ni_7$	672	913 (Al-Ni)	6.6

Table 4-2. Activation energy for the crystallization of various amorphous aluminum alloys prepared by mechanical alloying (MA) of powder alloys and by rapid solidification of melt-spun (MS) ribbons.

Composition	Activation Energy (kJ/mol)	Processing	Calculation method
$Al_{83}Y_7Fe_5Ni_5$	310	MA powder	JMA
$Al_{85}Y_8Ni_5Co_2$ [103]	285	MA powder	JMA
$Al_{80}Y_{15}Ni_5$ [133]	280	MA powder	Kissinger
$Al_{90}Fe_{10}$ [9]	201	MA powder	JMA
$Al_{93-x}Ni_xGd_7$ [24]	164-222	MS ribbons	Kissinger
$Al_{85}Ni_{15-x}Y_x$ [134]	221-240	MS ribbons	Kissinger
$Al_{85}Ni_5Fe_2Gd_8$ [2]	425	MS ribbons	JMA

Table 4-3. Enthalpy of mixing (kJ/mol) of constituent elements in alloys examined in this study [191].

ΔH_{mix}	Al	Y	Fe	Ti
Al		-38	-11	-30
Y	-38		-1	15
Fe	-11	-1		-17
Ti	-30	15	-17	

Table 4-4. Summary of samples used in consolidation study showing the composition (MA = mechanically alloyed, CG = coarse grain), forging temperature, # of forgings, % of theoretical density determined by Archimedes method, and ultimate compressive strength (UCS).

Sample	**Temperature °C**	**# of Forgings**	**Density %**	**UCS MPa**
100% MA	420	3	94-97*	85
85% MA + 15% CG	420	3	94	286
70% MA + 30% CG	420	3	96	305
100% MA	445	1	95	350
70% MA + 30% CG	445	1	94	285

*density of multiple pieces of fractured sample was measured

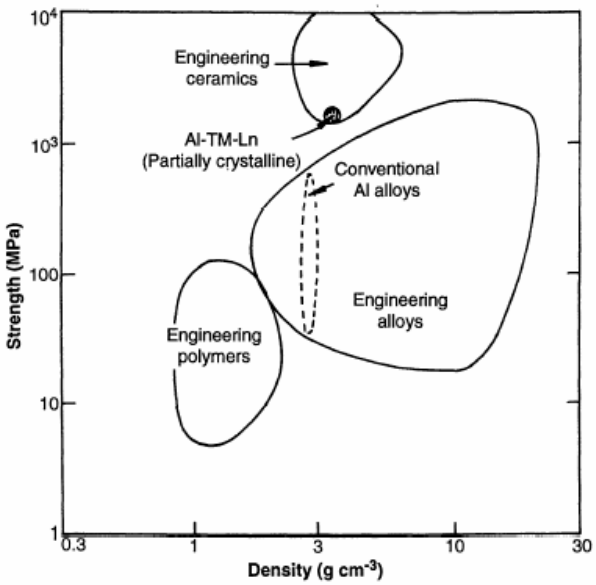

Figure 1-1. Schematic showing the strength-density relationship for various engineering materials [44].

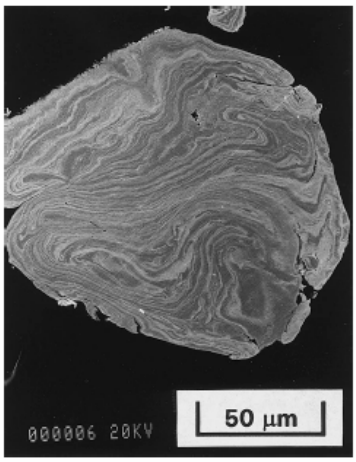

Figure 1-2. Example of layered microstructure developed during mechanical alloying as observed by scanning electron microscopy on a Ag-Cu alloy [20].

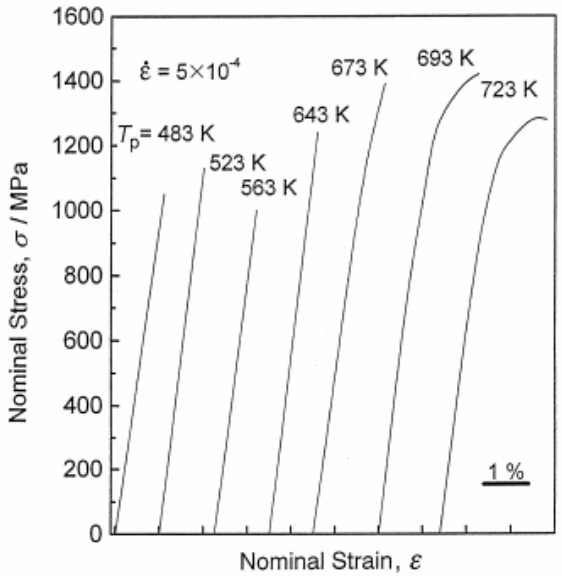

Figure 1-3. Stress-strain curves of $Al_{85}Ni_5Y_8Co_2$ consolidated at different temperatures [4].

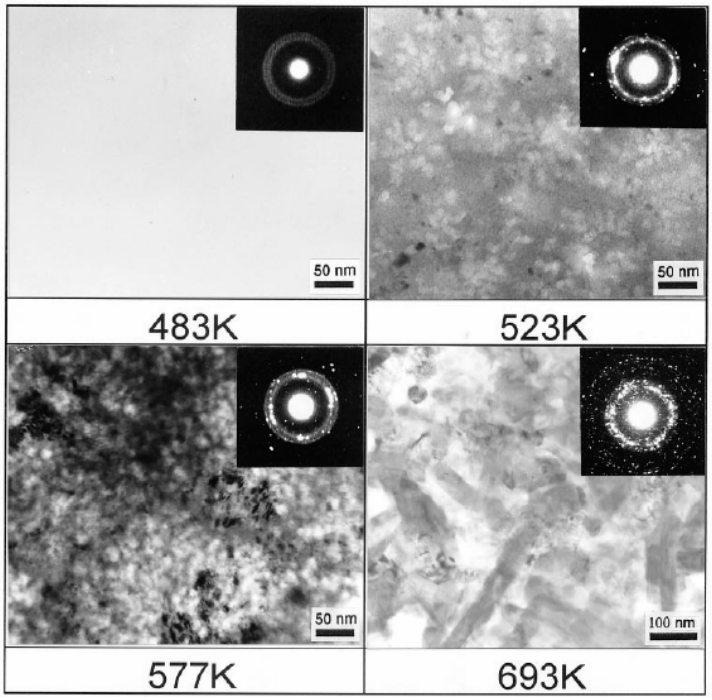

Figure 1-4. Bright-field electron micrographs and selected-area electron diffraction patterns showing microstructure of $Al_{85}Ni_5Y_8Co_2$ alloys after consolidation at 483K, 523K, 577K and 693K [4].

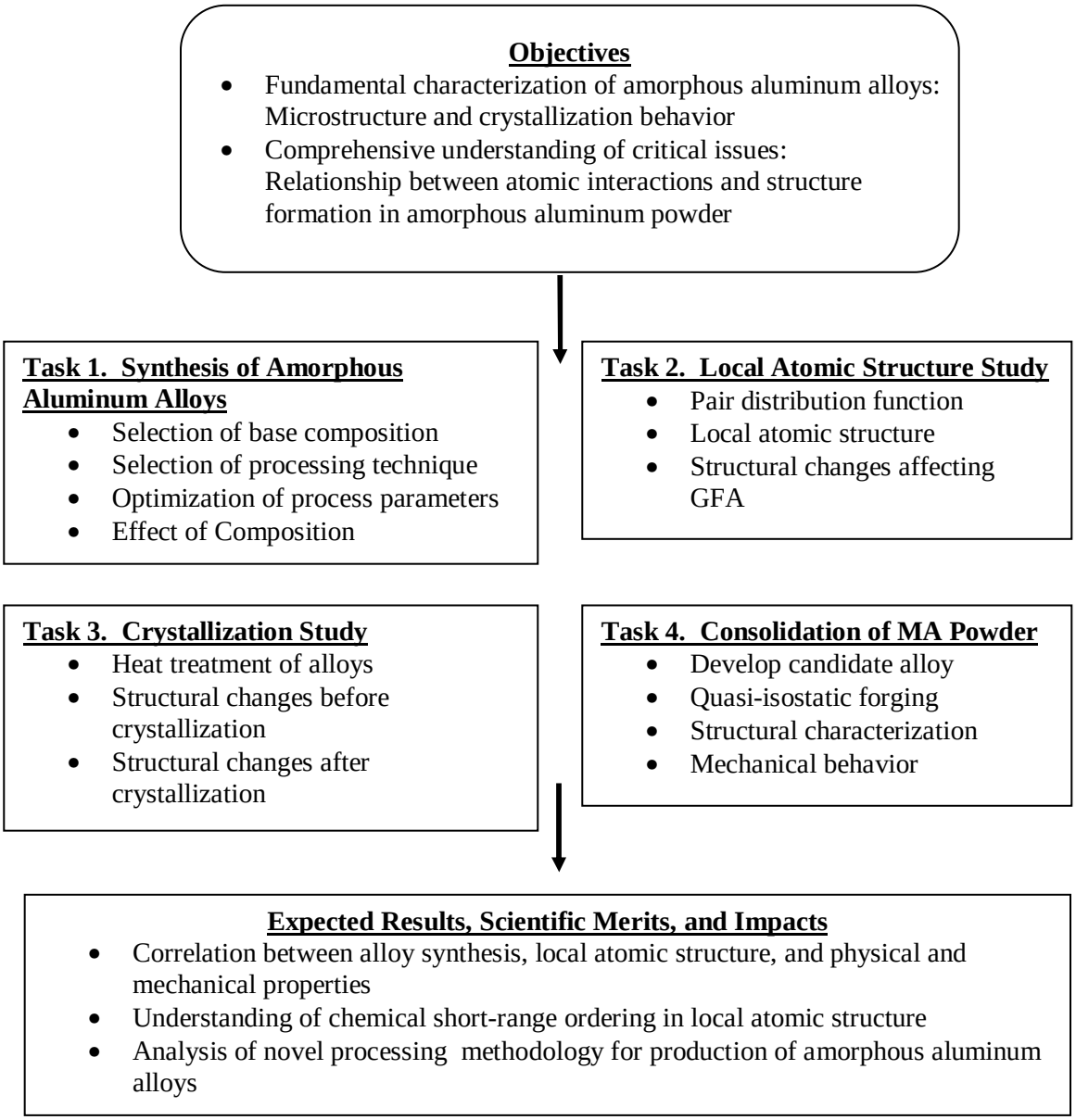

Figure 1-5. Objectives, tasks, and expected results of the current dissertation.

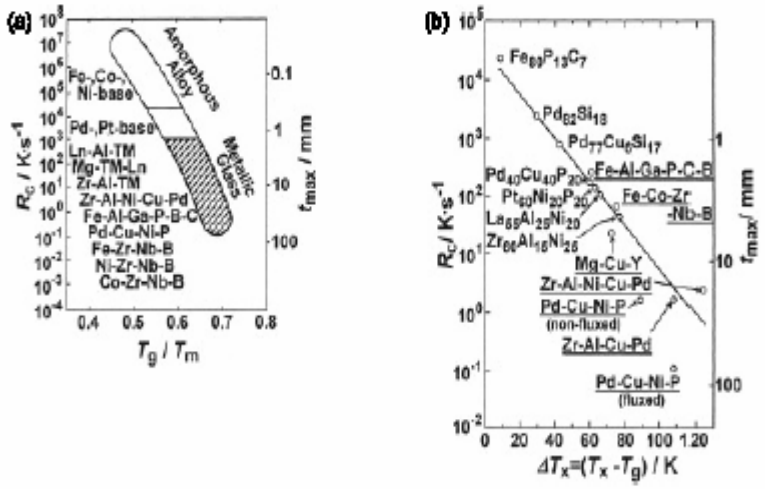

Figure 2-1. Correlation in different glass-forming alloys between (a) critical cooling rate (R_c), reduced glass-transition temperature (t_g) and thickness of glass (t_{max}), (b) critical cooling rate, (R_c) super-cooled liquid region ($T_x - T_g$) and thickness of glass (t_{max}) [49].

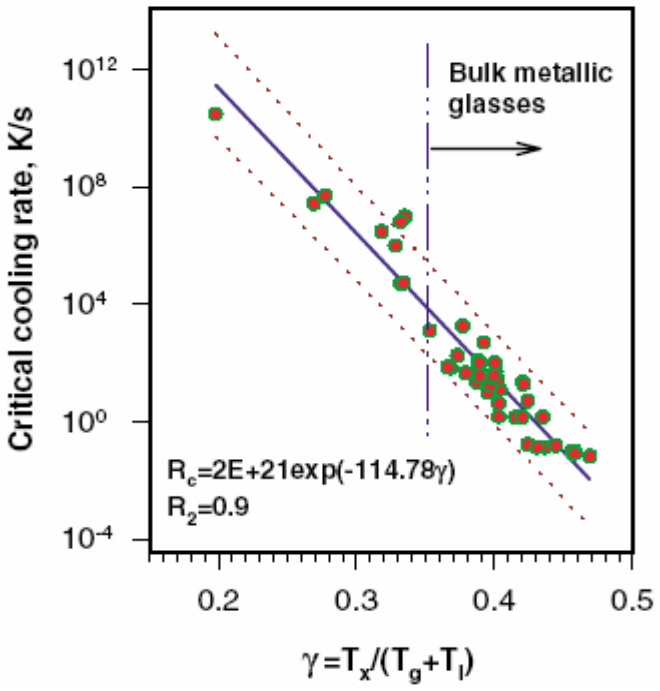

Figure 2–2. The correlation between the critical cooling rate and γ for 49 metallic glasses [52].

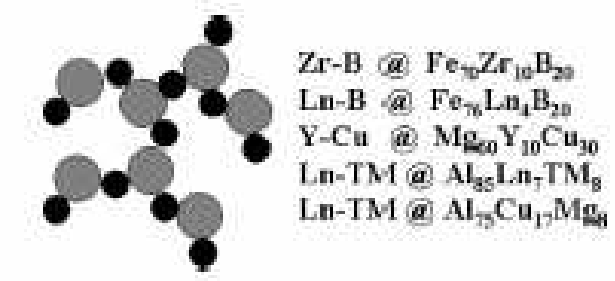

Figure 2-3. Sketch of atomistic network / backbone formed by the large and small atoms in a MSL class of metallic glasses. Several alloys are listed and there components are specified [8].

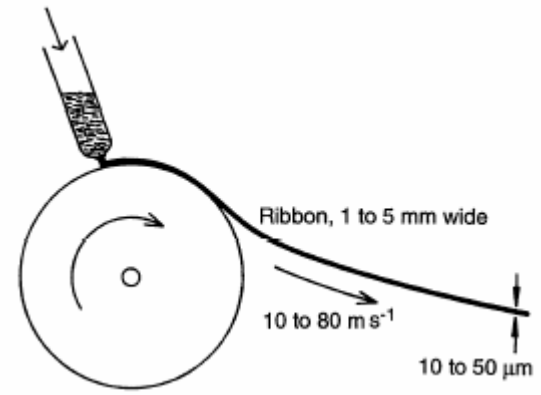

Figure 2-4. Melt-spinning schematic showing that the molten alloy is ejected onto a copper wheel and a thin ribbon is produced up to a few millimeters wide and up to about 50 micrometers thick [44].

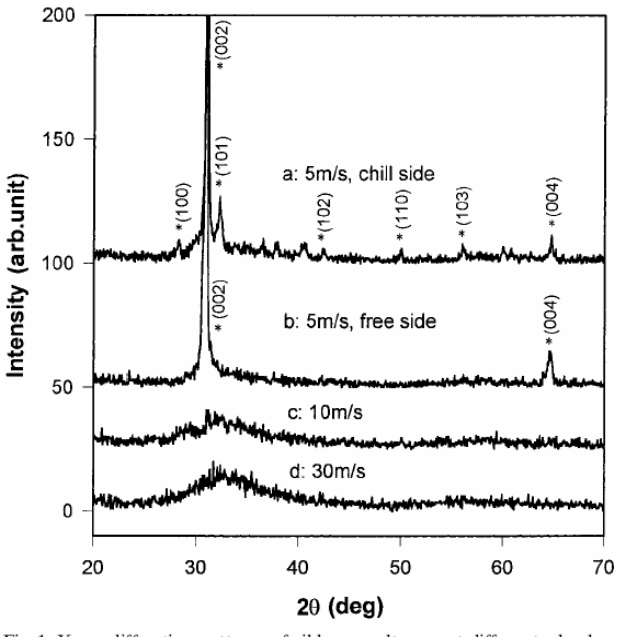

Figure 2-5. X-ray diffraction patters of melt-spun ribbons with different wheel speeds [59].

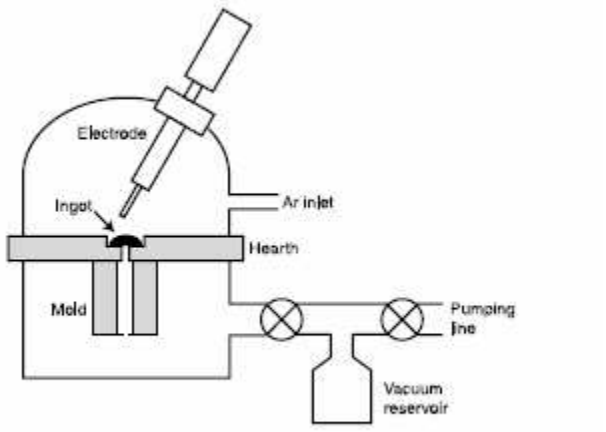

Figure 2-6. Schematic diagram of an arc melting / suction casing system [192].

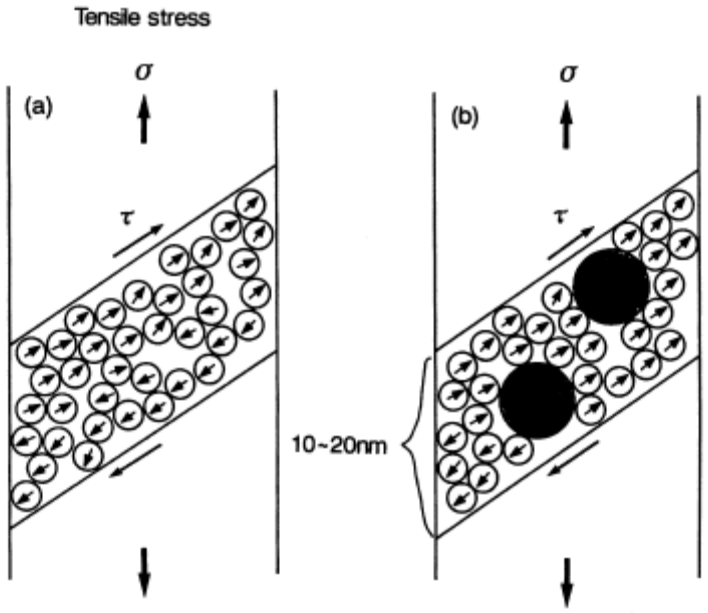

Figure 2-7. Schematic illustration showing the mechanism for shear deformation for (a) an amorphous single phase and (b) coexistent amorphous and fcc-Ni phase [5].

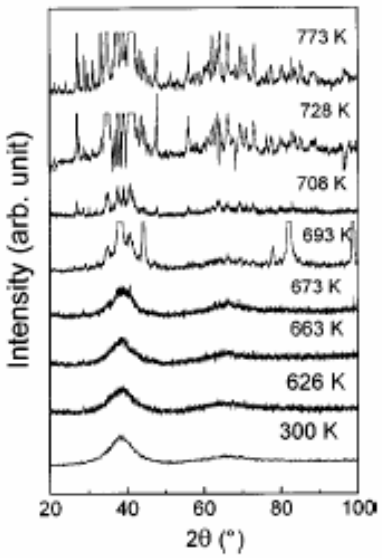

Figure 2-8. X-ray diffraction pattern of $Zr_{41}Ti_{14}Cu_{12.5}Be_{22.5}$ BMG after annealing at different temperatures [70].

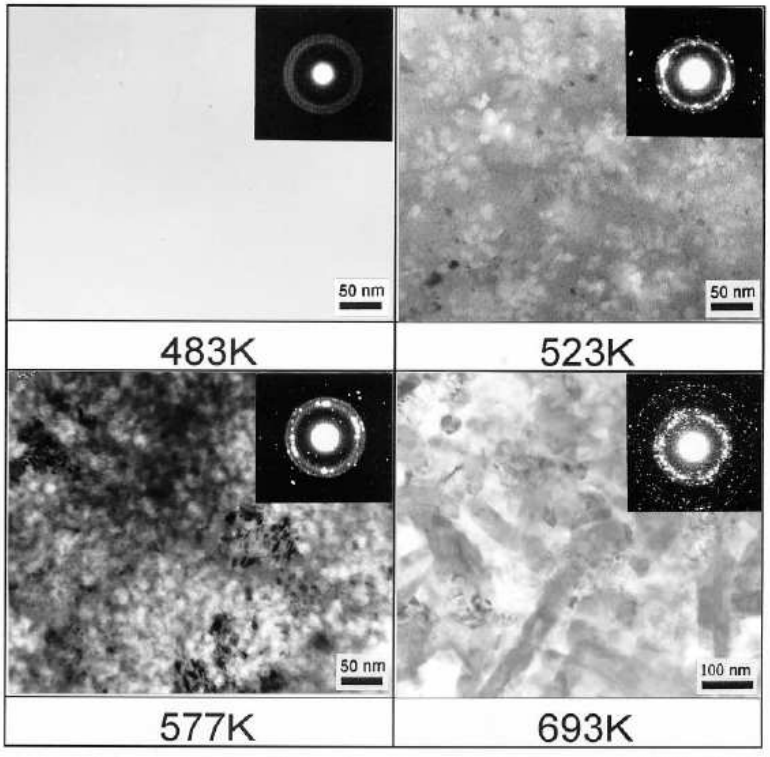

Figure 2-9. Bright field electron micrographs and selected-area diffraction patterns of $Al_{85}Ni_5Y_8Co_2$ consolidated at different temperatures [4].

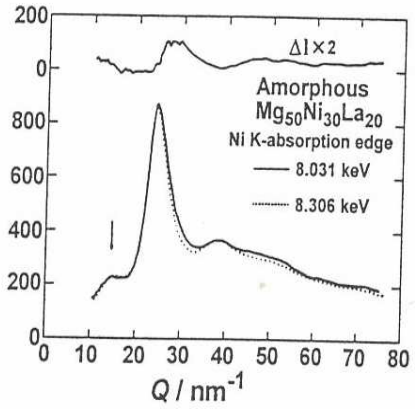

Figure 2-10. Differential intensity profile of amorphous $Mg_{50}Ni_{30}La_{20}$ alloy (top) determined from scattering intensities (bottom) measured at 8.031 keV (solid) and 8.306 keV (dotted) that correspond to energies of 300 and 25 eV below the Ni K-absorption edge. Arrow indicates prepeak [55].

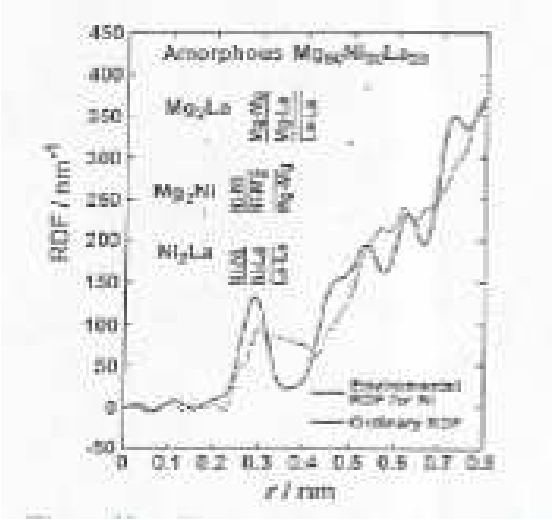

Figure 2-11. The environmental radial distribution function (RDF) for Ni (solid) and the ordinary RDF (dotted) of amorphous $Mg_{50}Ni_{30}La_{20}$ alloy [55].

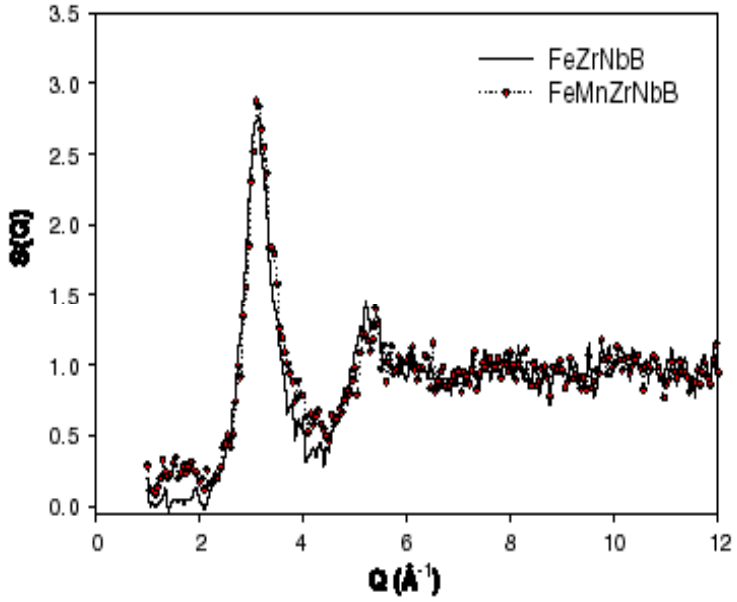

Figure 2-12, The structure function for the Fe-Zr-based alloy system. The pre-peak at about 1.5Å^{-1} is accentuated with Mn doping. This pre-peak is a manifestation of short-range chemical ordering [67].

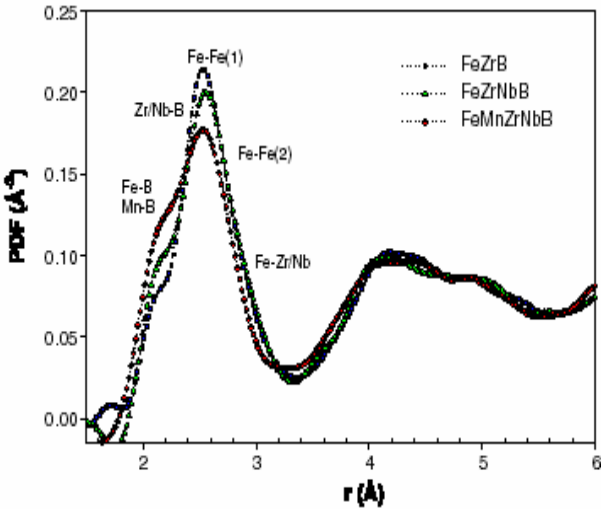

Figure 2-13. The local atomic structure for the Fe-Zr system is determined as a function of chemical substitution at room temperature. Note how the peaks shift to lower r-distances because of the volume contraction [67].

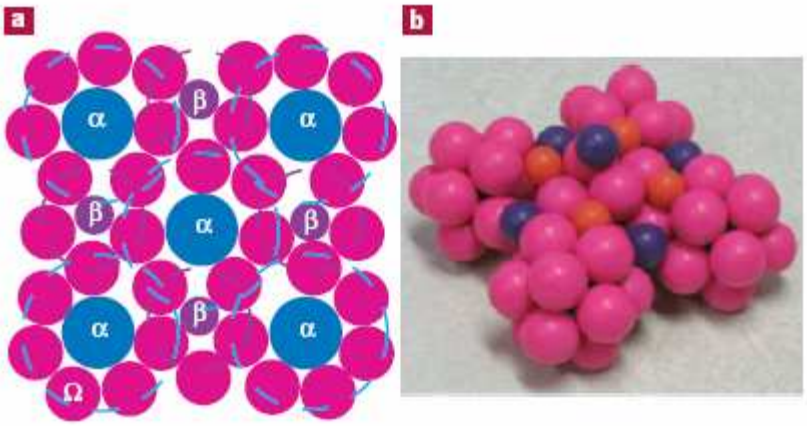

Figure 2-14. Illustrations of a portion of a single cluster unit for the dense cluster packing model. In this model, the Ω atoms are the solvent atoms and theα atoms are the largest atoms. The β atoms will fill the interstitial locations and are the smallest atoms [68].

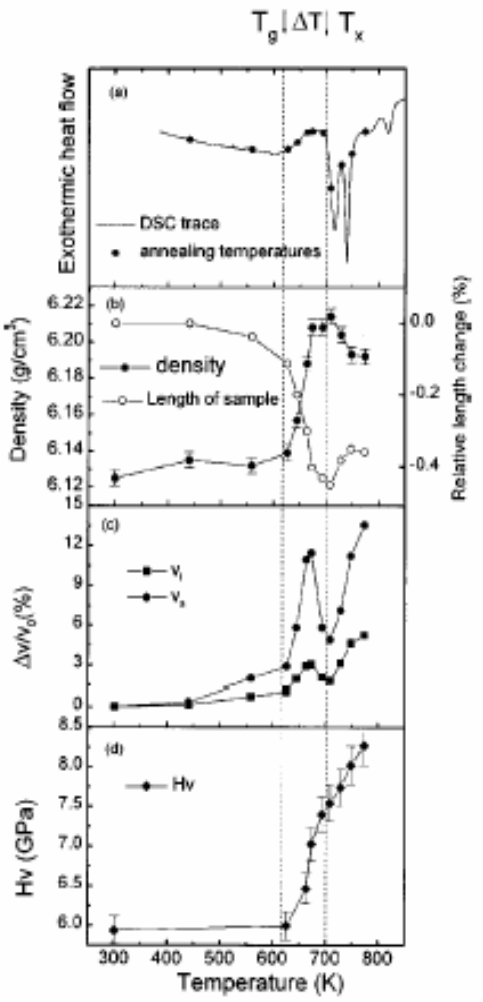

Figure 2-15. (a) DSC trace of the $Zr_{41}Ti_{14}Cu_{12.5}Ni10Be_{22.5}$ BMG; the significantly large SLR is indicated in the figure. The points show the annealing temperatures for density, microhardness, and acoustic velocities measurements. (b) The variation of the density and the relative change of the specimen length with temperature. (c) The relative longitudinal and transverse velocities change with temperature, and (d) the microhardness H_v of the BMG with temperature [70].

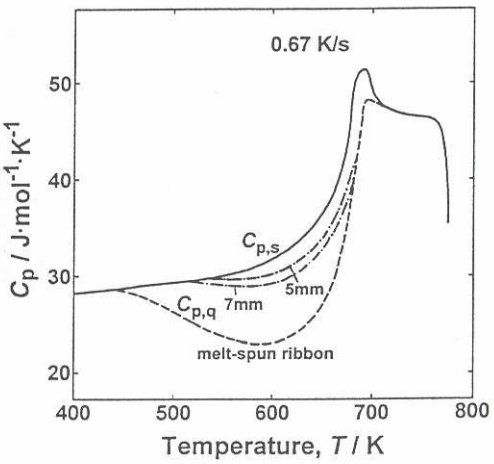

Figure 2-16. Thermograms of amorphous cylinders with diameters of 5 and 7mm. The data of the melt-spun ribbon are also shown for comparison [72].

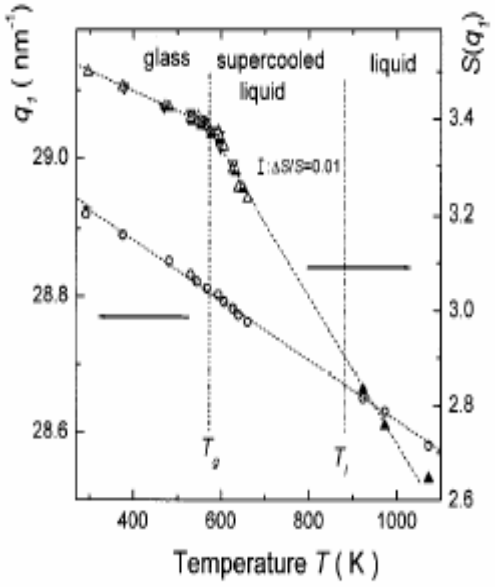

Figure 2-17. Position q_1 and height $S(q_1)$ of the first maximum of the structure factor $ST(q)$ vs temperature [73].

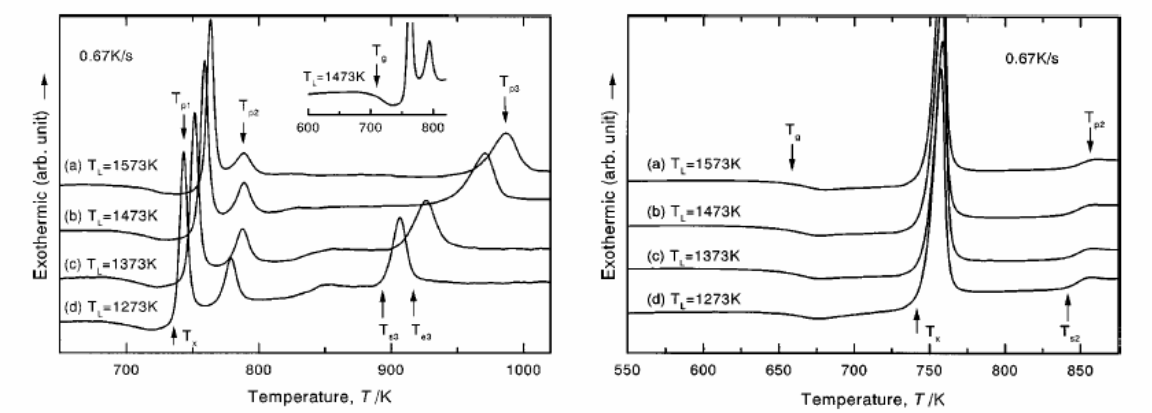

Figure 2-18. a) DSC curves of $Zr_{60}Cu_{20}Pd_{10}Al_{10}$ showing that the crystallization occurs in three stages. b) DSC curve of $Zr_{60}Cu_{27.5}Al_{7.5}$ showing that the crystallization occurs in a single stage [85].

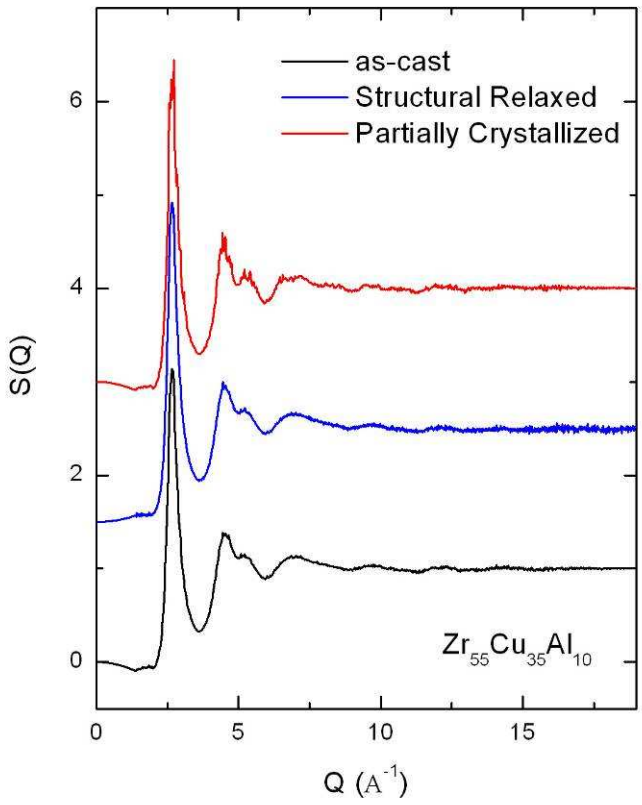

Figure 2-19. The structure factor $S(Q)$ for as-cast, structurally relaxed, and partially crystallized $Zr_{55}Cu_{35}Al_{10}$.

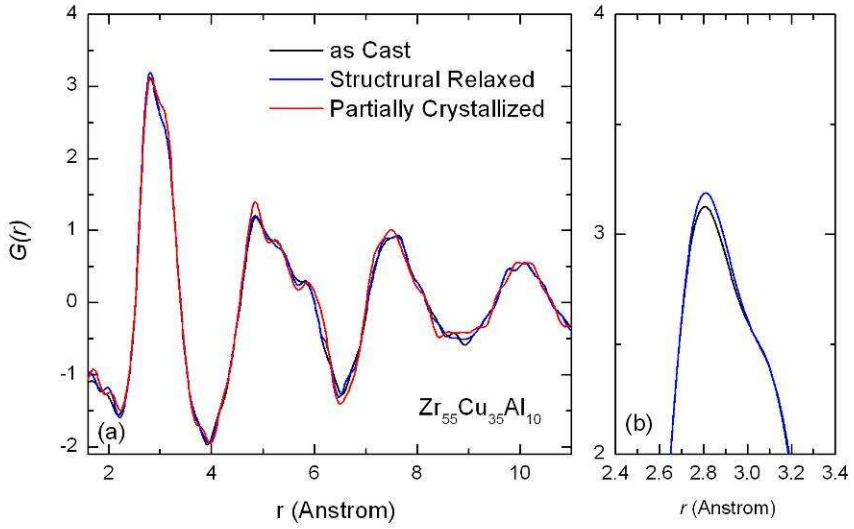

Figure 2-20. (a) The total radial distribution function, PDF, for as-cast, structurally relaxed, and partially crystallized $Zr_{55}Cu_{35}Al_{10}$ and (b) for as-cast and structurally relaxed in an enlarged scale.

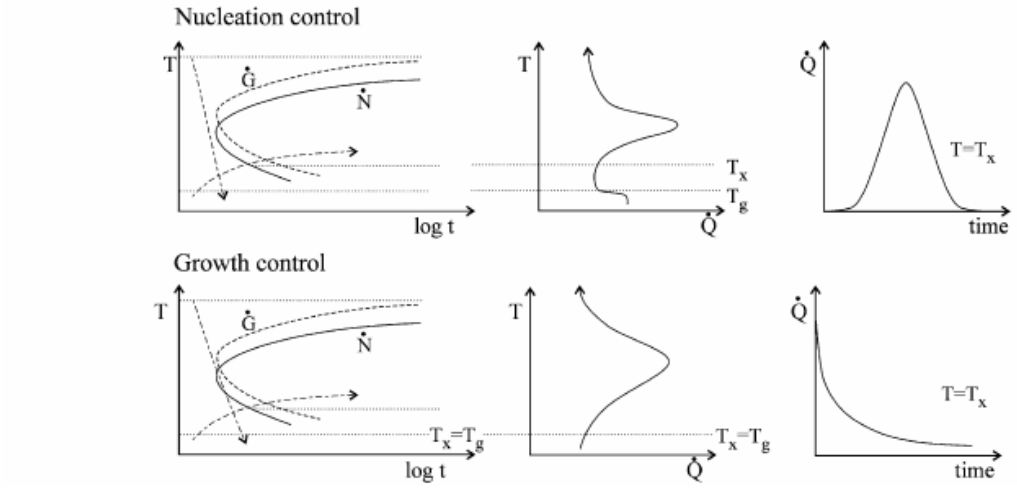

Figure 2-21 – Schematic showing the kinetics of metallic glass formation: nucleation control vs. growth control [102].

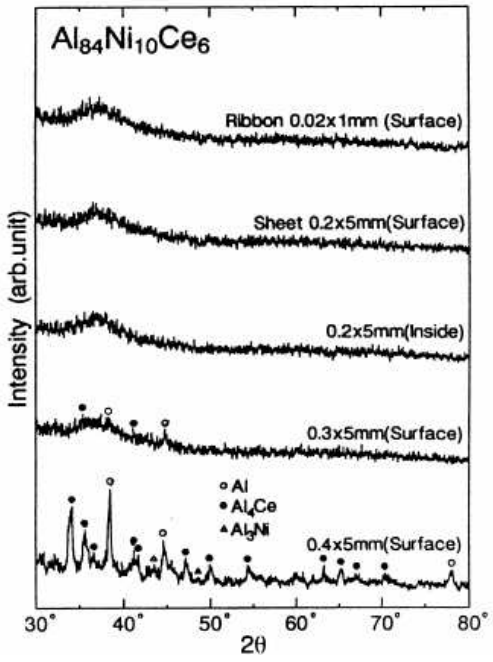

Figure 2-22. XRD patterns of $Al_{84}Ni_{10}Ce_6$ melt-spun ribbons with different thicknesses [5].

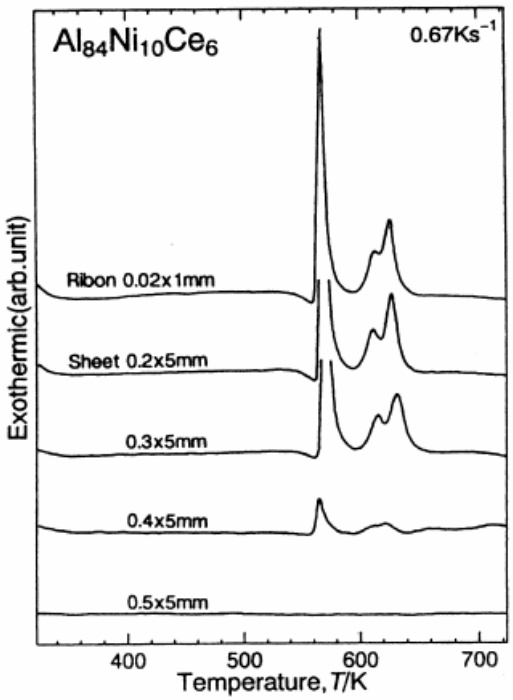

Figure 2-23. DSC curves of $Al_{84}Ni_{10}Ce_6$ melt-spun ribbons with different thicknesses [5].

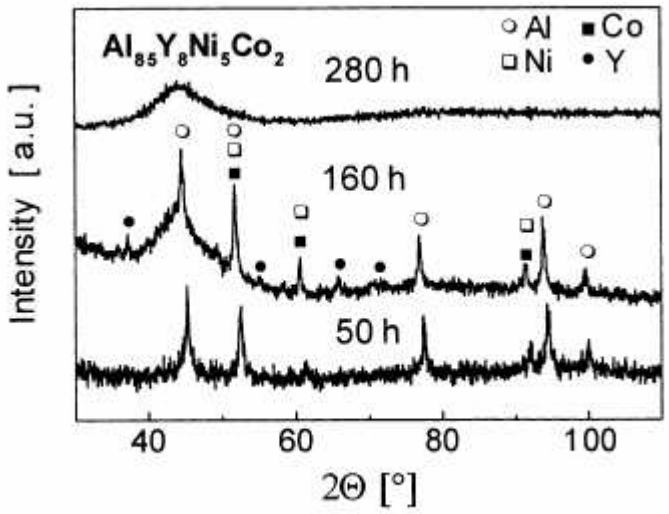

Figure 2-24. XRD patterns of $Al_{85}Y_8Ni_5Co_2$ after mechanical alloying for various times [103].

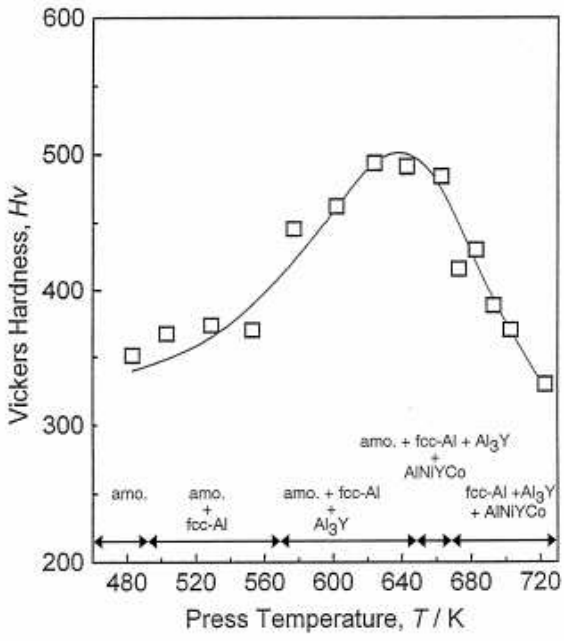

Figure 2-25. Pressing temperature of consolidation plotted against Vickers hardness for the consolidated $Al_{85}Y_8Ni_5Co_2$ alloys [4].

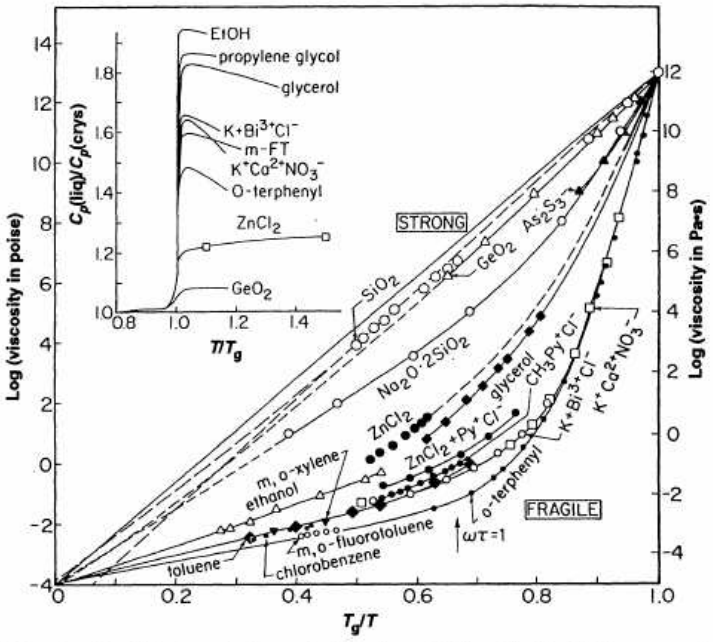

Figure 2-26. Arrhenius plot of viscosity vs. temperature scaled by T_g, showing the "strong-fragile" pattern of liquid behavior. The insert shows the large jump in C_p at T_g for fragile liquids and a small jump for strong liquids [109].

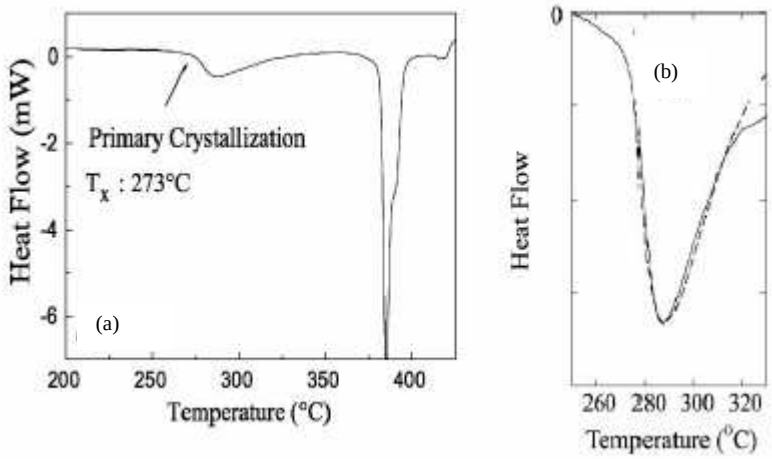

Figure 2-27. (a) DSC curve for $Al_{88}Y_7Fe_5$ melt-spun ribbon sample. The primary crystallization occurs at 273°C and corresponds to the formation of fcc nanocrystalline aluminum phase. (b) Close-up view of the primary crystallization [102].

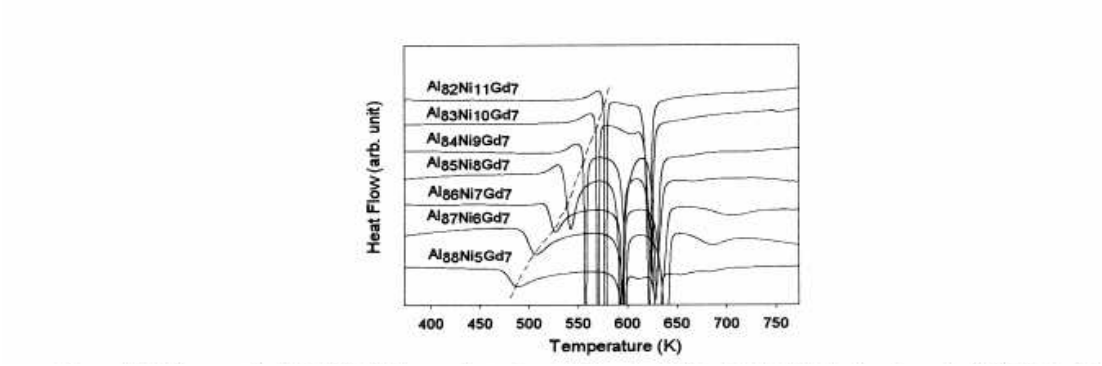

Figure 2-28. DSC curves of $Al_{93-x}Ni_xGd_7$ amorphous alloys. The dashed line corresponds to the primary crystallization [24].

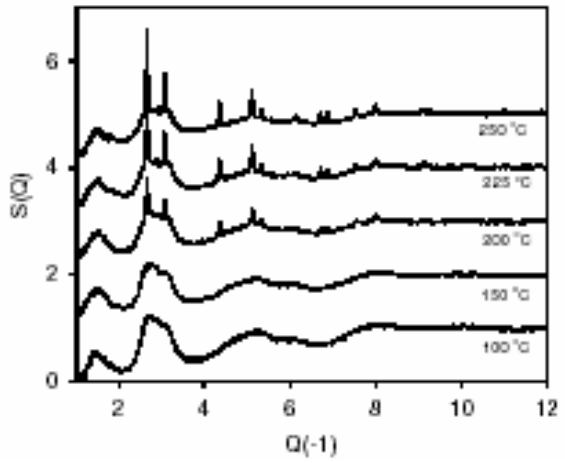

Figure 2-29. The structure function with increasing temperature. The diffraction peaks are indexed to Al [111].

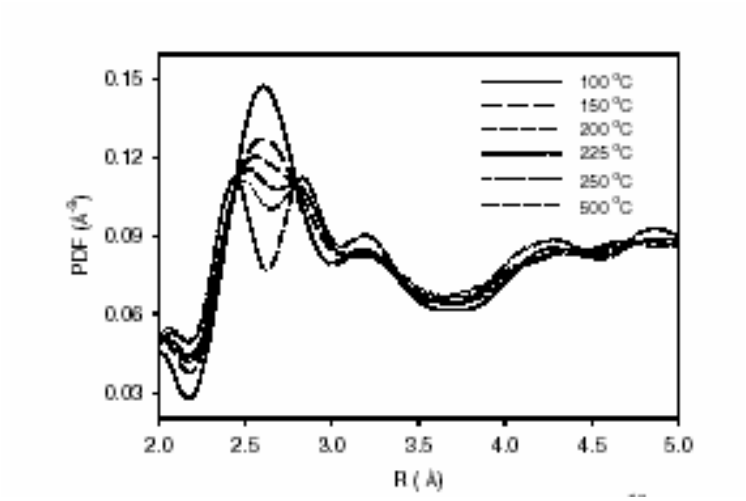

Figure 2-30. The local atomic structure for $Al_{87}Ni_7Nd_6$ at several temperatures. Above 500^{o}C, the atomic structure is dominated by the crystalline phases [111].

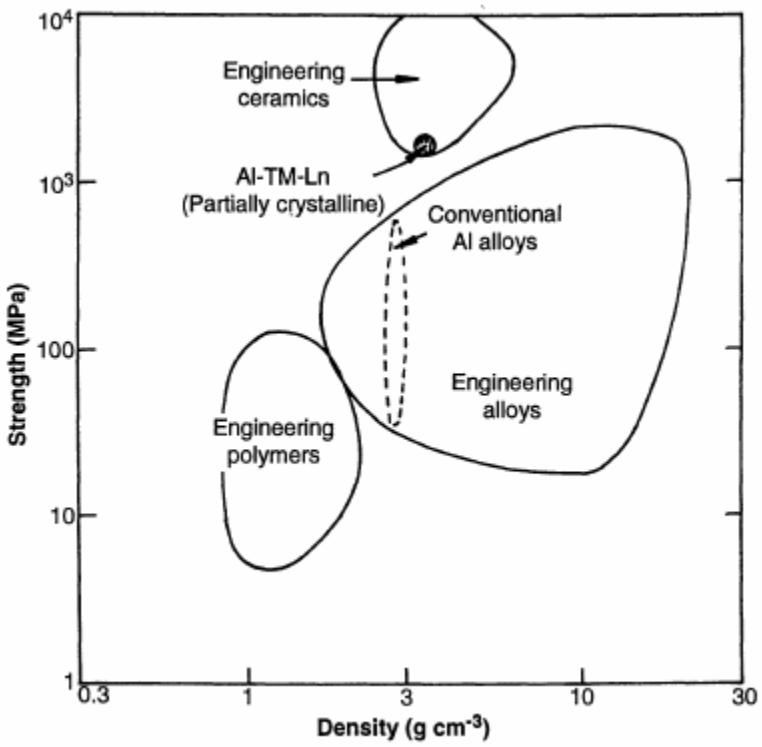

Figure 2-31. Strength vs. density plot for engineering materials. Partially crystalline Al-based alloys can have properties greater than conventional Al alloys [44].

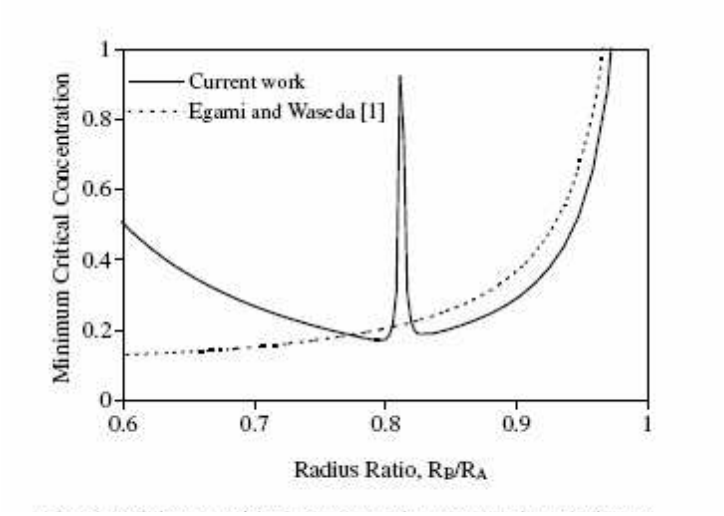

Figure 2-32. Minimum critical concentration vs. the relative atomic radius [119, 120].

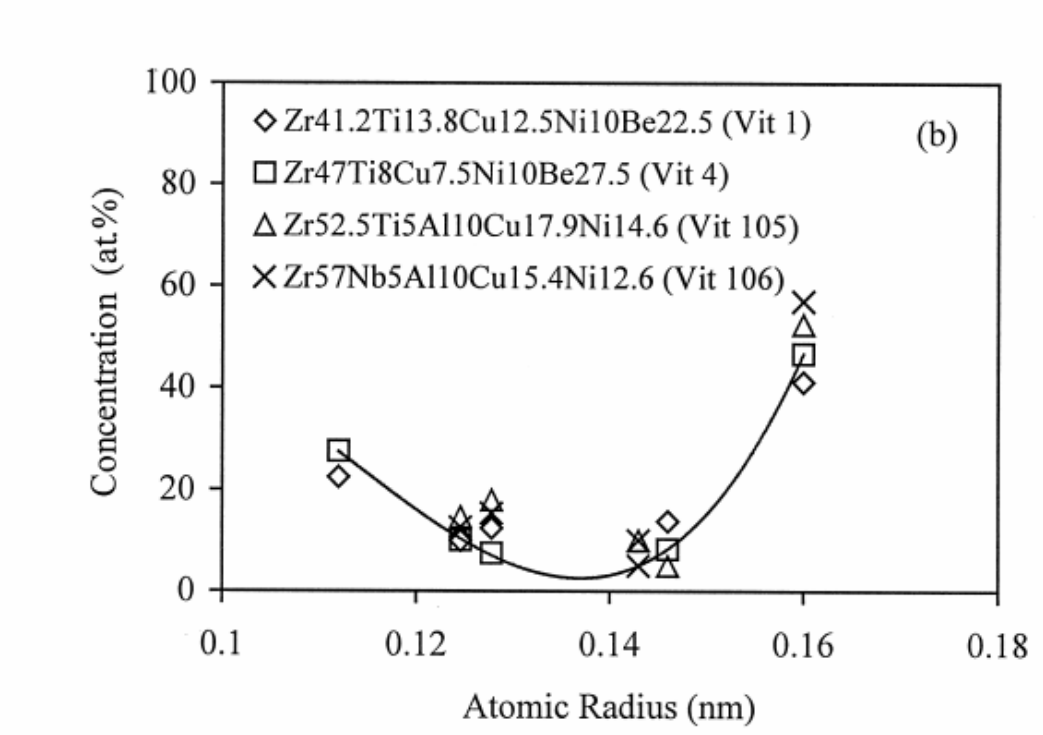

Figure 2-33. Plot of concentration vs. atomic radius for the bulk metallic glass forming Zr-based alloyes, showing a concave-up appearance [118].

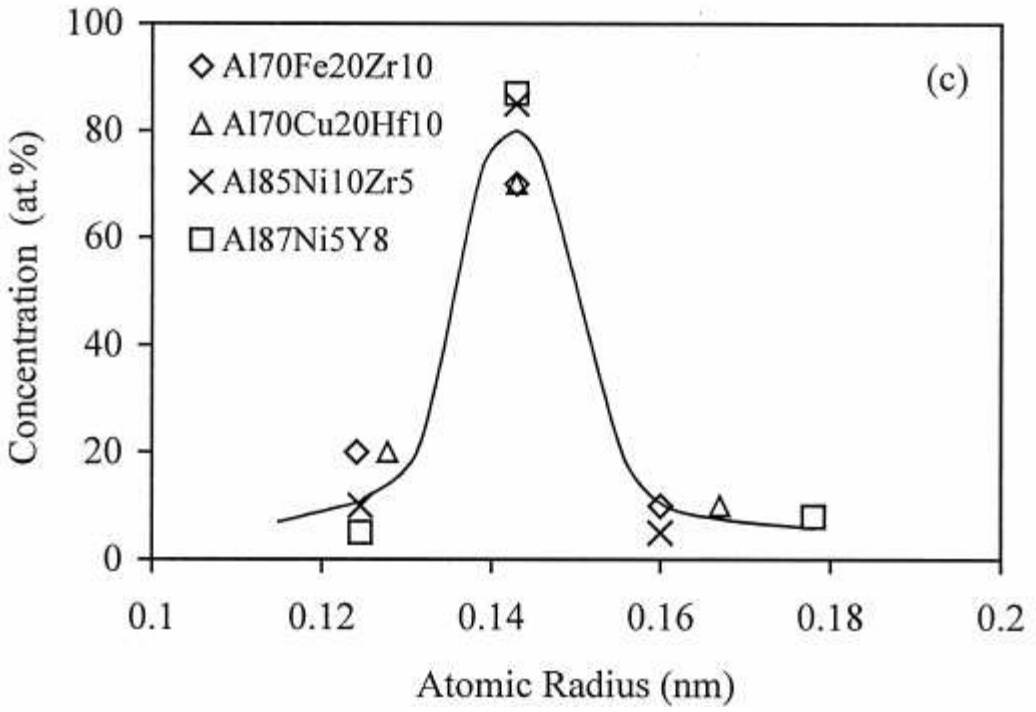

Figure 2-34. Plot of concentration vs. atomic radius for marginal glass-forming Al-based alloys, showing a concave-down appearance [118].

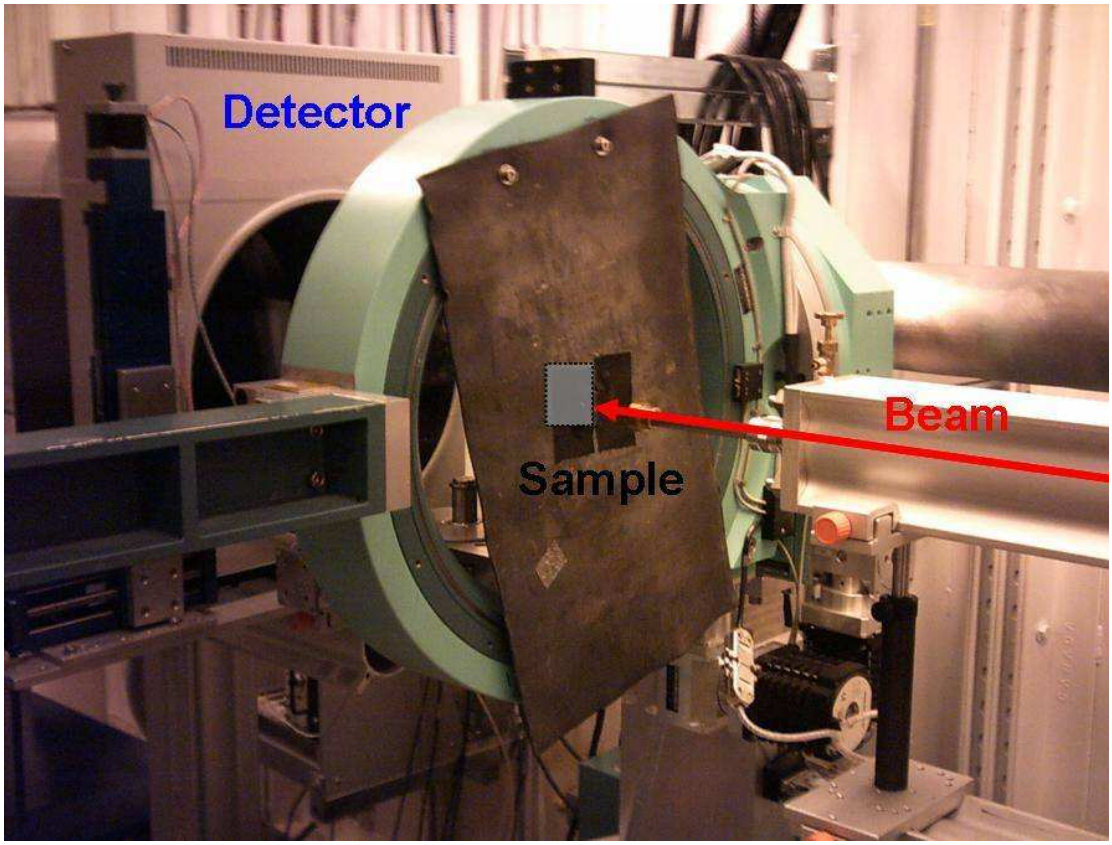

Figure 3-1. 6-ID-C synchrotron x-ray beamline at the Advanced Photon Source showing the direction of the x-ray beam, the sample location, and the detector.

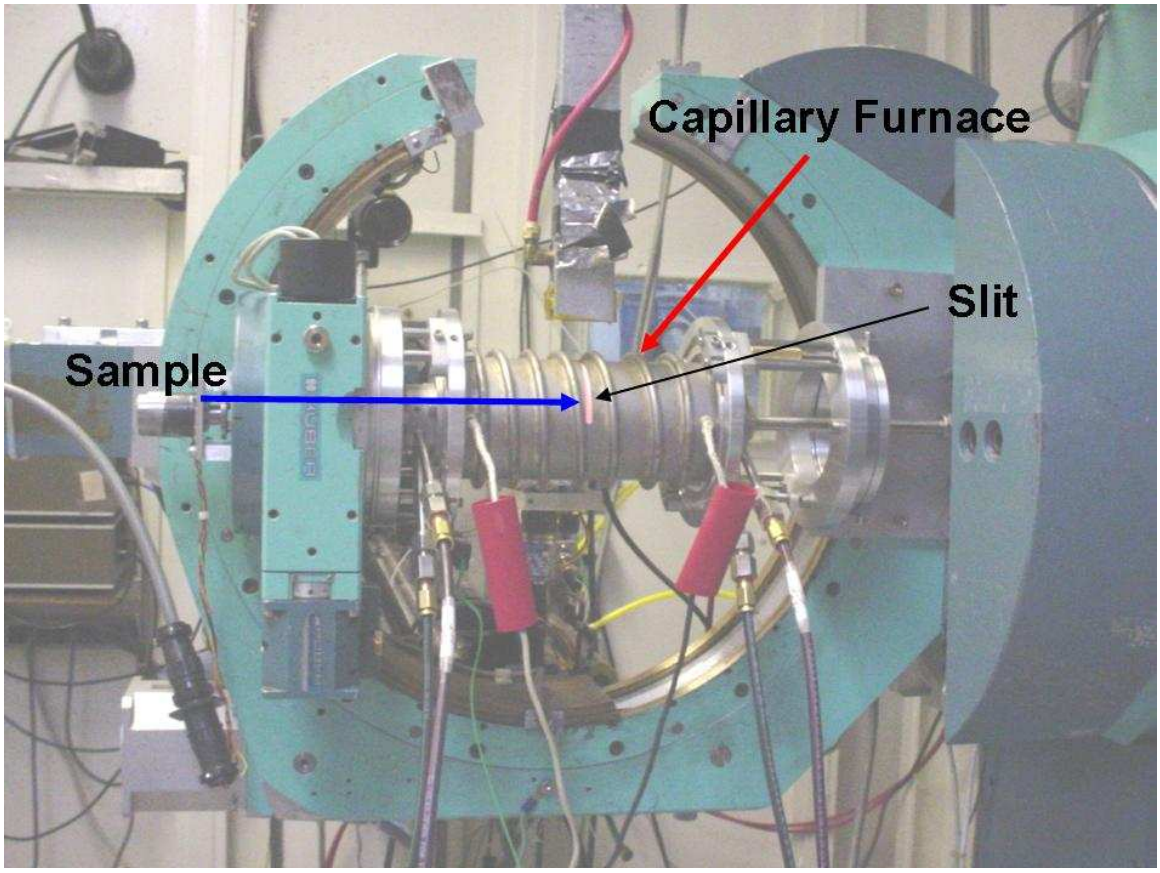

Figure 3-2. X14A synchrotron x-ray beamline at the National Synchrotron Light Source showing the sample location, the capillary furnace, and the slit for the diffracted beam.

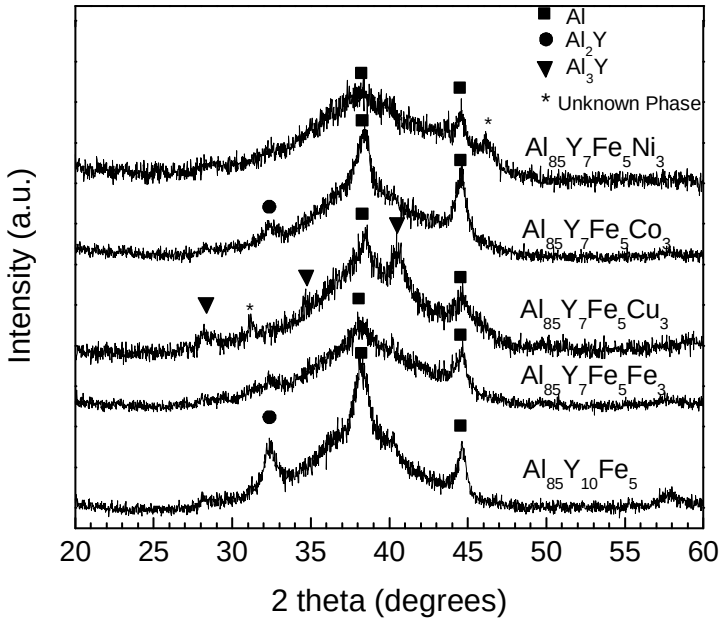

Figure 4-1. X-ray diffraction patterns of ball-milled $Al_{85}Y_{10}Fe_5$ and $Al_{85}Y_7Fe_5TM_3$ (TM = Ni, Co, Cu, and Fe).

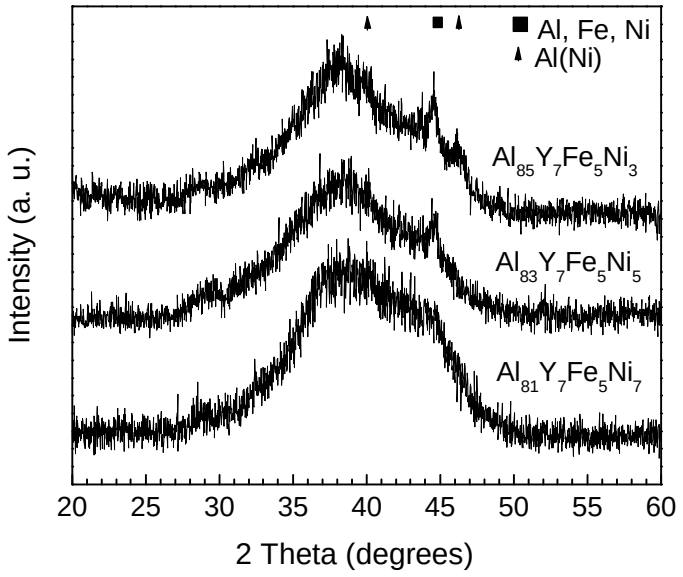

Figure 4-2. X-ray diffraction pattern of $Al_{85-x}Y_7Fe_5Ni_{3+x}$ showing the effect of changing the Al/Ni ratio.

.

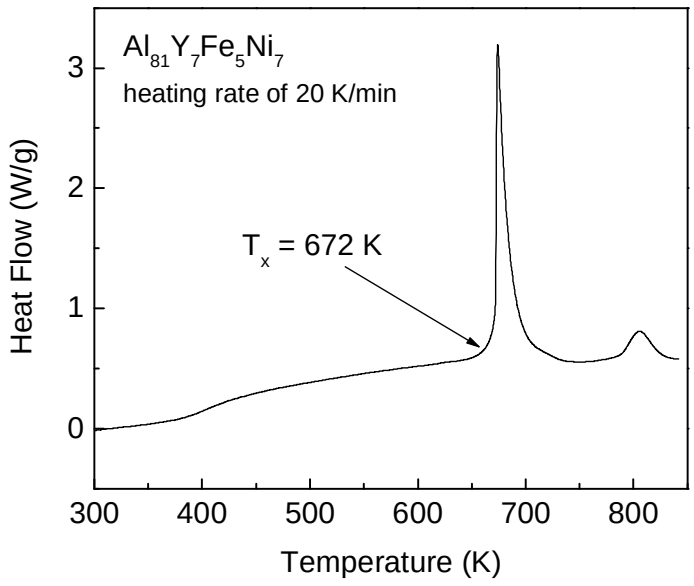

Figure 4-3. Differential scanning calorimetry results for $Al_{81}Y_7Fe_5Ni_7$ sample milled for 30 hours showing multiple exothermic events.

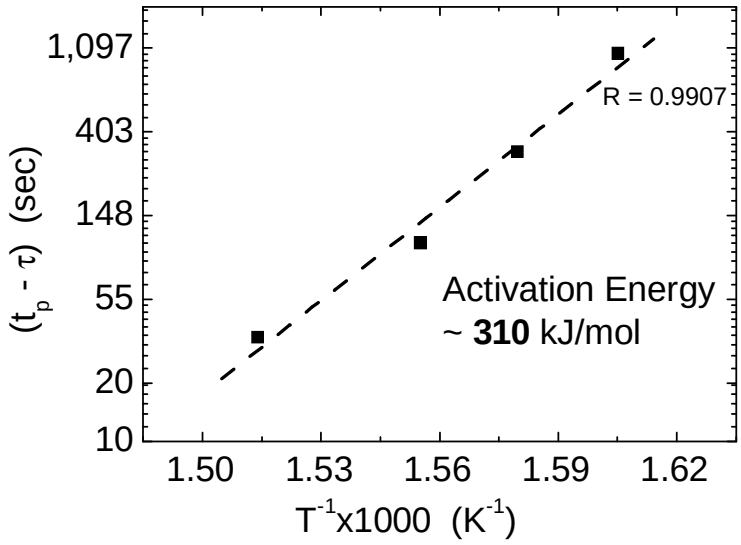

Figure 4-4. Plot of $(t_p-\tau)$ vs. 1/T as measured from isothermal annealing of $Al_{83}Y_7Fe_5Ni_5$.

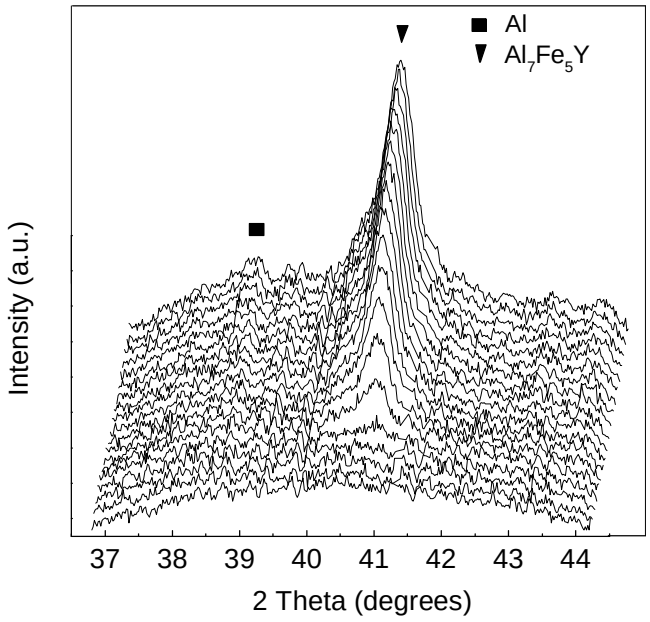

Figure 4-5. *In-situ* high-temperature x-ray diffraction patterns measured during isothermal annealing at 633 K on $Al_{83}Y_7Fe_5Ni_5$ for 95 minutes showing that the crystallization is a combination of crystallization of the amorphous phase and intermetallic phase formation.

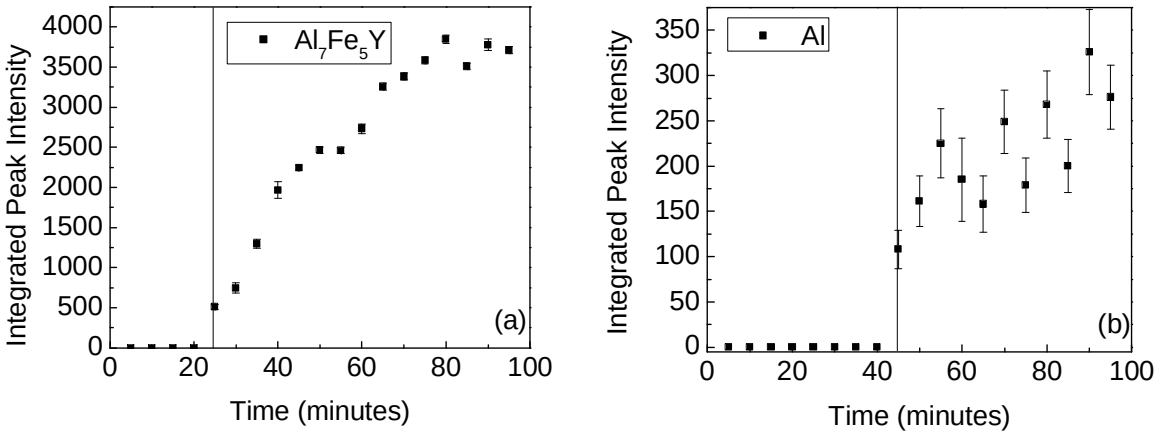

Figure 4-6. Integrated peak intensity of $Al_{83}Y_7Fe_5Ni_5$ during *in-situ* high-temperature x-ray diffraction at 633 K showing (a) intensity of the Al_7Fe_5Y phase with increasing time and (b) intensity of the fcc-Al phase with increasing time.

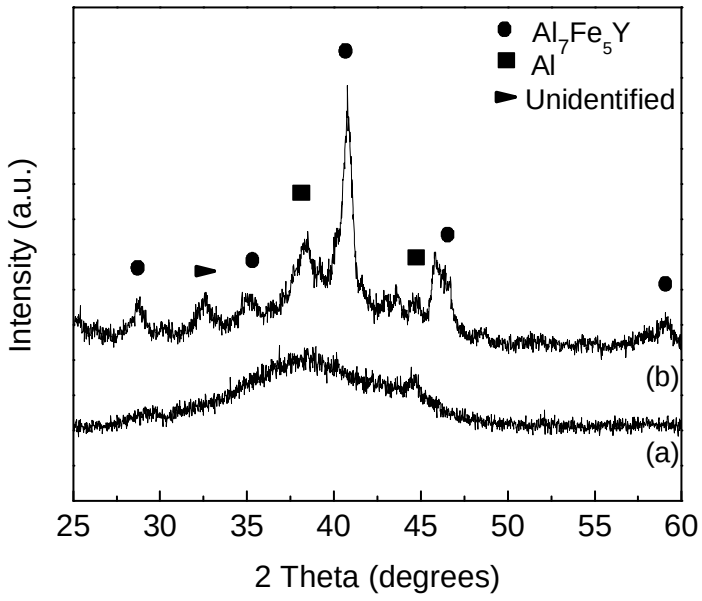

Figure 4-7. XRD patterns for the as-milled $Al_{83}Y_7Fe_5Ni_5$ sample (a) and the crystallized $Al_{83}Y_7Fe_5Ni_5$ (b) sample after annealing at 633 K for 95 minutes.

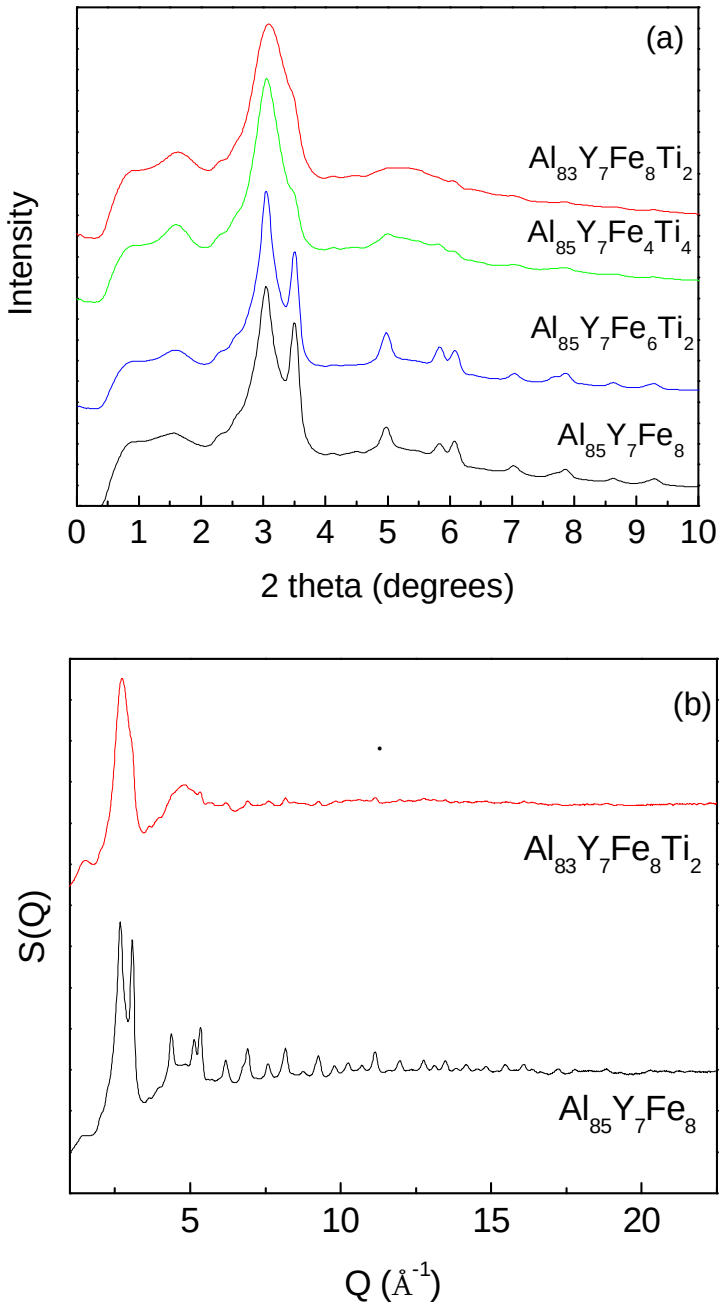

Figure 4-8. (a) X-ray diffraction patterns showing the effect of Ti additions to Al-Y-Fe alloy, (b) structure factors, *S(Q)*, of $Al_{85}Y_7Fe_8$ and $Al_{83}Y_7Fe_8Ti_2$ alloys after 45 hours of mechanical alloying. (c) comparison in the Q-range of 0 – 4 $Å^{-1}$.

Continued from Figure 4-8

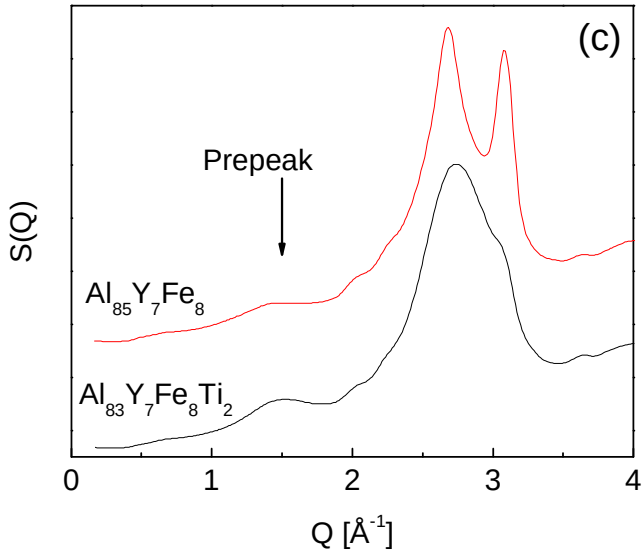

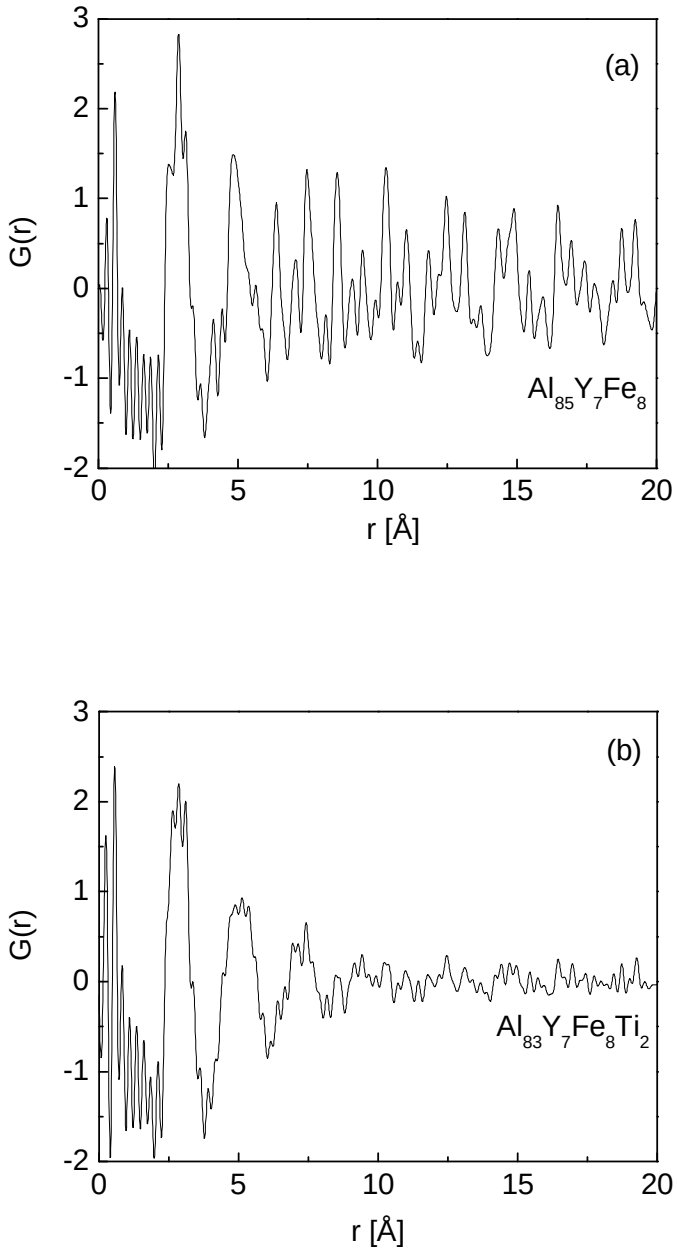

Figure 4-9. Pair distribution functions (PDF) of (a) $Al_{85}Y_7Fe_8$ and (b) $Al_{83}Y_7Fe_8Ti_2$ alloys.

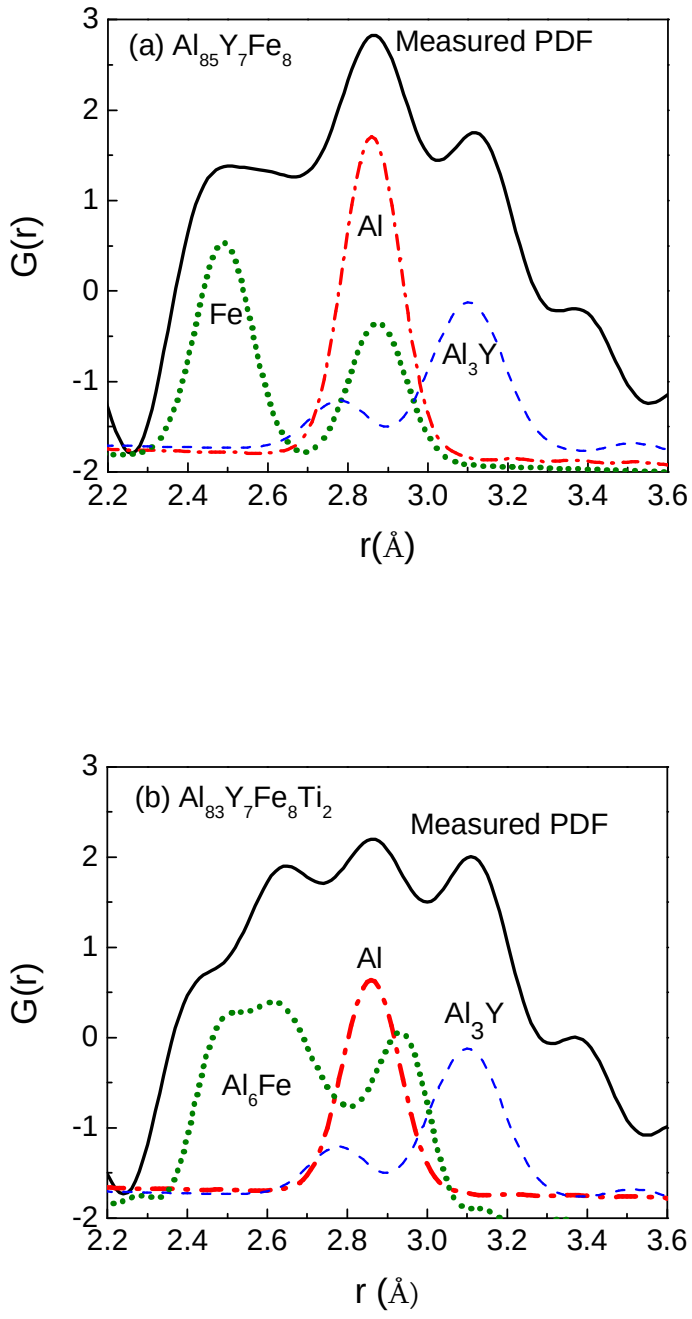

Figure 4-10. First coordination shell of PDF for (a) $Al_{85}Y_7Fe_8$ and (b) $Al_{83}Y_7Fe_8Ti_2$ alloys showing crystalline cluster approximations representative of the short range order.

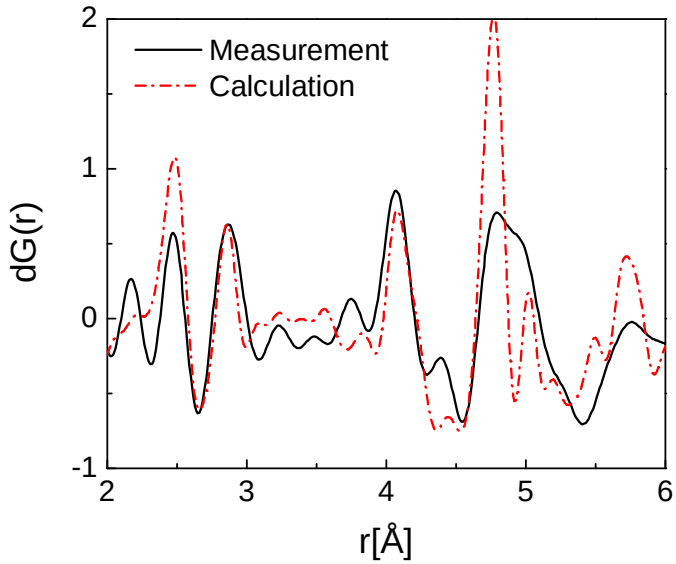

Figure 4-11. The difference pair distribution function (DPDF) of $Al_{83}Y_7Fe_8Ti_2$ subtracted from $Al_{85}Y_7Fe_8$. Also shown is the calculated DPDF of the theoretical PDF of Fe minus that of Al_6Fe for a comparison.

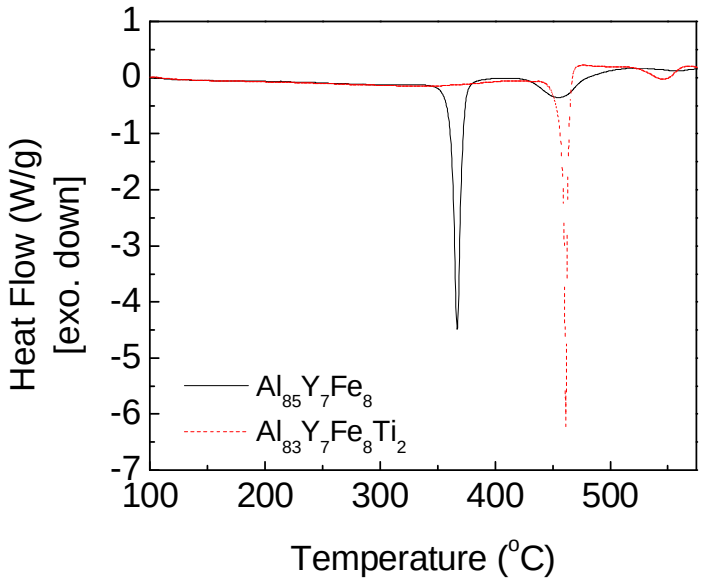

Figure 4-12. Differential scanning calorimetry (DSC) traces of $Al_{85}Y_7Fe_8$ and $Al_{83}Y_7Fe_8Ti_2$ performed at 20°C / minute.

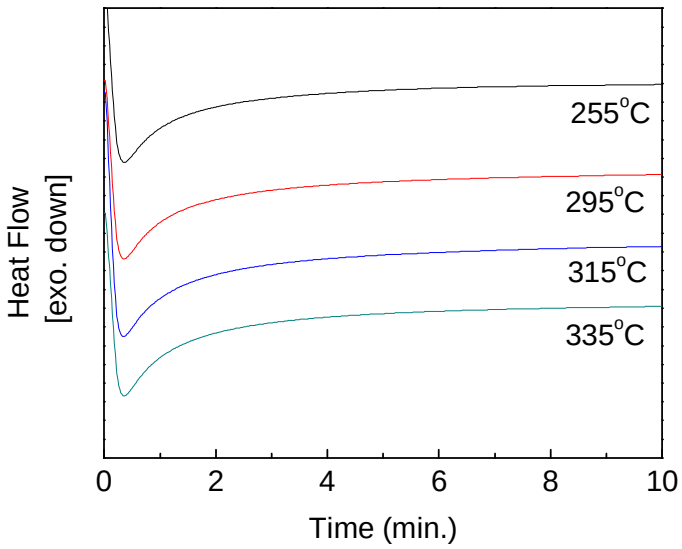

Figure 4-13. Isothermal DSC traces of $Al_{85}Y_7Fe_8$ performed at different temperatures.

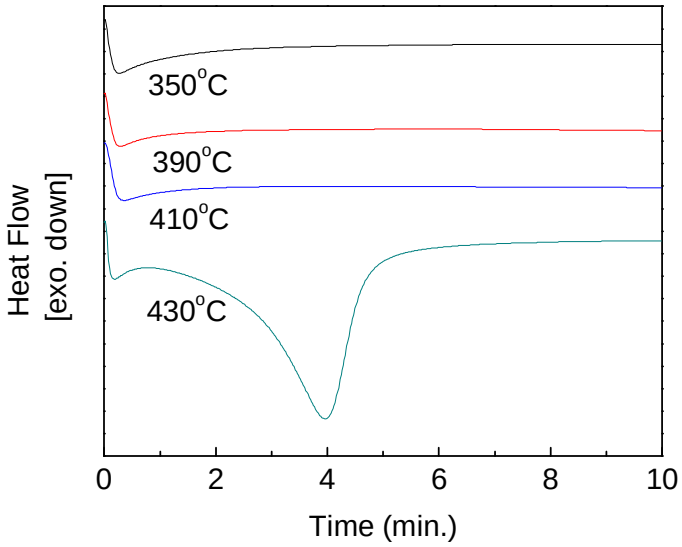

Figure 4-14. Isothermal DSC traces of $Al_{83}Y_7Fe_8Ti_2$ performed at different temperatures.

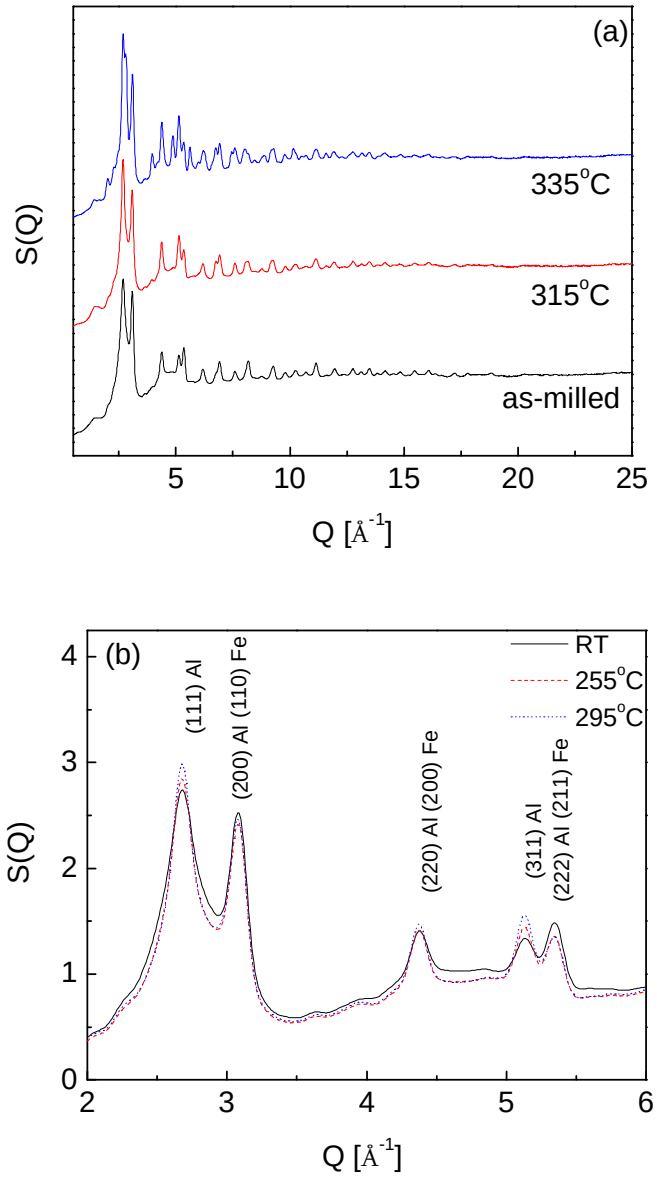

Figure 4-15. (a) Structure factor data of $Al_{85}Y_7Fe_8$ as-milled and annealed at 315°C and 335°C and (b) in the region of 2 – 6 $Å^{-1}$ in the as-milled condition and annealed at 255°C and 295°C.

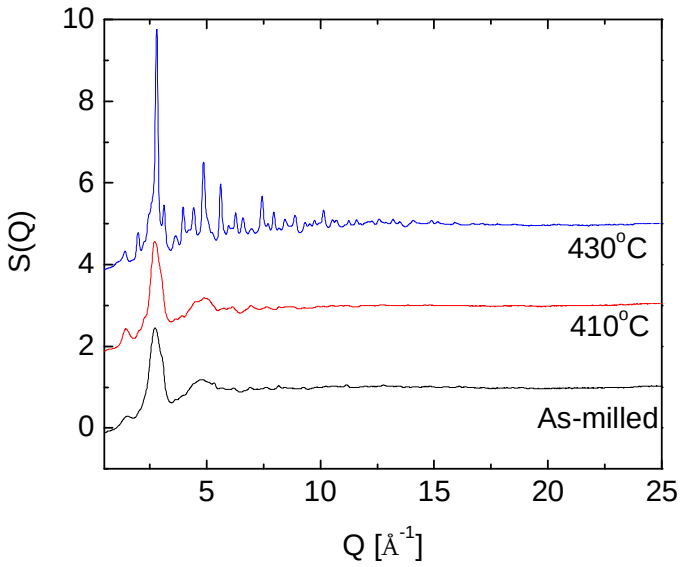

Figure 4-16. Structure factor data of $Al_{83}Y_7Fe_8Ti_2$ as-milled and annealed at 410°C and 430°C.

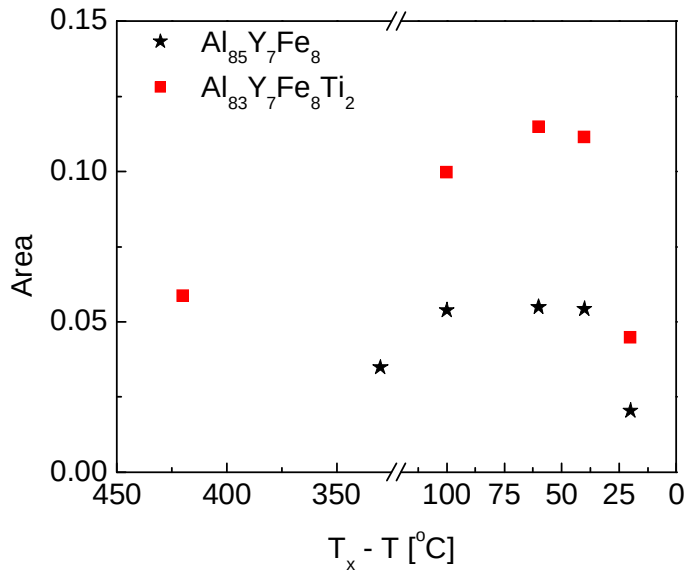

Figure 4-17. Area of prepeak of $Al_{85}Y_7Fe_8$ and $Al_{83}Y_7Fe_8Ti_2$ structure factors, plotted as a function of annealing temperature below crystallization temperature, T_x.

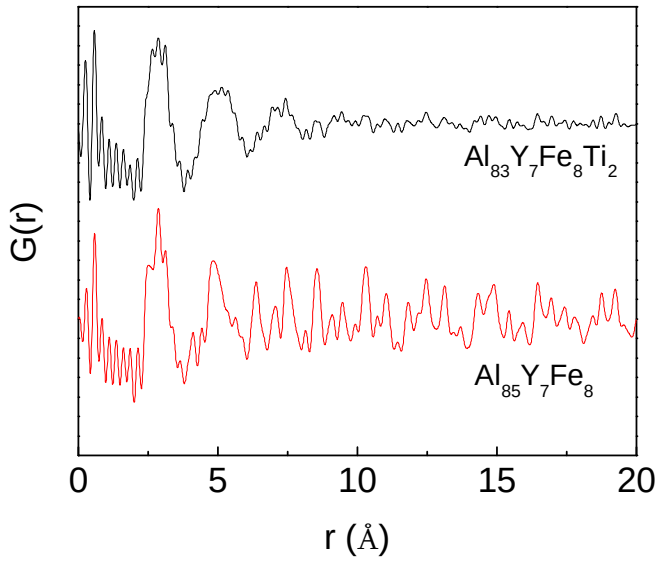

.

Figure 4-18. Pair distribution functions, G(r), of $Al_{85}Y_7Fe_8$ and $Al_{83}Y_7Fe_8Ti_2$ as-milled alloys.

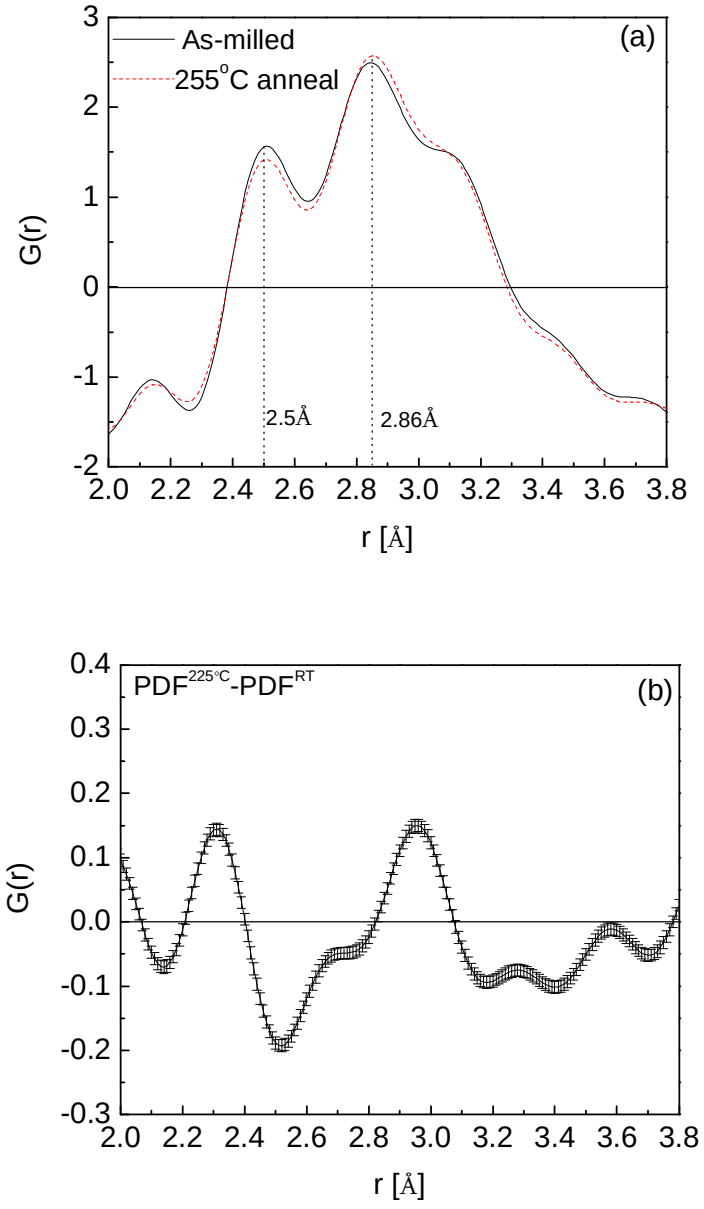

Figure 4-19. (a) PDF of $Al_{85}Y_7Fe_8$ in the as-milled condition and annealed at 255°C, (b) DPDF of as-milled alloy and annealed at 255°C, (c) DPDF annealed at 295°C and annealed at 255°C, and (d) DPDF of annealed at 335°C and annealed at 315°C.

Continued from Figure 4-19.

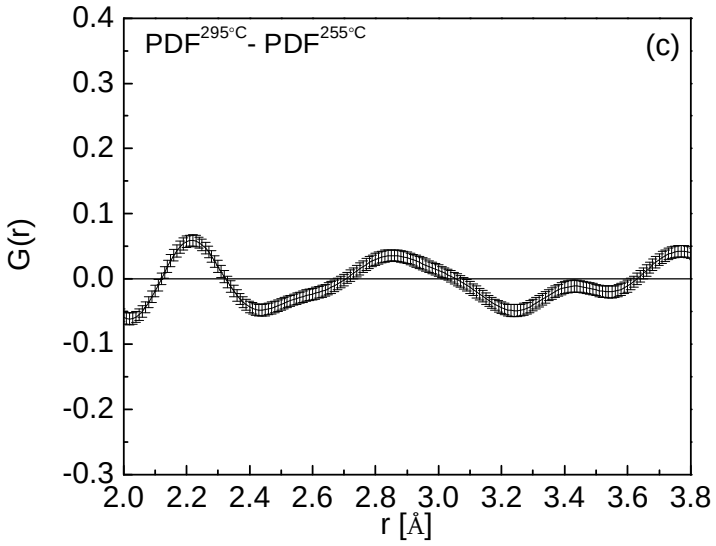

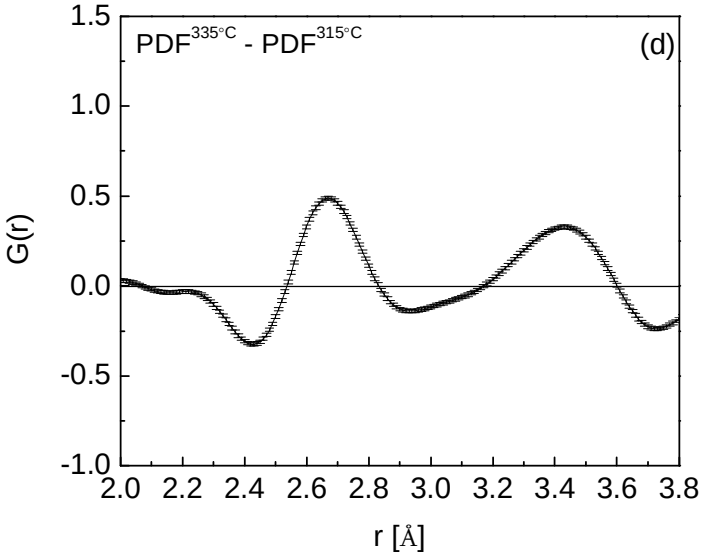

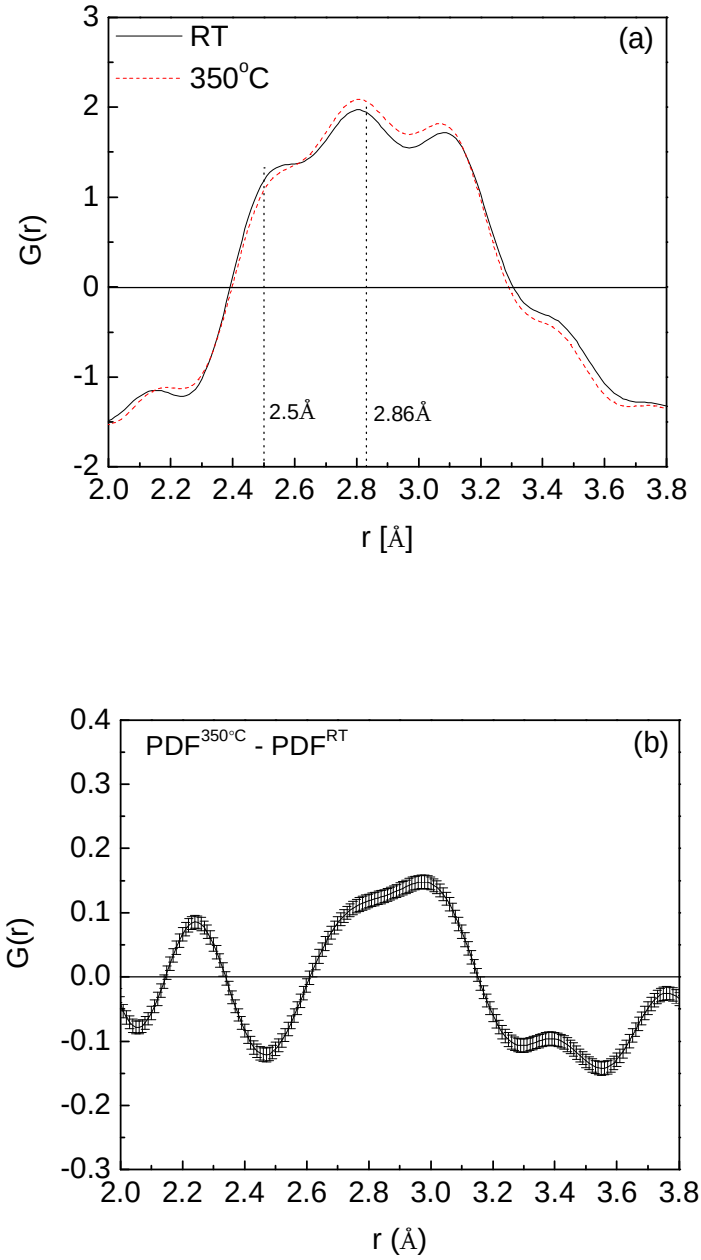

Figure 4-20. (a) PDF of $Al_{83}Y_7Fe_8Ti_2$ as-milled alloy and annealed at 350°C, (b) DPDF of as-milled alloy and annealed at 350°C, (c) DPDF of annealed at 410°C and annealed at 390°C, and (d) DPDF of annealed at 430°C and annealed at 410°C.

Continued from Figure 4-20.

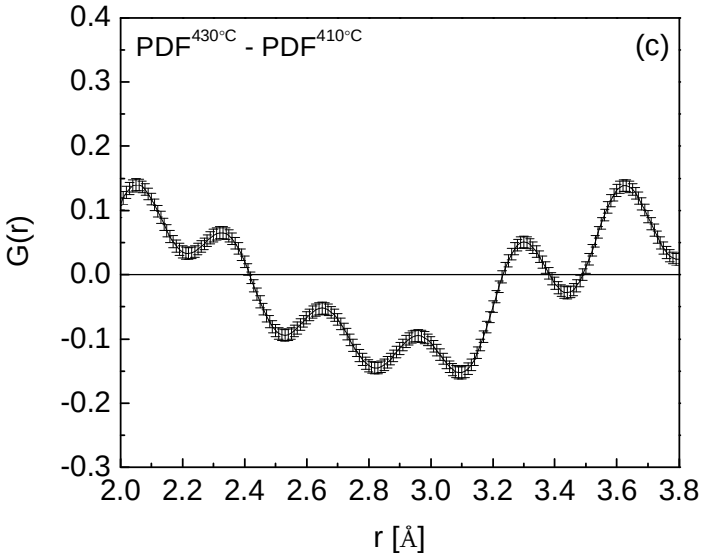

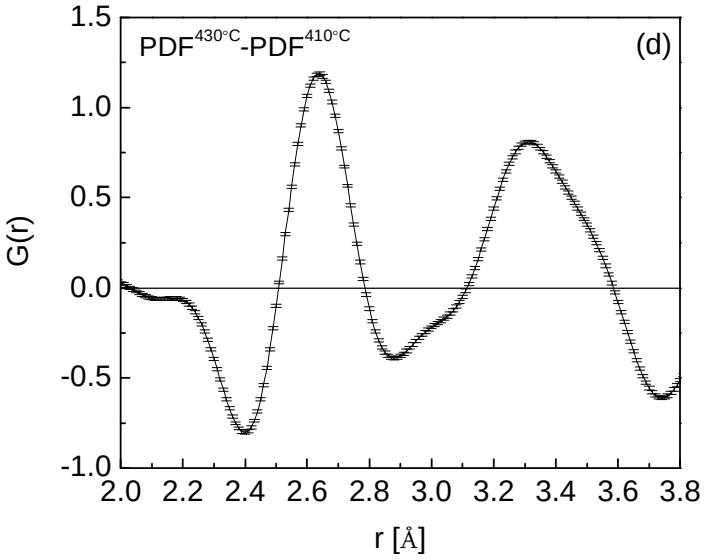

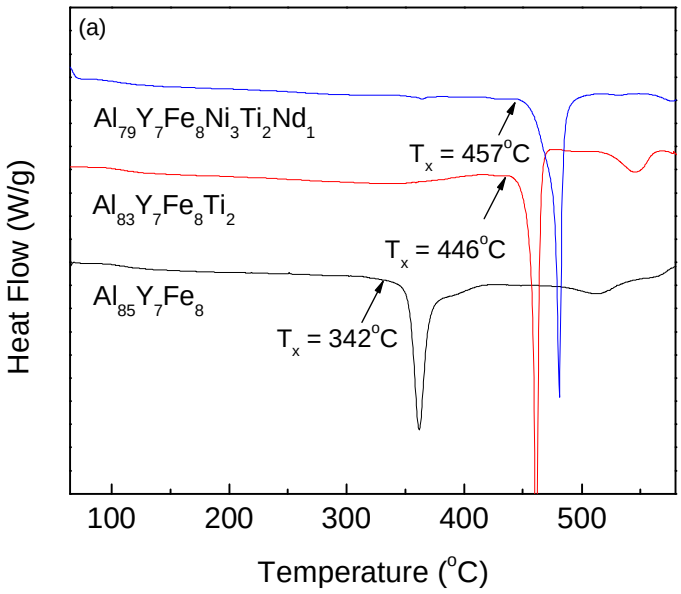

Figure 4-21. DSC traces of $Al_{85}Y_7Fe_8$, $Al_{83}Y_7Fe_8Ti_2$, and $Al_{79}Y_7Fe_8Ni_3Ti_2Nd_1$ performed at 20°C/minute.

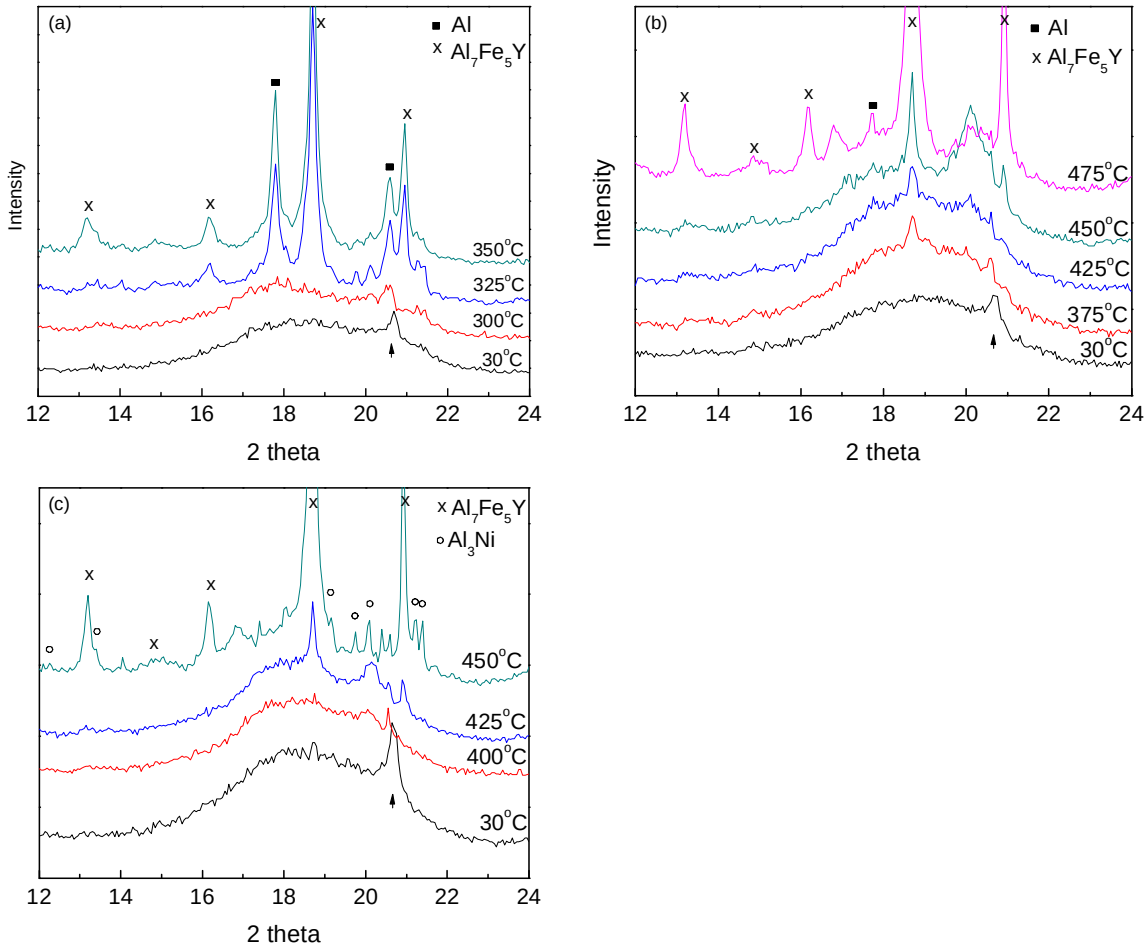

Figure 4-22. Selected *in-situ* synchrotron XRD patterns for (a) $Al_{85}Y_7Fe_8$ at 30°C, 300°C, 325°C, and 350°C; (b) $Al_{83}Y_7Fe_8Ti_2$ at 30°C, 375°C, 425°C, 450°C, and 475°C; and (c) $Al_{79}Y_7Fe_8Ni_3Ti_2Nd_1$ at 30°C, 400°C, 425°C, and 450°C . An Fe phase (marked with an arrow) is present in all of the as-milled alloys.

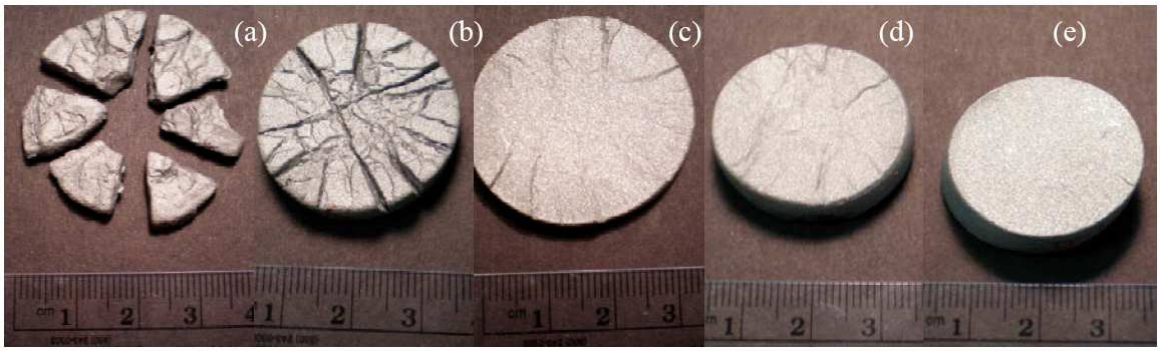

Figure 4-23. Photographs of consolidated $Al_{79}Y_7Fe_8Ni_3Ti_2Nd1$ samples after forging: (a) 100% MA alloy forged at 420°C, (b) 85% MA + 15% CG alloy forged at 420°C, (c) 70% MA + 30% CG alloy forged at 420°C, (d) 100% MA alloy forged at 445°C, and (e) 70% MA + 30% CG alloy forged at 445°C. (scale in centimeters)

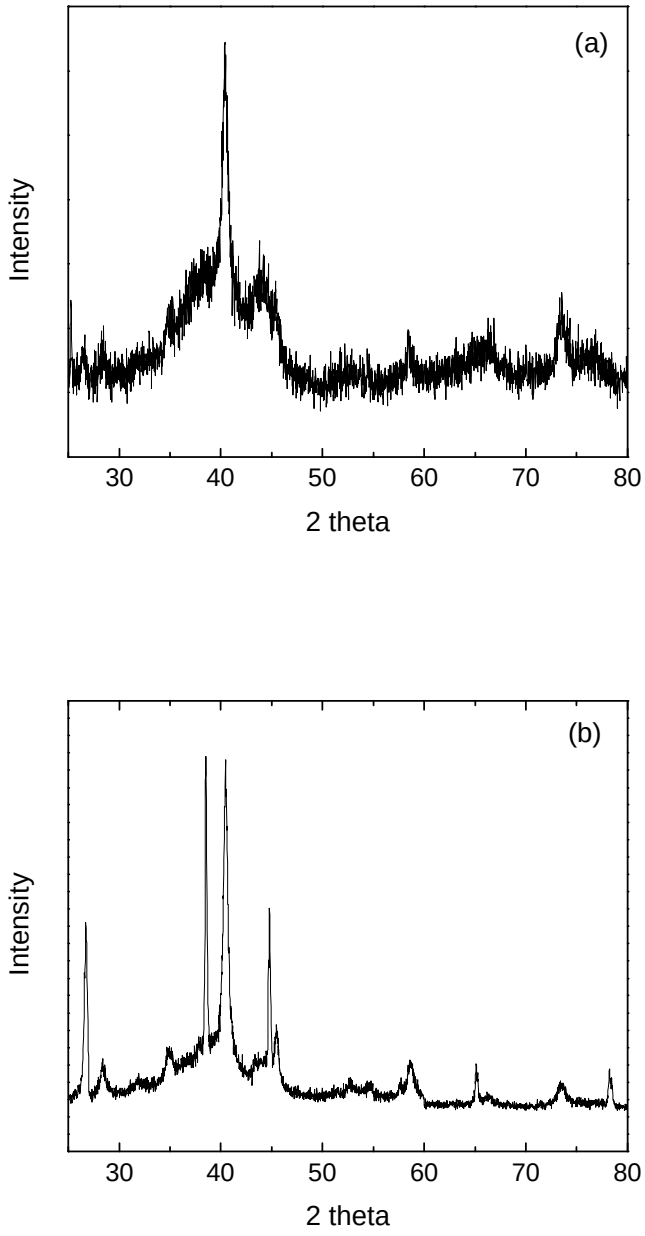

Figure 4-24. X-ray diffraction patterns of (a) 100% MA alloy forged at 420°C, (b) 85% MA + 15% CG alloy forged at 420°C, (c) 70% MA + 30% CG alloy forged at 420°C, (d) 100% MA alloy forged at 445°C, and (e) 70% MA + 30% CG alloy forged at 445°C.

Continued from Figure 4-24.

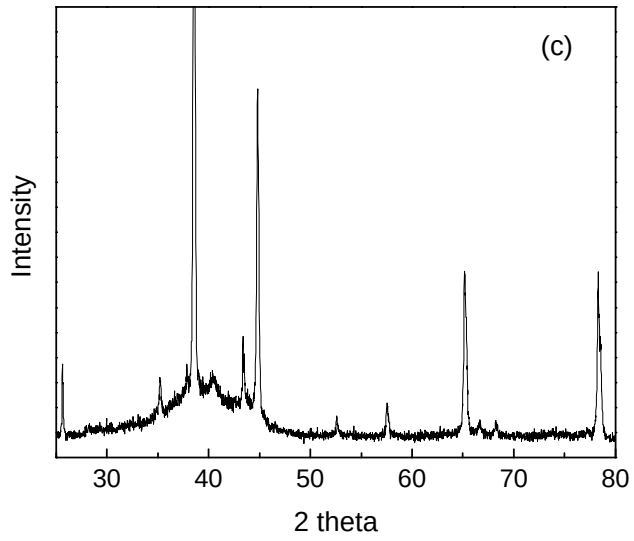

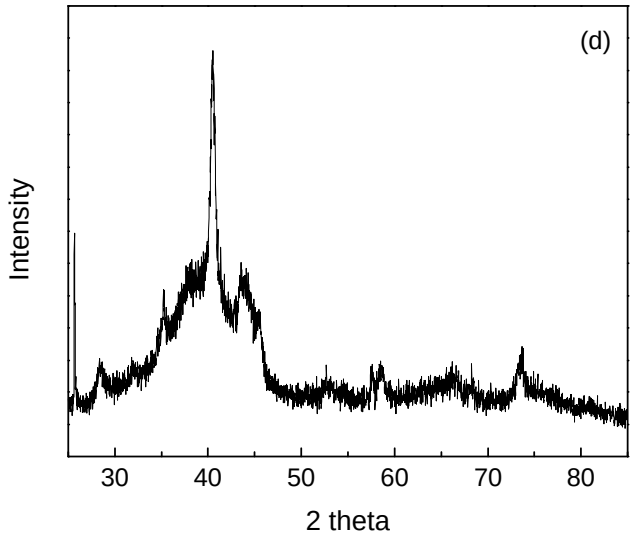

Continued from Figure 4-24.

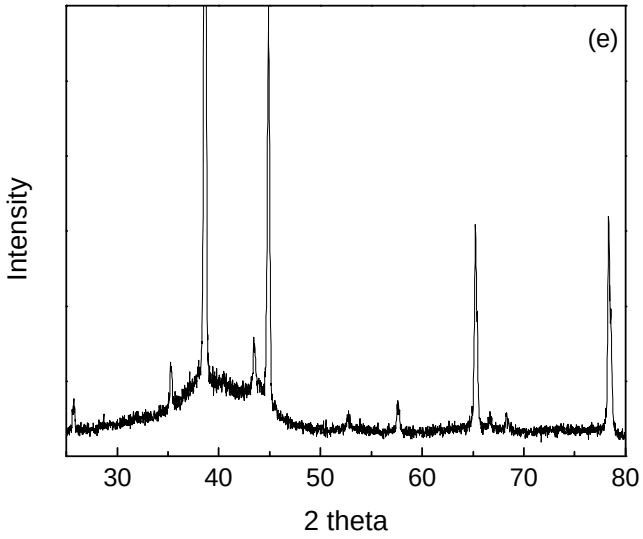

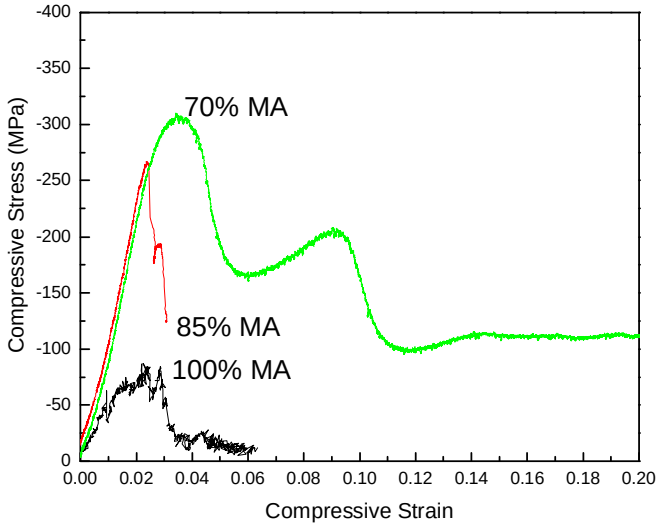

Figure 4-25. Compression test results of samples forged at 420°C.

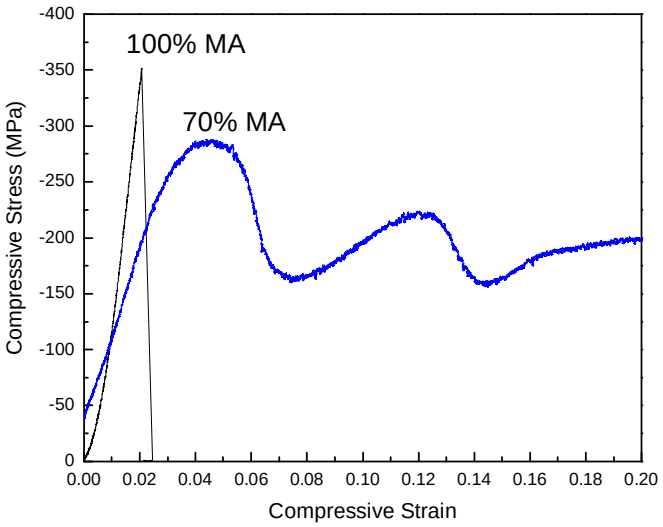

Figure 4-26. Compression test results of samples forged at 445°C.

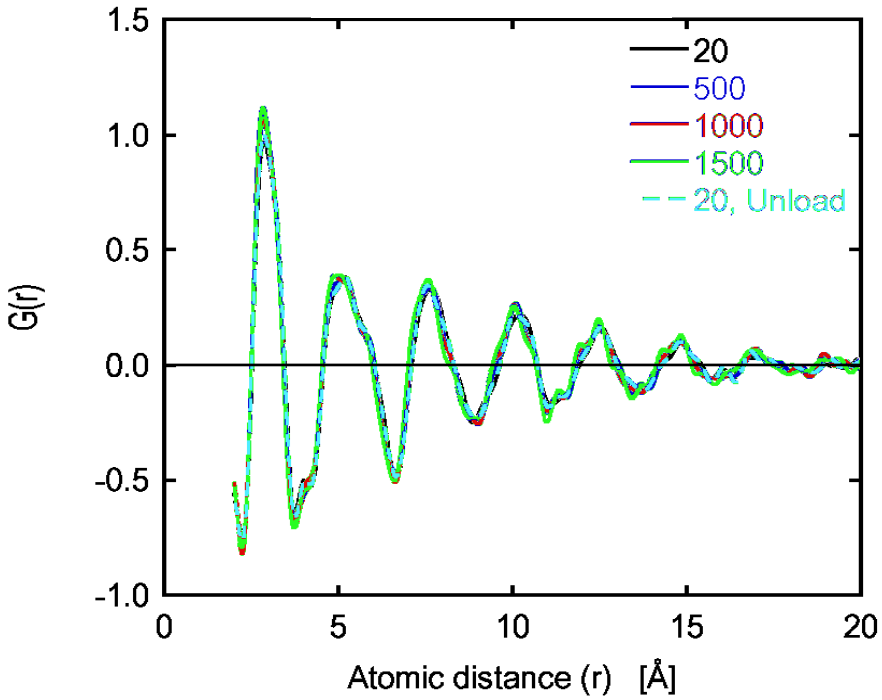

Figure 4-27a. Pair distribution function G(r) calculated from the S(q) diffraction data measured on $Zr_{57}Nb_5Cu_{15.4}Ni_{12.6}Al_{10}$ using SMARTS instrument.

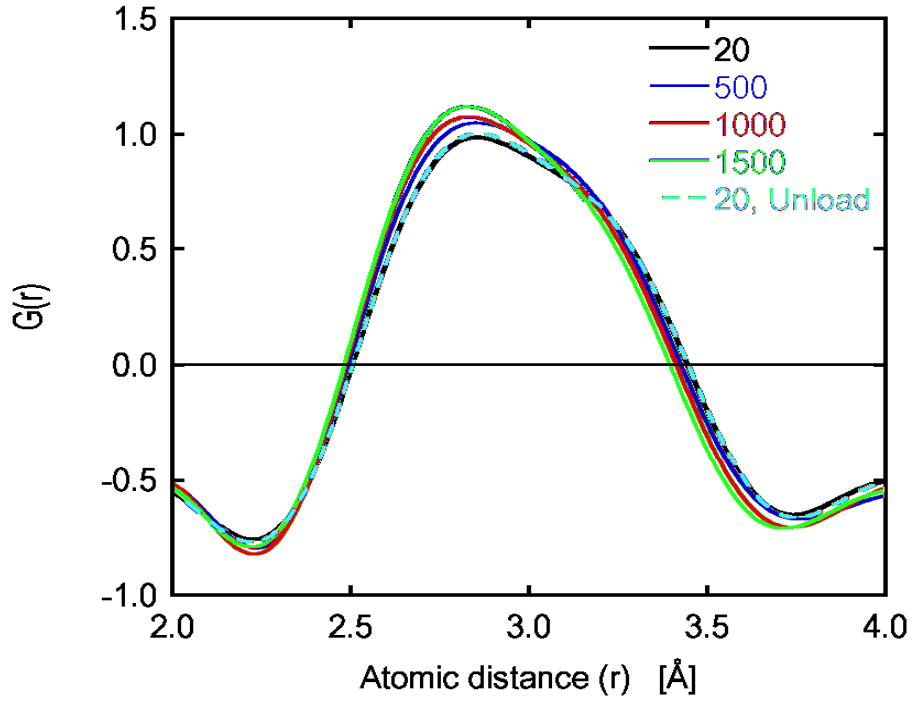

Figure 4-27b. First correlation shell of the pair distribution function measured $Zr_{57}Nb_5Cu_{15.4}Ni_{12.6}Al_{10}$ using SMARTS instrument, showing shift of PDF toward compressive strains as load is applied.

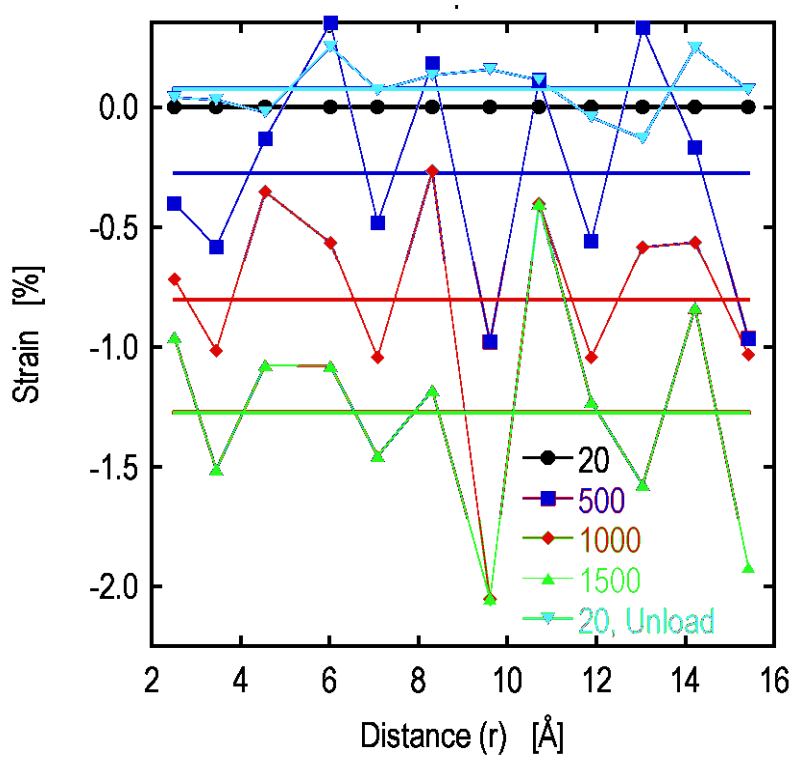

Figure 4-28a. Intercept strain data calculated from G(r) as a function distance, r for $Zr_{57}Nb_5Cu_{15.4}Ni_{12.6}Al_{10}$.

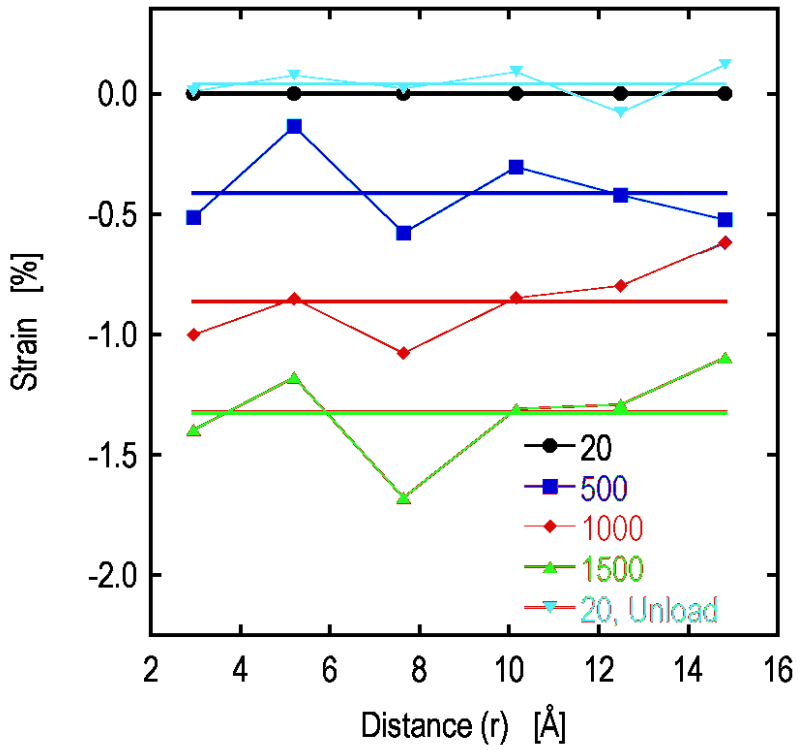

Figure 4-28b. Center-of-mass strain as a function of distance determined from PDF analysis for $Zr_{57}Nb_5Cu_{15.4}Ni_{12.6}Al_{10}$.

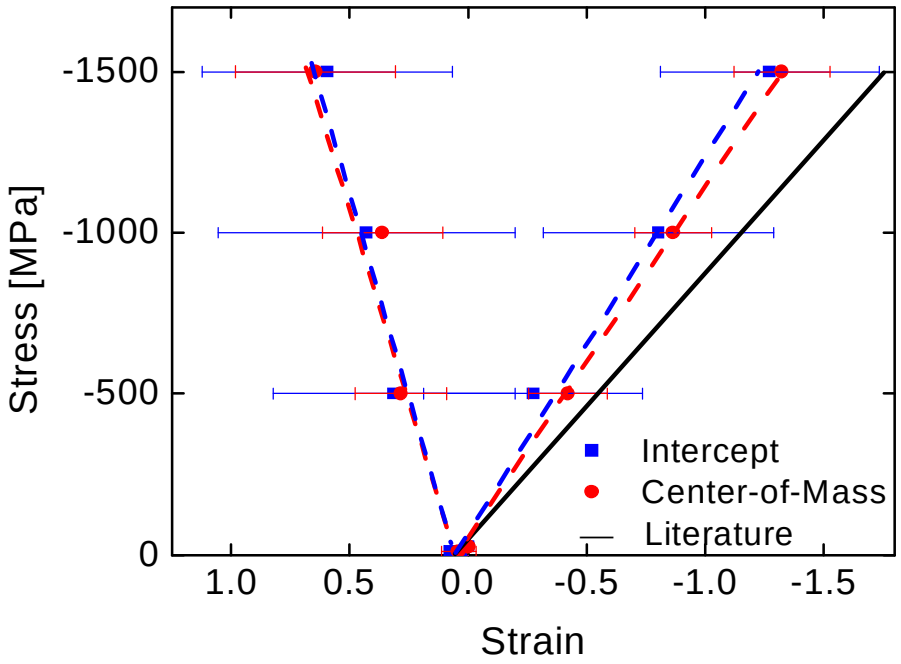

Figure 4-29. Stress vs. strain curve for $Zr_{57}Nb_5Cu_{15.4}Ni_{12.6}Al_{10}$ calculated on SMARTS from average local strains in G (r) by the intercept method and the center of mass method.

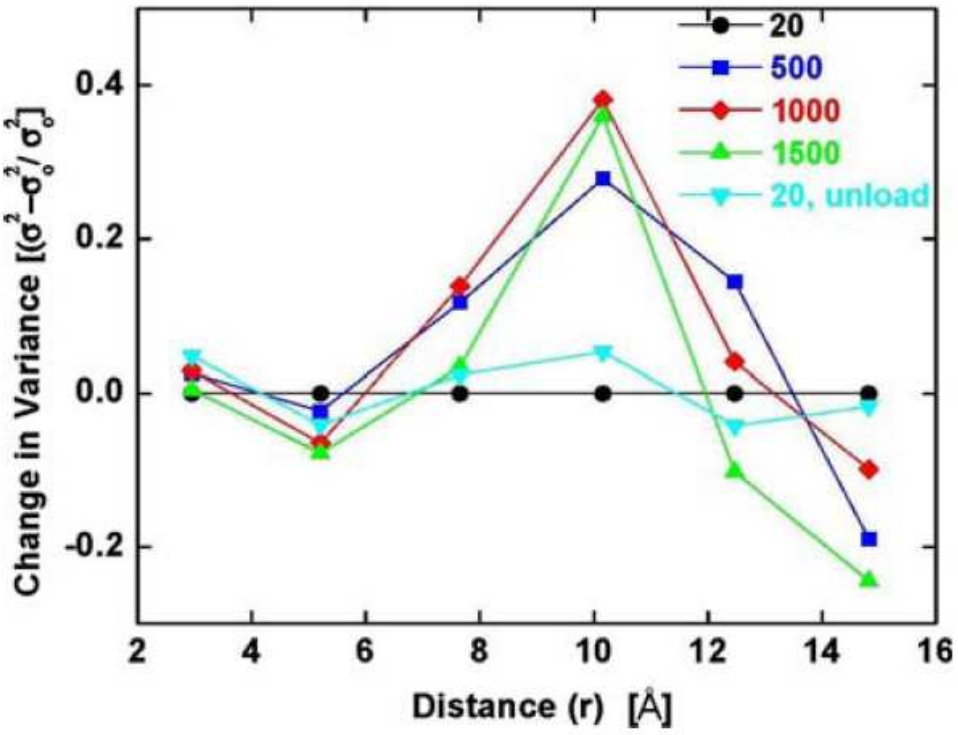

Figure 4-30. Change in variance from the center of mass measurements as a function of distance *r* measured on $Zr_{57}Nb_5Cu_{15.4}Ni_{12.6}Al_{10}$ bulk metallic glass.

Vita

Timothy Wayne Wilson Jr. was born in Memphis, Tennessee on November 14, 1980. He grew up in Oak Ridge, Tennessee. He attended the University of Tennessee, Knoxville and graduated in 2003 with a Bachelors of Science in Materials Science and Engineering. He continued at the University of Tennessee, and in 2005 received his Masters of Science. He has completed internships working for Michelin in Opelika, Alabama and Los Alamos National Laboratory in Los Alamos, New Mexico. While working as a research assistant at the University of Tennessee he pursued a Doctorate of Philosophy in the major of Materials Science and Engineering. He has performed research on the processing, structure, and properties of amorphous metallic alloys with a concentration on aluminum-based alloys.

Mr. Wilson is currently working as a metallurgist at CITGO Petroleum Corporation in Lake Charles, Louisiana working in the Fixed Equipment Reliability Engineering Group.